

## ABSTRACT

Title of Document: MULTIVARIATE STATISTICAL  
TECHNIQUES FOR ACCURATELY  
AND NONINVASIVELY LOCALIZING  
TUMORS SUBJECT TO RESPIRATION-  
INDUCED MOTION

Kathleen T. Malinowski,  
Doctor of Philosophy, 2012

Directed By: Warren D. D'Souza, Associate Professor,  
Fischell Department of Bioengineering and  
Director, Department of Medical Physics

Tumors in the lung, liver, and pancreas can move considerably with normal respiration. The tumor motion extent, path, and baseline position change over time. This creates a complex “moving target” for external beam radiation and is a major obstacle to treating cancer. Real-time tumor motion compensation systems have emerged, but device performance is limited by tumor localization accuracy. Direct tumor tracking is not feasible for these tumors, but tumor displacement can be predicted from surrogate measurements of respiration.

In this dissertation, we have developed a series of multivariate statistical techniques for reliably and accurately localizing tumors from respiratory surrogate markers affixed to the torso surface. Our studies utilized radiographic tumor localizations measured concurrently with optically tracked respiratory surrogates during 176 lung,

liver, and pancreas radiation treatment and dynamic MR imaging sessions. We identified measurement precision, tumor-surrogate correlation, training data selection, inter-patient variations, and algorithm design as factors impacting localization accuracy. Training data timing was particularly important, as tumor localization errors increased over time in 63% of 30-min treatments. This was a result of the changing relationship between surrogate signals and tumor motion. To account for these changes, we developed a method for detecting and correcting large localization errors. By monitoring the surrogate-to-surrogate and surrogate-to-model relationships, tumor localization errors exceeding 3 mm could be detected at a sensitivity of 95%. The method that we have proposed and validated in this dissertation leads to 69% fewer treatment interruptions than conventional respiratory surrogate model monitoring techniques. Finally, we extended respiratory surrogate-based tumor motion prediction to the otherwise time-consuming process of contouring respiratory-correlated computed tomography scans. This dissertation clarifies the scope and significance of problems underlying existing surrogate-based tumor localization models. Furthermore, it presents novel solutions that make it possible to improve radiation delivery to tumors without increasing the time required to plan and deliver radiation treatments.

MULTIVARIATE STATISTICAL TECHNIQUES FOR  
ACCURATELY AND NONINVASIVELY LOCALIZING  
TUMORS SUBJECT TO RESPIRATION-INDUCED MOTION

By

Kathleen T. Malinowski

Dissertation submitted to the Faculty of the Graduate School of the  
University of Maryland, College Park, in partial fulfillment  
of the requirements for the degree of  
Doctor of Philosophy  
2012

Advisory Committee:

Dr. Warren D. D'Souza, Ph.D., Co-chair

Professor Yang Tao, Ph.D., Co-chair

Professor Jeffrey W. Herrmann, Ph.D.

Professor Peter Kofinas, Ph.D.

Professor Thomas J. Mc Avoy, Ph.D.

© Copyright by

Kathleen T. Malinowski

2012



## DEDICATION

This dissertation is dedicated to my parents. Thank you, Mom and Dad, for your love and constant support. Thank you for giving me everything I've ever needed, including setting me up with a good education from an early age. It is because of you that I have been able to complete this dissertation.

## ACKNOWLEDGMENTS

I would like to thank my Ph.D. advisor, Dr. Warren D'Souza, and my second mentor, Dr. Tom McAvoy, for their instruction, mentorship, and guidance throughout the process of this dissertation research. Thank you also to my committee co-chair Dr. Yang Tao for helping me understand Bioengineering policies and to my other committee members, Dr. Jeffrey Herrmann and Dr. Yu Chen, for participating in my dissertation defense. I would also like to acknowledge Dr. Sonja Dieterich of Stanford University for sharing data that she collected at Georgetown University Hospital and to Dr. Suresh Senan for sharing data collected at VU University Medical Center.

Finally, thank you to my fiancé, Richard, for staying with me through every step of the process (from the everyday to the big events like my proposal and my defense), for helping me through the hard times, and for following me to Maryland so that I could finish my degree.

# TABLE OF CONTENTS

DEDICATION .....	ii
ACKNOWLEDGMENTS .....	iii
TABLE OF CONTENTS .....	iv
LIST OF TABLES .....	ix
LIST OF FIGURES .....	x
CHAPTER 1: Introduction .....	1
1.1. Problem Summary .....	1
1.2. Overall Goal of the Study .....	2
1.3. Previously Published Material Included in this Dissertation .....	2
CHAPTER 2: Background .....	4
2.1. Radiation Therapy for Tumors that Move with Respiration .....	4
2.2. Tumor Immobilization .....	5
2.3. Motion-Encompassing Treatment Planning .....	6
2.4. Imaging for Tumor Motion Assessment .....	6
2.5. Real-Time Tumor Motion Management .....	7
2.5.1. Real-Time Tumor Motion Compensation Devices .....	8
2.5.2. Direct Real-Time Tumor Localization .....	10
2.5.3. Indirect Real-Time Tumor Localization .....	11
2.6. Regression Analysis for Indirect Tumor Localization .....	12
2.6.1. Ordinary Least Squares (OLS) Regression .....	13
2.6.2. Partial Least Squares (PLS) Regression .....	14
2.7. Tumor Localization During Tumor-Surrogate Relationship Changes .....	15
2.8. Statistical Process Control for Tumor Model Monitoring .....	15
CHAPTER 3: Approach .....	18
3.1. Specific Objectives of the Research .....	18
3.2. Respiratory Surrogate Model Building .....	18
3.3. Human Studies .....	21

3.3.1. Cyberknife Database .....	21
3.3.2. 4D Computed Tomography Data .....	24
3.3.3. Magnetic Resonance Imaging Study .....	26
CHAPTER 4: Mitigating Errors in Respiratory Surrogate-Based Models of Tumor Motion .....	28
4.1. Introduction .....	28
4.2. Methods .....	29
4.2.1. Position Data .....	29
4.2.2. Applying and Testing Inferential Models.....	30
4.2.3. Model Design .....	30
4.2.4. Training Data Selection.....	33
4.2.5. Inter-Patient and Inter-Fraction Variation .....	34
4.2.6. Measurement Precision .....	35
4.3. Results .....	35
4.3.1. Model Design .....	35
4.3.2. Training Data Selection.....	36
4.3.1. Tumor-Surrogate Correlation .....	37
4.3.2. Tumor Site .....	37
4.3.1. Inter-Patient and Inter-Fraction Variation .....	41
4.3.2. Measurement Precision .....	41
4.4. Discussion.....	43
4.5. Conclusions .....	46
CHAPTER 5: Incidence of Changes in Respiration-Induced Tumor Motion and its Relationship with Respiratory Surrogates During Individual Treatment Fractions.....	47
5.1. Introduction .....	47
5.2. Methods .....	48
5.2.1. Data	48
5.2.1. Tumor Location Analysis .....	49
5.2.2. Tumor Position Variation .....	50
5.2.3. Baseline Shift Detection .....	51
5.2.4. Internal-External Relationship Variation .....	52
5.3. Results .....	53
5.3.1. Tumor Positions.....	53
5.3.2. Treatment Margins .....	56
5.3.3. Baseline Shift Detection .....	58
5.3.4. Internal-External Relationships .....	58
5.4. Discussion.....	62
5.5. Conclusions .....	65

CHAPTER 6: Inferring Positions of Tumor and Nodes in Stage III Lung Cancer from Multiple Surrogates Using 4D CT .....	66
6.1. Introduction .....	66
6.2. Methods .....	68
6.2.1. 4D CT Position Data .....	68
6.2.2. Nodal Volume- and Tumor-Surrogate Correlation .....	69
6.2.3. Modeling Tumor and Nodal Volume Position with Anatomical Surrogates .....	70
6.3. Results .....	71
6.3.1. Tumor-Surrogate Correlation .....	71
6.3.1. Inferring Position of Primary Tumor and Nodes Using Anatomical Surrogates .....	74
6.4. Discussion .....	77
6.5. Conclusions .....	80
CHAPTER 7: Online Monitoring and Error Detection of Real-Time Tumor Displacement Prediction Accuracy Using Control Limits on Respiratory Surrogate Statistics .....	81
7.1. Introduction .....	81
7.2. Methods .....	83
7.2.1. Data .....	83
7.2.2. Partial Least Squares (PLS) for Predicting Tumor Positions .....	83
7.2.3. Tumor Motion Models and Model Monitoring .....	84
7.2.4. Respiratory Surrogate Metrics .....	85
7.2.5. Performance of Respiratory Surrogate-Based Monitoring .....	86
7.3. Results .....	88
7.3.1. Large Error Detection .....	88
7.3.1. Time to Error and Time to Alarm .....	90
7.3.2. Effect of Tumor Site .....	92
7.4. Discussion .....	92
7.5. Conclusions .....	96
CHAPTER 8: Maintaining Tumor Targeting Accuracy in Real-Time Tumor Motion Compensation Systems for Respiration-Induced Tumor Motion .....	98
8.1. Introduction .....	98
8.2. Methods .....	99
8.2.1. Data .....	99
8.2.2. Tumor Motion Prediction .....	100
8.2.3. Model Monitoring and Updates .....	100

8.3. Results .....	102
8.3.1. Model Errors.....	103
8.3.2. Update Timing.....	105
8.3.1. Site-Specific Results.....	106
8.4. Discussion.....	106
8.5. Conclusions .....	109
CHAPTER 9: Understanding the Performance of Control Limit-Based Monitoring of Respiratory Surrogate Tumor Motion Models.....	110
9.1. Introduction .....	110
9.2. Methods .....	111
9.2.1. Patient Data .....	111
9.2.2. Respiratory Surrogate Models of Tumor Displacement.....	119
9.2.3. Monitoring Respiratory Surrogate Models of Tumor Displacement .....	120
9.2.4. Simulations .....	121
9.3. Results .....	128
9.3.1. Imaging Study Results.....	128
9.3.2. Simulation Study Results .....	131
9.4. Discussion.....	135
9.5. Conclusions .....	138
CHAPTER 10: Conclusions .....	140
10.1. Main Objective .....	140
10.1.1. Specific Objective #1: Identify Sources of Error in Multivariate Respiratory Surrogate Tumor Localization Models.....	141
10.1.2. Specific Objective #2: Develop and Validate an Algorithm for Predicting Tumor Position from Mutliple Surrogates of Respiration .....	142
10.1.3. Specific Objective #3: Develop and Validate Methods of Monitoring Changes in Respiratory Surrogate Model Accuracy .....	144
10.2. Significance and Future Work.....	145
APPENDIX A: Institutional Review Board Approval .....	147
APPENDIX B: Selected Matlab Code.....	148
B.1 parseExternalData.....	148
B.2 func_projectData .....	150
B.3 func_lineFinder.....	150
B.4 applyPLSandSPC .....	151
B.5 func_pp_v1 .....	152
B.6 func_calcss .....	152

APPENDIX C: Selected Labview Code .....	153
C.1 Main Program for Spectra Tracking During MR Study .....	153
C.1.1 Front Panel.....	153
C.1.2 Block Diagram.....	154
C.2 Data Logging Code.....	156
C.2.1 Log File Creation.....	156
C.2.2 Logging During Tracking.....	157
C.3 Transformation from Quaternion to Cartesian Coordinates .....	158
C.2.1 Front Panel.....	158
C.2.2 Block Diagram.....	158
REFERENCES .....	159

## LIST OF TABLES

Table 4.1	Errors for models based on 6 training points, stratified by tumor site.....	40
Table 5.1	Lung tumor locations .....	49
Table 5.2	Incidence of large differences between 10 min- and 30 min-based treatment margins.....	57
Table 7.1	Summary of monitoring performance for all tumor sites at 90% and 95% sensitivity.....	90
Table 9.1.	Respiratory cycle measurements for a randomly selected surrogate marker in the first imaging session for each patient .....	124
Table 9.2.	Modeling and model monitoring performance for patient datasets .....	130
Table 9.3.	The effect of sampling rate on modeling and model monitoring performance for simulations incorporating all sources of cycle-to-cycle variation .....	134
Table 9.4.	Modeling and model monitoring performance for acquisition-time averaged training data .....	134



## LIST OF FIGURES

Figure 2.1 (a) Respiratory gating, (b) beam tracking, and (c) couch tracking technologies. ....	9
Figure 3.1 Schematic of respiratory surrogate model development and use. (1) A mathematical model is designed from a set of respiratory surrogate measurements and tumor localizations that have been captured concurrently. (2) The model is then applied to convert real-time surrogate measurements into high-frequency, noninvasive predictions of tumor position. ....	20
Figure 3.2 Four optically trackable markers affixed to the abdomen of a volunteer. ....	20
Figure 3.3. Cyberknife Synchrony suite, which includes (from left to right) the radiation treatment device (a miniature linear accelerator mounted on a robotic arm), the stereoscopic radiograph imaging system, and the respiratory surrogate marker optical tracking system. ....	23
Figure 3.4. Setup for a 4DCT scan, including a camera system at the foot of the table that optically tracks a marker fixed to the subject’s abdomen. ....	25
Figure 3.5. Optical tracking camera in position for respiratory surrogate tracking concurrent with magnetic resonance imaging. ....	27
Figure 4.1 Example of (a) 3D surrogate marker motion data (solid) projected onto its first principle component (arrow) line (dashed) to obtain (b) a 1D representation of respiration-induced surrogate marker motion. ....	31
Figure 4.2 Histogram of tumor localization errors during the first minute of testing for models based on 6 training samples. The last bin comprises all errors greater than 0.5 cm. ....	36
Figure 4.3 Mean and 95 <sup>th</sup> percentile tumor position model prediction errors in the test data acquired over 20 minutes for (a) OLSxyz, (b) PLSxyz, (c) OLSr, (d) PLSr, and (e) SYNr models. For clarity, the y-axis in (a) is scaled differently than that of (b-e). ....	38
Figure 4.4 Mean and standard deviation (error bars) of tumor position model prediction errors, binned by time elapsed since the end of training	

data collection. *The standard deviation of the OLSxyz error bar in the >20 min bin is 2.3 cm.....	39
Figure 4.5 The impact of an uncorrelated (Gaussian noise) input variable in OLSr and PLSr models. Mean and standard deviation of model errors indicate that the additional input increased errors. In the 0-2 min bin, OLSr errors increased by 57%, and PLSr errors increased by 16%. .....	39
Figure 4.6 Histograms of mean error in each fraction by tumor site for (a) OLSxyz, (b) PLSxyz, (c) OLSr, (d) PLSr, and (e) SYNr models, each based on 6 training data points.....	40
Figure 4.7 Mean and standard deviation of 9-training-datapoint PLSr in each fraction for 9 patients. Errors represent samples acquired within 20 minutes of the training dataset. For clarity, the figure is limited to the 9 patients with at least 4 treatment fractions available for analysis; the results for these patients are consistent with the dataset as a whole. ....	42
Figure 4.8 (a) Tumor and (b) external marker localization noise (in the training data used to build the model that predict tumor position) versus tumor position prediction error. Best fit lines represent least-squared-error linear regression fits with an assumption of zero error for zero noise. OLSr regression lines have slopes of (a) 1.1 and (b) 3.7. The PLSr line overlies the SYNr line in (b). ....	42
Figure 5.1 Tumor and surrogate marker (a) SI, (b) AP, (c) ML displacements for a single treatment fraction. For clarity, data from only one of the three surrogate markers is shown.....	50
Figure 5.2 Mean and standard deviation (error bars) of absolute differences in mean position of tumor (a) in subsequent (combined data from first to second and second to third) 10-min blocks of data and (b) from the first to third 10-min blocks of data.....	55
Figure 5.3 Boxplots of changes in mean tumor displacement differences between consecutive (first-to-second and second-to-third) 10-min blocks of data for upper, middle, and lower lung lobes in the (a) SI, (b) AP, and (c) ML directions. ....	55
Figure 5.4 Boxplots of differences between treatment margins calculated from the first 10 min and from the first 30 min of SI data for (a) lung and (b)	

pancreas fractions. Positive values indicate that the 30-min margin was larger than the 10-min margin.....	56
Figure 5.5 Boxplots of differences between treatment margins calculated from the first 10 min and from the first 30 min of SI data for (a) LUL, (b) LLL, (c) RUL, (d) RML, and (e) RLL lung fractions. Positive values indicate that the 30-min margin was larger than the 10-min margin. ....	57
Figure 5.6 Histogram of correlation between dtumor and dmarker for each marker and treatment fraction. ....	59
Figure 5.7 (a) Displacement from initial position for tumor (dtumor) versus displacement from initial position for surrogate markers (dmarker) with a linear least-squares best fit line ( $R^2 = 0.43$ ). (b) Residuals for linear fit line indicating the errors in predicting dtumor from the best fit line in (a).....	59
Figure 5.8 Example of a change in the relationship between AP motion of a surrogate marker and SI motion of a tumor from 1st 10-min block (circles) to the 3rd 10-min block (x's). The ratios of tumor motion to surrogate marker motion are indicated by the slopes of the least-squares fit lines: 2.8 mm tumor displacement per mm surrogate displacement and 3.6 mm tumor displacement per mm surrogate displacement.....	60
Figure 5.9 Boxplots of PLS model error (mean error in each fraction) in each of the first four 10-min blocks of data for (a) lung and (b) pancreas cases. Models were trained on the data in Block 1. Errors in each population increased monotonically for subsequent blocks of data.....	60
Figure 5.10 Proportion of (a) lung and (b) pancreas treatment fractions associated with a positive trend or no trend in model error over time when the first 10, 20, or 30 min of testing data is considered. There were no cases in which error decreased significantly over the course of the treatment fraction. ....	61
Figure 6.1 Summary of methodology employed for inferring the positions of the primary tumor and nodal volumes. ....	67
Figure 6.2 Mean and standard deviations of correlation between anatomical surrogate and tumor for surrogate (a) ML, (b) AP, and (c) SI coordinates. pt = primary tumors, nv = nodal volumes. ....	72

Figure 6.3 Proportion of primary tumor and nodal volume coordinates that are most highly correlated with each anatomical surrogate coordinate, normalized according to the quantity of data available for that anatomical surrogate. ....	73
Figure 6.4 Means and standard deviations (error bars) of OLS and PLS errors for models trained on a range (3-8) of quantities of contoured volumetric respiratory phase bin images. The standard deviation of the PLS errors is smaller and more consistent than the standard deviation of the OLS errors. ....	74
Figure 6.5 Target coordinate peak-to-peak motion vs. mean 3-phase PLS model error. Mean error (1.1 mm) for coordinates with peak-to-peak motion >0.5 cm (points in the gray area) is indicated by the dashed line. ....	76
Figure 6.6 Histogram summarizing inferred position errors of 3-phase PLS models, including all primary tumors and nodal volumes in the dataset. Errors exceeded 0.2 cm in 7% of inferred positions. ....	76
Figure 6.7 Mean and standard deviation (error bars) of 3-phase model error for nodal volumes, subdivided by zone of nodal station. ....	77
Figure 7.1 Schematic of proposed improvement to respiratory surrogate-based model monitoring. ....	82
Figure 7.2 The surrogate marker projection process. (a) Example of 3D surrogate marker motion data, including its mean and first principal component vector (blue dot and arrow, respectively) and its projection line (dashed). (b) The 1D representation of the 3D data in (a). ....	85
Figure 7.3 Receiver operator characteristic (ROC) curves showing ability to predict localization errors exceeding 3 mm for various confidence levels. ....	89
Figure 7.4 Example of (a) $T^2$ , (b) $Q^{(X)}$ , and (c) tumor localization error versus time elapsed since the training data. In (a) and (b), horizontal dashed lines represent control limits, and times in which the control limit is exceeded are shaded red. In (c), the horizontal dashed line represents a 3 mm error limit, and radiographic tumor localizations errors are indicated at $t = 0.8$ min and $t = 1.8$ min by circled x's ( $\otimes$ ). It is likely that localization errors exceed 3 mm from 0.3 to 0.5 min and after 0.9	

min, but radiographic validation is only possible at two moments over this 2 min period. ....	91
Figure 7.5 Comparison of mean time to alarm for lung and pancreas results using 2 sec of data.....	92
Figure 8.1. Timing of model updates for the four update methods in a representative treatment fraction. Updates are indicated by “x”s at the appropriate time. Results for this fraction for each method are summarized at right.....	104
Figure 8.2. Mean and standard deviation (error bars) tumor position prediction errors over 20 min for each update method. There is no significant difference ( $p>0.05$ ) between results for surrogate-based, error-based, and always update methods.....	104
Figure 8.3. Incidence of large (>3 mm and >5 mm) errors for each update method. ....	105
Figure 8.4. Numbers of model updates per 20-min fraction for each update method.....	106
Figure 9.1. Tumor localization (box) in a sagittal slice through the tumor.....	113
Figure 9.2. Stereoscopic camera system in position at the MR scanner. ....	114
Figure 9.3. Phantom marker artifact of the stereoscopic camera system. The system is unable to distinguish between the real and phantom markers when two real markers are coplanar with the two camera lenses. The dashed purple and red lines are parallel to the solid purple and red lines, respectively, and the phantom marker positions are reported at the intersections of the purple and red lines.....	116
Figure 9.4. Respiratory surrogate marker data processing for patient #1 imaging session #1. (a) Unsorted surrogate marker data. (b) Surrogate marker data replotted after automated sorting. On this plot, the user selects a box around the data known to be associated with true (non-phantom) marker data. (c) Phantom marker data circled on the sorted marker plot. ....	117
Figure 9.5. The five respiratory surrogate marker datasets projected onto one dimension in (a) a patient dataset showing gross patient motion, amplitude variations, period variations, and measurement noise but no	

baseline variations, and (b) a simulated dataset incorporating all sources of variation. .... 122

Figure 9.6. Tumor localizations (predictions) based on either a single set of respiratory surrogate marker positions (continuous blue lines) or the average of respiratory surrogate marker positions recorded over the course of 450 msec (450-msec-long red horizontal lines). .... 130

## CHAPTER 1: Introduction

### 1.1. Problem Summary

Recent advances in radiation therapy allow clinicians to plan highly conformal treatments that target radiation to the tumor while sparing the surrounding healthy tissue. However, the tumor can move out of alignment with the radiation beam during therapy. In particular, tumor motion caused by patient breathing spreads much of the radiation dose meant for the periphery of the tumor into the surrounding healthy tissue. This targeting error leads to reduced tumor control while increasing the chance that the patient will develop radiation-induced side effects.

Tracking systems that correct for tumor motion within the body by continually repositioning either the radiation beam or the tumor itself are under development. These devices rely upon accurate knowledge of the real-time tumor position. There are two ways by which real-time tumor position can be measured: (1) directly, using continuous imaging or trackable markers implanted in the tumor, or (2) indirectly, by inferring the position of the tumor from surrogate measurements of respiration.

Direct tracking systems either require unsafe levels of ionizing radiation or are only available for use in the prostate. Thus, direct tracking is not currently possible for tumors in the lung, liver, and pancreas that are subject to high-speed respiration-induced motion. Instead, surrogate measurements of respiration can be used to indirectly infer tumor displacement. Because tumors move with respiration, each respiratory surrogate

signal is partially correlated to the tumor motion. Surrogate-based systems offer the advantages of high-frequency, low-latency, and noninvasive measurements.

Surrogate-based tumor localization systems that match the accuracy and the precision of the radiation delivery are not available. To improve radiation treatment outcomes in cancer patients whose tumors move with respiration, it is necessary to develop accurate surrogate-based tracking techniques.

## 1.2. Overall Goal of the Study

The overall goal of this work was to develop multivariate statistical methods for localizing tumors from respiratory surrogates in a radiation oncology environment.

## 1.3. Previously Published Material Included in this Dissertation

The material in many of the research chapters of this dissertation has been published as journal articles, as follows:

Chapter 4 has been accepted for publication in *The International Journal of Radiation Oncology Biology and Physics* as “Mitigating errors in external respiratory surrogate-based models of tumor position” by Malinowski, K.T., McAvoy, T.J., George, R., Dieterich, S., and D’Souza, W.D.

Chapter 5 has been accepted for publication in *The International Journal of Radiation Oncology Biology and Physics* as “Incidence of changes in respiration-induced tumor motion and its relationship with respiratory surrogates during individual treatment fractions” by Malinowski, K.T., McAvoy, T.J., George, R., Dieterich, S., and D’Souza, W.D. It was published online (ahead of print) on April 16, 2011.



Chapter 6 has been published in *The International Journal of Radiation Oncology Biology and Physics* as “Inferring Positions of Tumor and Nodes in Stage III Lung Cancer from Multiple Anatomical Surrogates Using 4D CT” by Malinowski, K.T., McAvoy, T.J., George, R., Dieterich, S., and D’Souza, W.D. in 2010 Volume 77 Issue 5 pages 1553-1560.

Chapter 7 has been accepted for publication in *Medical Physics* as “Online monitoring and error detection of real-time tumor displacement prediction accuracy using control limits on respiratory surrogate statistics” by Malinowski, K., McAvoy, T.J., George, R., Dieterich, S., and D’Souza, W.D.

## CHAPTER 2: Background

### 2.1. Radiation Therapy for Tumors that Move with Respiration

Cancer can be treated through any combination of radiation therapy, surgery, and chemotherapy, but radiation therapy (or radiotherapy) is a part of the standard of care for many types of cancer. Most radiotherapy treatments (88% in 2004) are performed on a medical linear accelerator, a device that generates beams of high-energy x-rays that are delivered to the tumor through the patients' skin.<sup>1</sup> As a result, it is inevitable that over the course of treatment some radiation energy is deposited in the tissue surrounding the tumor. This radiation can damage the healthy tissue. Thus, the ultimate goal of radiation therapy is to deliver sufficient radiation to control the cancer while sparing the healthy tissue, particularly that of organs at high risk of severe radiation damage. In the lung, for instance, radiation can cause radiation pneumonitis or pulmonary fibrosis. These radiation-induced side effects are especially dangerous for lung cancer patients, who often have pulmonary comorbidities like emphysema.<sup>2</sup> Side effects of radiation therapy can be as severe as organ failure or even death.

For each radiation treatment session (called a treatment fraction), the patient is carefully aligned with the radiation beam. When the tumor is not in the expected position, radiation energy that was planned for deposition in the tumor is instead deposited in the surrounding tissue. Targeting radiation to the tumor site on each day of treatment involves two components: day-to-day alignment and intra-fraction motion. Tattoo marks,

lasers fixed in the treatment room, and in-room imaging systems are used to position the patient at the start of each day of radiation therapy. However, subsequent undetected tumor motion during the treatment fraction (intra-fraction motion) is common.

Depending on the tumor site, intra-fraction motion can be caused by any combination of muscle relaxation, gross patient movements, digestive tract activity, tissue settling, and respiration. Tumors in the lung, liver, and pancreas can move up to 2-4 cm with free breathing.<sup>3-4</sup> In the absence of motion management, respiration-induced tumor motion reduces the accuracy and effectiveness of radiation therapy to affected tumors.<sup>5-10</sup> Clinicians are guided by an American Association of Physicists in Medicine task group report, which recommends intervention when the respiration-induced tumor motion is greater than 5 mm.<sup>5</sup>

## 2.2. Tumor Immobilization

Tumor immobilization through patient breath holding, either voluntary or involuntary, has been investigated but is not a viable option.<sup>11-12</sup> The majority of lung cancer patients affected by respiration-induced tumor motion have compromised pulmonary function and cannot hold their breath for an extended period of time.<sup>2</sup> In addition, it has been shown that the tumor position may not be consistent across individual breath holds.<sup>12</sup> Similarly, abdominal compression can be used to reduce respiration-induced tumor motion, but it does not eliminate the tumor movement completely.<sup>13</sup>

### 2.3. Motion-Encompassing Treatment Planning

The International Commission on Radiation Units and Measurements (ICRU) has recommended radiating an internal margin (IM) of tissue around the planned target of radiation such that the high-dose radiation encompasses the expected intra-fraction motion.<sup>14</sup> The IM is meant to ensure that the entire tumor receives sufficient dose for tumor control. However, with an IM of a magnitude on the order of the extent of tumor motion, considerable radiation dose can be delivered to healthy tissues.<sup>5-6</sup> As a result, the prescription dose is limited by the quantity of radiation that the healthy tissue irradiated during treatment is able to tolerate.

### 2.4. Imaging for Tumor Motion Assessment

Computed tomography (CT), digital x-ray, and magnetic resonance (MR) imaging have been utilized to estimate the path and extent of tumor motion.

CT techniques are used in most clinics to volumetrically image the patient anatomy as a part of the treatment planning process. CT images are acquired over multiple respiratory cycles, leading to artifacts that misrepresent the tumor shape, volume, and position.<sup>15</sup> Slow CT scans effectively blur the tumor image over its extent of motion by oversampling the CT dataset. This is accomplished by reducing the scanner's gantry rotation speed, helical acquisition pitch, or both. Slow CT scans allow clinicians to estimate the volume through which the tumor passed during the acquisition. 4D CT scanning is also based upon oversampled CT data and is a more advanced technology. The 4D CT data is retrospectively sorted by respiratory phase such that multiple volumetric images, each representing a different portion of the respiratory cycle, can be

reconstructed. The 4D CT data can be used to characterize the tumor shape, volume, and average range of motion over an acquisition period of a few minutes. However, tumor motion over the acquisition period may not be the same as tumor motion during treatment.

Recently, MR imaging has also been used to estimate the extent of tumor motion. Dynamic MR imaging, which can capture image slices at a rate greater than 1 Hz, can provide a great deal of information about anatomy at a high temporal and spatial resolution.<sup>16</sup> Although efforts to develop an MR imaging system compatible with the linear accelerator environment are underway, it currently is not possible to obtain MR images in the radiation treatment room.

Modern linear accelerator radiation treatment machines are equipped with x-ray imaging tubes and flat-panel detectors for radiographic and fluoroscopic imaging. Pairs of orthogonal radiographic images (anterior-posterior and lateral) are used routinely in the patient setup process to align the patient with the treatment beam. Fluoroscopic images can be captured rapidly (15-30 Hz) to capture images of the moving anatomy and to compare the extent of motion with the size and shape of the treatment beam.

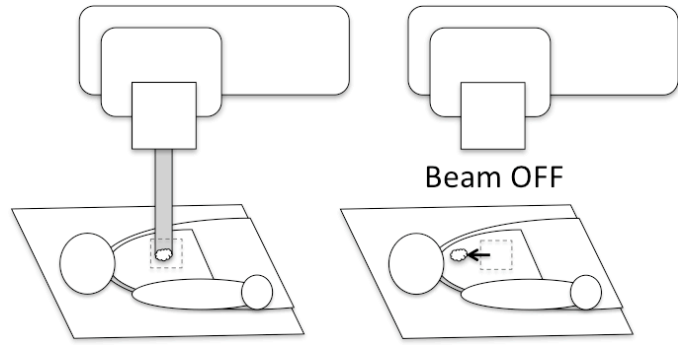
## 2.5. Real-Time Tumor Motion Management

The 5-year survival rates for lung, liver, and pancreas cancer are 16%, 6%, and 14%, respectively.<sup>17</sup> Thus, there is a great need for improving treatment techniques for these difficult-to-access, mobile tumors. Because radiation treatment planning and radiation delivery are highly precise, the efficacy of radiation treatments must be improved through increasingly accurate tumor targeting.

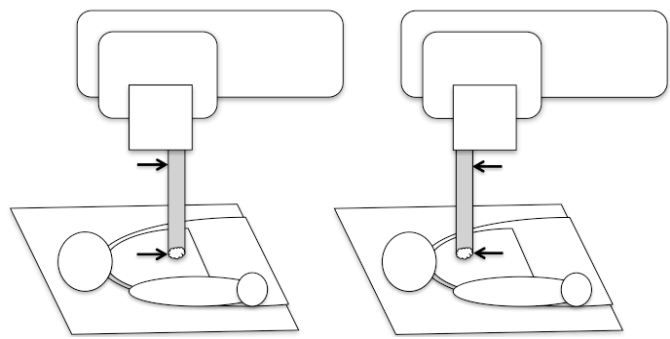
### 2.5.1. Real-Time Tumor Motion Compensation Devices

Recently, a number of real-time tumor motion management solutions have emerged. By continuously adjusting the treatment according to the instantaneous tumor position, healthy tissue can be spared without sacrificing tumor control. Existing real-time solutions include both radiation gating and tumor tracking technologies (Figure 2.1).<sup>18-20</sup> In the case of gating systems, the radiation beam is paused except during a pre-selected portion of the respiratory cycle<sup>21</sup> or while the tumor is within a limited range of positions.<sup>22</sup> Tracking systems follow the tumor with the radiation beam<sup>18,20</sup> or continuously reposition the patient such that the tumor remains stationary with respect to the radiation source.<sup>19</sup>

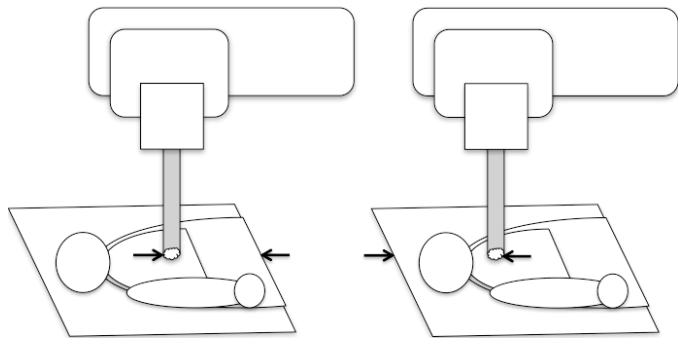
To manage tumor motion, real-time devices must precisely localize the tumor at a high frequency throughout the treatment fraction. The performance of real-time tumor motion compensation systems is closely related to the accuracy of the tumor localization.<sup>20</sup> Both direct and indirect tumor localization systems have been developed. Direct tracking systems measure the position of the tumor itself, while indirect tracking systems use other measurements to predict the instantaneous tumor displacement. A few direct tracking systems are available for clinical or research use, but these devices have considerable limitations.



(a)



(b)



(c)

Figure 2.1 (a) Respiratory gating, (b) beam tracking, and (c) couch tracking technologies.

### 2.5.2. Direct Real-Time Tumor Localization

The first direct tracking system to be introduced to the radiation oncology community was described by Shirato *et al.*<sup>23</sup> This device uses a dual-detector fluoroscopy system to localize the tumor through continuously captured x-ray images. This system must be active throughout each 20-60 min treatment fraction, during which time significant ionizing radiation is imparted to the patient's body. Because of the risk associated with the ionizing radiation delivered to the patient, this device is not expected to gain FDA approval for clinical use in the United States.

A second direct tracking technology is the Calypso 4D Localization System (Varian Medical Systems, Palo Alto, CA).<sup>24</sup> The Calypso system utilizes non-ionizing electromagnetic radiation to localize wireless transponders that are implanted in or near the tumor. This system is only approved for use in the prostate. Research has shown that the transponders do not remain fixed in lung tissue and therefore cannot be used to track lung tumor motion.<sup>25</sup>

The third direct tumor tracking system was recently introduced by Navotek Medical Lt. (Yokneam, Israel). To utilize this device, a fiducial marker containing 100  $\mu\text{Ci}$  of radioactive Ir-192 is implanted in or near the tumor. A tracking system comprising radiation detectors localizes the fiducial marker during the treatment.<sup>26</sup> Like the Calypso system, this device is seeking initial approval for use in the prostate.<sup>27</sup> Because the Navotek fiducial markers are even smaller than those of the Calypso system,<sup>26</sup> implantation in the lung is likely to be problematic.



### 2.5.3. Indirect Real-Time Tumor Localization

Indirect tracking systems use a measurement of some surrogate of respiration to infer the respiration-induced motion of the tumor. Previously investigated respiratory surrogates include torso surface motion,<sup>3,6,28-30</sup> spirometrically measured tidal volume and air flow,<sup>6,30-31</sup> and the motion of internal anatomical structures visible in x-ray images.<sup>29,32</sup> Of these, torso surface motion is the least invasive and the safest for the patient.

Torso surface motion is partially correlated with respiration-induced tumor motion.<sup>3,30,33</sup> The magnitude of the correlation varies by tumor site and location, by the position of markers on the torso surface, and over time. Because of these variations, a different respiratory surrogate model must be developed for each treatment session and patient. To predict tumor motion from respiratory surrogate measurements, a small set of gold-standard tumor localizations must be captured concurrently with respiratory surrogate measurements. This data makes it possible to develop an understanding of the relationship between tumor motion and surrogate signals.

The most commonly used respiratory surrogate device tracks the anterior-posterior (AP) motion of a marker placed on the abdomen of a supine patient (Real-time Position Management, RPM, Varian Medical Systems, Palo Alto, CA). Tumor motion in each dimension is assumed to be linearly related to the AP marker motion. However, this assumption can lead to significant radiation targeting errors.<sup>28,34-35</sup>

The accuracy of existing surrogate tumor motion prediction systems may not be sufficient for high-precision radiation therapy systems.<sup>21</sup> The first specific objective of

this dissertation is to identify and quantify sources of error in multivariate respiratory surrogate tumor localization models.

## 2.6. Regression Analysis for Indirect Tumor Localization

Combining multiple surrogate signals into a single model of tumor motion has been recommended as a means to create accurate respiratory surrogate-based tumor motion models.<sup>33,36,38</sup> By incorporating multiple surrogates into one model, the marker placement effect, differences between respiratory surrogate paths of motion and tumor paths of motion, and phase offsets between motion of the tumor and motion of the torso surface can be overcome.<sup>3,28,35-36,39</sup>

To predict tumor displacement from respiratory surrogate signals, a mathematical model describing the relationship between tumor motion and surrogate measurements must be developed. Because the literature lacks direct, quantitative comparisons of existing multiple-input models, there is no consensus on the best mathematical approach for modeling tumor motion from multiple markers. The second specific objective of this dissertation is to develop and validate an algorithm for predicting tumor position from multiple surrogates of respiration.

In this dissertation, we developed novel techniques for localizing tumors based upon multilinear regression analysis. Regression analysis is a technique by which the form and accuracy of a relationship between outputs and inputs can be estimated.<sup>40</sup> When applied to respiratory surrogate inputs, the relationship between each dimension (anterior-posterior, AP, superior-inferior, SI, and medial-lateral, ML) of tumor motion and each respiratory surrogate signal can be estimated. If a linear relationship is assumed,

the outputs are estimated as a sum of linearly scaled inputs. The linear regression yields a model of the form  $\hat{Y} = X \cdot B$ , where  $\hat{Y}$  is the  $n \times 3$  matrix of estimated 3D tumor positions,  $X$  is the  $n \times m$  matrix of respiratory surrogate signal measurements at  $n$  samples, and  $B$  is an  $m \times 3$  matrix of regression coefficients. In this dissertation work, two multilinear regression techniques were explored: ordinary least squares (OLS) regression and partial least squares (PLS) regression. These techniques provide alternative solutions to the equation  $\hat{Y} = X \cdot B$ .

### 2.6.1. Ordinary Least Squares (OLS) Regression

The OLS method defines  $B$  as the set of regression coefficients that result in the smallest possible sum of squared errors,  $\sum_j \sum_i (\hat{Y}_{i,j} - Y_{i,j})^2$ , for approximate and actual target positions  $\hat{Y}$  and  $Y$ , respectively, at time  $i$  and for direction of tumor motion  $j$ . The unique OLS solution is given by  $B = X^+ \cdot Y$ , where  $X^+$  is the Moore-Penrose pseudo-inverse of  $X$ . For full-rank, real  $X$ , the Moore-Penrose pseudo-inverse is defined as  $X^+ = X^T / (X^T \cdot X)$ . For rank-deficient, real  $X$ ,  $X^+ = V \cdot \Sigma^+ \cdot U^T$ , where  $U$ ,  $\Sigma$ , and  $V$  are the matrices in the singular value decomposition of  $X$  given by  $X = U \cdot \Sigma \cdot V$ . The terms of  $\Sigma^+$  are given by  $\Sigma_{i,j}^+ = (\Sigma_{i,j})^{-1}$  for  $\Sigma_{i,j} \neq 0$  and  $\Sigma_{i,j}^+ = 0$  for  $\Sigma_{i,j} = 0$ .

### 2.6.2. Partial Least Squares (PLS) Regression

PLS regression is a technique that yields a coefficient matrix,  $B$ , in  $\hat{Y} = X \cdot B$  such that the expression  $\frac{1}{2}B^T \cdot X^T X \cdot B - (X^T Y)^T \cdot B$  is minimized. In this dissertation, the SIMPLS algorithm<sup>41</sup> was used to calculate the regression coefficients.

The SIMPLS algorithm involves sequentially determining the  $A$  scores, weights, and loadings associated with  $X$  and  $Y$ .  $X$  is compressed into an  $m \times A$  matrix of scores (or latent variables),  $T = [t_1, t_2, \dots, t_A]$ , where  $A < m$ . The latent variables of  $Y$ ,  $u_i$  for  $i = 1$  to  $A$ , are linear combinations of the columns of  $Y$  that are chosen so as to maximize the covariance between  $t_i$  and  $u_i$  for each  $i$ . The first  $X$  score,  $t_1$ , is given by  $t_1 = X \cdot X^T \cdot Y_0 / \text{norm}(X \cdot X^T \cdot Y)$ , where  $Y_0$  is mean-centered  $Y$ . The first  $X$  weight,  $r_1$ , and the first  $X$  basis,  $v_1$ , each have elements equal to one. The  $Y$  loadings and scores are calculated as  $q_i = Y_0^T \cdot t_i$  and  $u_i = Y_0 \cdot q_i$ , respectively. The  $X$  basis is updated with each iteration as  $v_i = v_{i-1} - V_{i-1} \cdot (V_{i-1}^T \cdot (t^T \cdot X)^T)$ , where  $V_{i-1} = [v_1, v_2, \dots, v_{i-1}]$ . Subsequent  $X$  weights and scores are calculated as  $r_i = (S_{i-1} - v_i \cdot (v_i^T \cdot S_{i-1})) \cdot q_i$  and  $t_i = X \cdot r_i$ .

Because the PLS algorithm determines scores in order of decreasing contribution to the PLS model, utilizing only the first  $A$  of  $m$  factors serves to select the input information most relevant to the outputs. Thus the score and loading matrices were compressed as  $X = \hat{T} \cdot \hat{W} + E$  and  $Y = \hat{U} \cdot \hat{Q} + F$ , where  $\hat{T}$  was the  $n \times A$  matrix  $\hat{T} = [t_1, t_2, \dots, t_A]$ ,  $\hat{W}$  was the  $m \times A$  matrix  $\hat{W} = [w_1, w_2, \dots, w_A]$ ,  $\hat{U}$  was the  $n \times A$  matrix  $\hat{U} = [u_1, u_2, \dots, u_A]$ , and  $\hat{Q}$  was the  $p \times A$  matrix  $\hat{Q} = [q_1, q_2, \dots, q_A]$ . The residual matrices were  $E$  and  $F$ . Cross-validation approaches such as the leave-one-out and bootstrap

methods<sup>42</sup> were used to select the appropriate number of factors,  $A$ , for each training dataset. The regression coefficient matrix,  $B$ , was given by  $B = \hat{R} \cdot \hat{Q}^T$ , where  $\hat{R} = [r_1, r_2, \dots, r_A]$  and  $\hat{Q} = [q_1, q_2, \dots, q_A]$ .

## 2.7. Tumor Localization During Tumor-Surrogate Relationship Changes

Respiratory surrogate models of tumor motion only work as long as the tumor-surrogate relationship remains constant.<sup>6</sup> However, researchers have documented changes in relative motion amplitudes, drifts in the baseline tumor position, drifts in the surrogate signals, and shifts in the phase offset between the tumor and surrogate motion.<sup>6,43-44</sup>

Inconsistencies in the day-to-day relationship between tumor motion and external surrogate signals have led researchers to recommend assessing such changes by imaging prior to the start of each treatment fraction.<sup>44-46</sup> However, tumor-surrogate relationship changes have been detected during the duration of a single treatment fraction.<sup>6,47</sup> To maintain respiratory surrogate model accuracy throughout a radiation treatment, it is necessary to periodically create a new model based on additional gold-standard tumor localizations. The third specific objective of this dissertation is *to develop and validate methods for monitoring changes in respiratory surrogate model accuracy*.

## 2.8. Statistical Process Control for Tumor Model Monitoring

In this dissertation work, we developed a set of methods for monitoring respiratory surrogate-based tumor motion models. These monitoring methods are based statistical process control techniques.

Statistical process control (SPC) is a class of statistical techniques in which new observations are compared to observations captured while the system was operating under control. Specifically, SPC metrics, as plotted versus time on control charts,<sup>48</sup> increase as changes occur in the observations relative to one another and relative to the model. These metrics, therefore, can rapidly detect the external disturbances that degrade the validity of the process under study.

In the case of respiratory surrogate models, the respiratory surrogate measurements captured during the model-building period can be compared to the respiratory surrogate measurements captured during treatment. In this dissertation work, Hotelling's  $T^2$  statistic and the input variable squared prediction error ( $Q^{(X)}$ ), were used to monitor the tumor-surrogate relationship through surrogate measurements alone, without halting the radiation beam to directly measure the tumor position. Both of these metrics are compatible with PLS regression and utilize the latent variables, or scores, that are developed as part of the regression process.

Hotelling's  $T^2$  statistic is an extension of the student's t-test to multiple dimensions. In this work,  $T^2$  was used to measure the variation amongst the respiratory surrogate-based PLS input scores,  $t_i$ .<sup>49</sup> Aberrant  $T^2$  values indicate that the relationship between latent variables differs from that of the PLS model training data and that the model therefore must be extrapolated to fit the new respiratory surrogate data.  $T^2$  was

calculated as  $T_i^2 = t_i^T \cdot \left( \frac{\hat{T}_i^T \cdot \hat{T}_i}{n-1} \right)^{-1} \cdot t_i$ . The  $(1 - \alpha)$  percentile confidence limit on  $T^2$  was

calculated as  $T_\alpha^2 = \frac{(n^2 - 1)A}{n(n - A)} F_\alpha(A, n - A)$ ,  $n$  was the number of training samples used to generate the model,  $A$  was the number of scores utilized by the PLS model, and  $F_\alpha(A, n - A)$  was the upper ( $\alpha \times 100\%$ ) critical point of the  $F$  distribution with  $(A, n - A)$  degrees of freedom.

The input variable squared-prediction-error,  $Q^{(X)}$ , detects events that cause the process to move away from the hyper-plane defined by the reference model.<sup>50</sup>  $Q^{(X)}$  was

given by  $Q_i^{(X)} = \sum_{j=A+1}^n (\hat{z}_{ij} - z_{ij})^2$ , where  $\hat{z}_i = t_i \cdot \hat{W}$  represents the surrogate marker

measurement vector at sample  $i$ ,  $z_i$ , compressed to  $A$  latent variables. Confidence limits on  $Q^{(X)}$  were calculated through the Jackson-Mudholkar formula,<sup>51</sup>

$Q_\alpha = \theta_1 \left[ 1 - \frac{\theta_2 h_0 (1 - h_0)}{\theta_1^2} + \frac{z_\alpha \sqrt{2\theta_2 h_0^2}}{\theta_1} \right]^{1/h_0}$ , in which  $z_\alpha$  is the upper (100%)·( $\alpha$ ) critical

point of the normal distribution,  $\theta_j = \sum_{k=A+1}^N \lambda_k^j$ ,  $h_0 = 1 - \frac{2\theta_1 \theta_3}{3\theta_2^2}$ , and  $\lambda_k$  is the  $k$ th eigenvalue

of  $(\hat{z}_{new,i} - z_{new,i})^T (\hat{z}_{new,i} - z_{new,i})$ .

## CHAPTER 3: Approach

### 3.1. Specific Objectives of the Research

The purpose of this work was to develop multivariate statistical techniques for localizing tumors from respiratory surrogates in a radiation oncology environment. The specific objectives of this research were:

1. To identify and quantify sources of error in multivariate respiratory surrogate tumor localization models,
2. To develop and validate an algorithm for predicting tumor position from multiple surrogates of respiration, and
3. To develop and validate methods for monitoring changes in respiratory surrogate model accuracy over time.

### 3.2. Respiratory Surrogate Model Building

To develop methods for localizing tumors with respiratory surrogates, it was necessary to evaluate respiratory surrogate models developed under a variety of conditions. Respiratory surrogate models are based upon concurrent measurements of tumor and respiratory surrogate marker positions. These concurrent measurements make it possible to develop a mathematical model describing tumor displacement as a function of respiratory surrogate measurements. Because of variations in patient anatomy, tumor size and position, breathing patterns, and respiratory surrogate setup, surrogate models of tumor motion must be redeveloped for each patient and day of treatment. Only after the



mathematical model is developed with gold-standard tumor localization data can subsequent tumor positions be predicted from respiratory surrogate measurements alone (Figure 3.1).

The data used to develop and test the respiratory surrogate models was acquired from volunteers in three human imaging studies (Section 0). Two components, high-frequency external localization and low-frequency internal localization, comprised each study. The external surrogates of respiration in each of these studies were optically tracked markers placed on the abdominal surface to allow monitoring of abdominal surface displacement during breathing. The markers were affixed to the subject either with adhesive tape (Figure 3.2) or with hook-and-loop fasteners and a form-fitting vest.<sup>52</sup> The internal localization was accomplished by identifying the tumor in radiographic, computed tomography (CT), or magnetic resonance (MR) images.

Of note, it is not possible to localize the tumor at a high frequency throughout a radiation treatment fraction using images, because imaging modalities compatible with radiation delivery devices emit ionizing radiation (Section 2.5.2). Instead, because of the retrospective nature of this work, the images in this study were captured at a lower frequency (radiographs, CT) or through a modality incompatible with radiation delivery (MR).

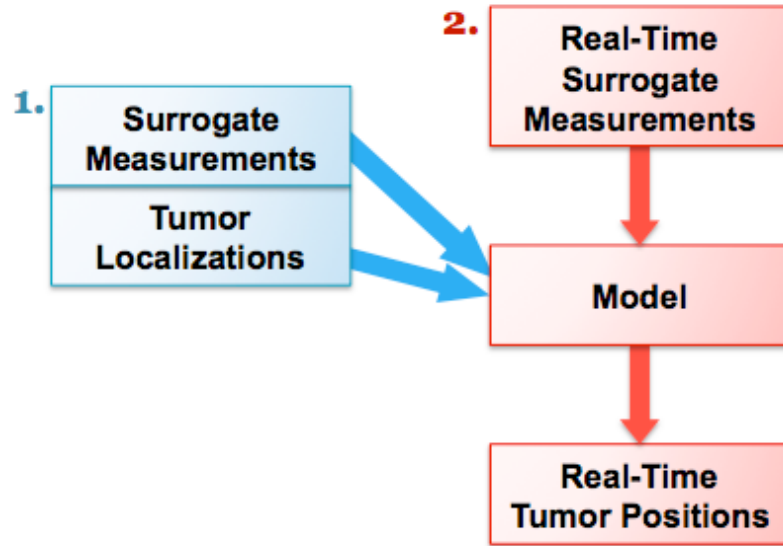


Figure 3.1 Schematic of respiratory surrogate model development and use. (1) A mathematical model is designed from a set of respiratory surrogate measurements and tumor localizations that have been captured concurrently. (2) The model is then applied to convert real-time surrogate measurements into high-frequency, noninvasive predictions of tumor position.

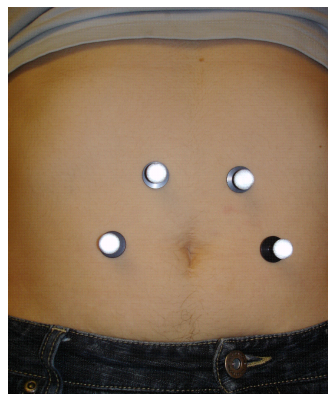


Figure 3.2 Four optically trackable markers affixed to the abdomen of a volunteer.

Models of tumor motion were developed and tested using in-house-developed Matlab (Mathworks, Natick, MA) code, which utilized the Partial Least Squares (PLS) code provided by the PLS\_Toolbox (Eigenvector Research Incorporated, Wenatchee, WA). A selection of Matlab code written for this purpose is included in Appendix B.

### 3.3. Human Studies

The specific objectives of this work were accomplished in six studies included as chapters of this dissertation work. Each study utilized one of three human imaging datasets described below.

#### 3.3.1. Cyberknife Database

Data was obtained under Institutional Review Board approval. A total of 91 cancer patients, including 63 with lung tumors, 5 with liver tumors, and 23 with pancreas tumors, underwent stereotactic body radiation therapy using a Cyberknife Synchrony<sup>TM</sup> (Accuray, Sunnyvale, CA) system at Georgetown University Hospital. Each patient underwent 1-5 treatment sessions. The Georgetown University Institutional Review Board approved sharing of an anonymized version of this dataset with research partners, including our group at the University of Maryland.

In the course of a usual treatment, the Cyberknife Synchrony<sup>TM</sup> system (Figure 3.3) records both tumor and torso surface positions. For this patient population, three respiratory surrogate markers in the form of light-emitting diodes (LEDs) were fixed to a form-fitting vest worn by the patient. The LED surrogate markers were optically tracked at a rate of 26 Hz throughout the treatment. Second, using a pair of stereoscopic

radiographs, the centroid of 2-3 fiducial markers implanted in or near the tumor was localized every 3 radiation beams delivered, once per minute on average. The fiducial marker centroid displacement was considered to be equivalent to the tumor displacement. The tumor and surrogate marker localizations were aligned using timestamps in the log files.

The raw Cyberknife Synchrony<sup>TM</sup> system data files were processed in Matlab (Mathworks, Natick, MA). Periods of tracking while the patient was being repositioned were removed from the dataset. For each imaging session, the longest period of tracking between repositioning events was utilized in the analyses. Each tracking period included at least 40 tumor localizations.

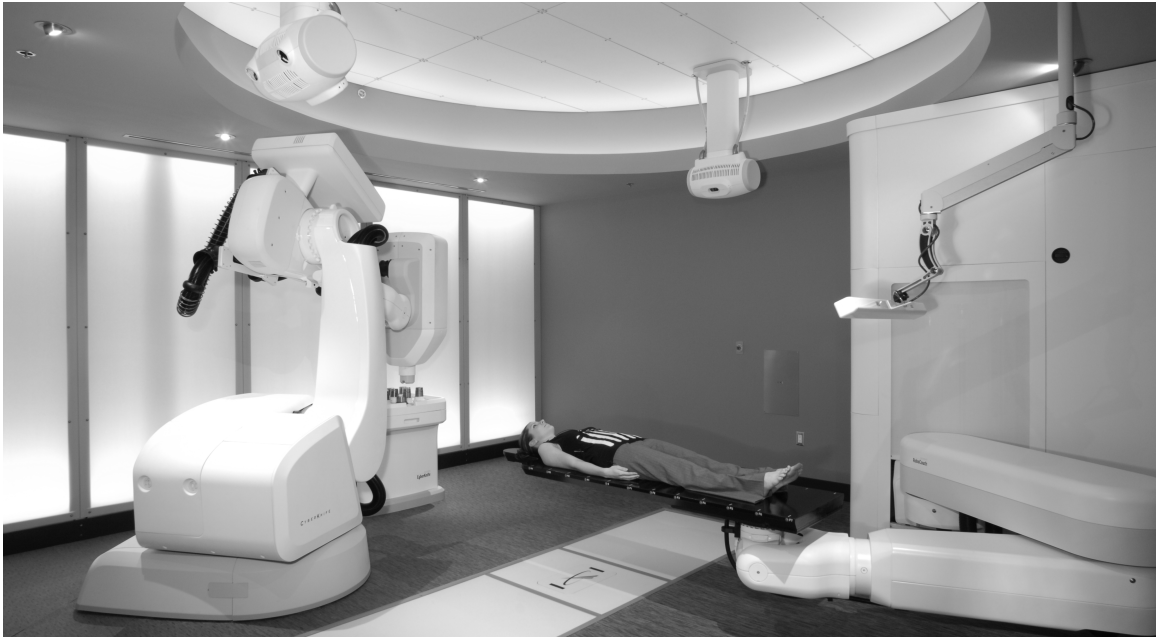


Figure 3.3. Cyberknife Synchrony suite, which includes (from left to right) the radiation treatment device (a miniature linear accelerator mounted on a robotic arm), the stereoscopic radiograph imaging system, and the respiratory surrogate marker optical tracking system.

### 3.3.2. 4D Computed Tomography Data

A retrospective analysis of planning 4D computed tomography (CT) scans was evaluated to determine whether easily localized anatomical landmarks in the chest are predictive of lung primary tumor and lung nodal volume motion. Sixteen patient scans with clearly demarcated mediastinal lymph nodes and without imaging artifacts were selected from the VU University Medical Center (Amsterdam, Netherlands) database of planning 4D CT scans.

Patients were scanned in the supine position on a 16-slice CT scanner (LightSpeed 16, GE Healthcare, Waukesha, WI) with no intravenous contrast (Figure 3.4). Scans were performed in cine acquisition mode at 2.0 cm intervals with a slice thickness of 2.5 mm. Patients were instructed to breathe normally with a regular rhythm, and images were obtained only after a quiet, regular breathing pattern was observed. The respiratory signal was detected using a Real-time Position Monitoring (RPM) system (Varian Medical Systems, Palo Alto, CA). The CT imaging data and corresponding respiratory signal files were binned into 10 separate respiratory phases by dividing each RPM-derived respiratory cycle into 10 equal time intervals. The phases were labeled from 0% to 90%, with end-inspiration corresponding to the 0% bin.

A single radiation oncologist manually contoured the primary tumors and the thoracic nodal volumes and localized the anatomical respiratory surrogates, and a second radiation oncologist verified the contours. Depending on their visibility in the 4D CT scan, 3-5 anatomical surrogates were tracked for each patient. The anatomical surrogates were xyphoid (n=16), carina (n=16), left (n=7) and right (n=11) nipples (tracked in male

patients only), and mid-sternum (n=15). The mid-sternum was localized as a metal marker placed on the sternum at the time of 4D CT in the images. The carina was localized as the peak between main-stem bronchi on coronal image slices, which had been automatically interpolated by the treatment software. In total, 3D position data from 16 primary tumors, 53 nodal volumes, and 65 anatomical surrogates from the 16 patients were analyzed.



Figure 3.4. Setup for a 4DCT scan, including a camera system at the foot of the table that optically tracks a marker fixed to the subject's abdomen.

### 3.3.3. Magnetic Resonance Imaging Study

Five lung cancer patients undergoing radiation therapy at the University of Maryland Department of Radiation Oncology participated in an Institutional Review Board-approved magnetic resonance (MR) imaging study at the University of Maryland Medical Center. The study participants underwent dynamic (high-frequency) MR scanning on three separate days. The first scan took place 1-2 weeks prior to the start of the patient's radiation treatments. The second scan took place between the 5<sup>th</sup> and 11<sup>th</sup> treatments for patients undergoing conventionally fractionated radiation therapy or between the 1<sup>st</sup> and 2<sup>nd</sup> treatments for patients undergoing hypo-fractionated radiation therapy. The third scan took place between the 15<sup>th</sup> and 21<sup>th</sup> treatments for patients undergoing conventionally fractionated radiation therapy or between the 2<sup>nd</sup> and last treatments for patients undergoing hypo-fractionated radiation therapy.

Images of the tumor were acquired on a 1.5 T Magnetic Resonance Imager (Manetom Avanto, Siemens, Erlangen, Germany) using a TrueFISP sequence (200 images, 5 sagittal slices, 8 mm slice thickness, interleaved acquisition, TE 1.29 ms, TR 2.57 ms, 60deg flip angle, matrix 176 × 256 matrix, in-plane spatial resolution of 1.6-2.2mm in each direction, 1028 bandwidth, 500 sec total acquisition time). The FOV was selected to encompass the tumor and the tumor motion in the medial-lateral dimension and to encompass the thorax in each sagittal slice.

During scan acquisition, five spherical reflective markers affixed to the abdomen were tracked (Figure 3.5) by an infrared camera system (Polaris Spectra, NDI, Waterloo, Ontario) using in-house developed software (Labview, National Instruments, Austin,



Texas). The software was designed to poll the camera for marker positions at a rate of 30-60 Hz, parse the response, log the positions, and synchronize marker tracking with MR image acquisition. The software emits a voltage pulse through a DAQ board once every 500 msec. The scanner receives this signal through its electrocardiogram input hardware. The scan sequence was programmed to acquire one image slice per pulse. This scheme ensures that marker position logging is synchronized with the MR acquisition. Developing this software involved modifying the available Labview drivers designed for the older Polaris camera system for compatibility with the Polaris Spectra camera system used in this study. Selected Labview code written for this project is included in APPENDIX C: Selected Labview Code.

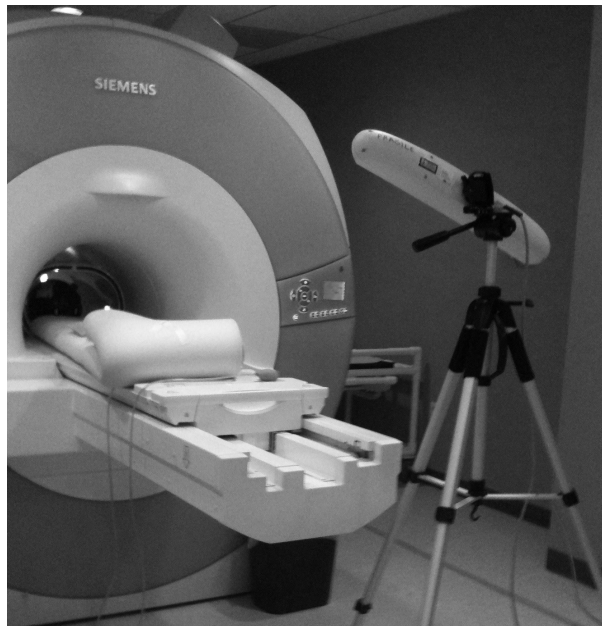


Figure 3.5. Optical tracking camera in position for respiratory surrogate tracking concurrent with magnetic resonance imaging.

## CHAPTER 4: Mitigating Errors in Respiratory Surrogate-Based Models of Tumor Motion

### 4.1. Introduction

Respiration-induced tumor motion degrades radiation therapy targeting accuracy.<sup>5,9-10</sup> Tumor displacement can be inferred by indirect tracking systems that rely on external surrogates of respiratory motion, such as optical markers affixed to the torso, to predict the position of the tumor.<sup>18,21,33,36-37,53-54</sup> However, few studies to date explore potential variations in the model or explain sources of error. While the literature has suggested that such issues as signal-to-noise ratio (SNR)<sup>34</sup> and variations in the tumor-surrogate relationship<sup>3,6,30,45</sup> might lead to indirect tumor tracking system errors, to our knowledge *no study to date has provided a systematic investigation of factors that may contribute to the accuracy of surrogate-based predictive models of tumor position.* This information would make it possible to more accurately track real-time tumor motion.

In this study, we evaluate potential sources of error in tumor position prediction models. The primary *purpose of this study was to investigate the impacts of: (1) tumor site, (2) tumor and external surrogate measurement precision, (3) tumor-surrogate correlation, (4) training data selection, (5) model design, (6) inter-patient variations, and (7) inter-fraction variations on the accuracy of external marker-based models of tumor position* in the context of three modeling algorithms: ordinary least squares (OLS)

regression, the Cyberknife Synchrony™ algorithm, and partial least squares (PLS) regression. The secondary goal of this study was to evaluate PLS regression for modeling tumor motion from external surrogates. Preliminary studies<sup>37</sup> have indicated that PLS may be more accurate than computationally simpler multiple-marker linear algorithms such as OLS and Synchrony.™ This may be due to the collinearity in external markers' motion.<sup>40</sup>

## 4.2. Methods

### 4.2.1. Position Data

Data consisted of Cyberknife Synchrony™ system (Accuray Inc., Sunnyvale, CA) log files captured during 113, 10, and 44 stereotactic body radiation therapy treatments from 61, 5, and 22 lung, liver, and pancreas patients, respectively, at Georgetown University Hospital, Washington, DC. An Institutional Review Board approved the collection of this data and the distribution of de-identified data from this study to research partners.

Cyberknife Synchrony™ data files included 3D positions of: (1) the centroid of a set of 2-3 fiducial markers implanted in the tumor that were measured via stereoscopic x-rays, henceforth referred to as the tumor position; and (2) three markers affixed to the patient's form-fitting vest that were tracked optically. The positions of the tumor, identified as the centroid of the set of fiducial markers, were aligned in time with those of the external respiratory surrogate markers according to the timestamps in the system log files. Each dataset included 40-112 (mean = 62) concurrent tumor and marker localizations spaced at a mean interval of 66 sec. The log files also included the

continuous real-time output of the Cyberknife Synchrony™ model predicting tumor motion from respiratory surrogate marker motion.

#### 4.2.2. Applying and Testing Inferential Models

For each treatment fraction, a series of models was tested. First, a model was fit (Section 4.2.3) to a training dataset of the first  $N$  concurrent tumor and external marker positions in the treatment fraction. This model was used to predict tumor positions from subsequent external marker measurements in the same treatment fraction. Each predicted tumor position, derived from marker measurements alone, was validated against the tumor position measured from stereoscopic x-rays. This process was repeated for training datasets of each set of  $N$  consecutive measurements in the treatment fraction, each time testing the model against the tumor localizations during that fraction that were acquired after the training dataset. Prediction error was defined as the Euclidean distance between the stereoscopic x-ray-measured tumor position and the modeled tumor position.

#### 4.2.3. Model Design

##### 4.2.3.1. Input Data Pre-Processing

In addition to the raw external marker positions, an alternative input was created by projecting marker displacements onto a single dimension of motion, defined as  $r_i$  (Figure 4.1). The motivation for comparing raw 3D inputs to projected, 1D inputs was to better understand the impact of this data processing technique on the Cyberknife Synchrony™

algorithm's performance. As described by Sayeh *et al.*, the Cyberknife Synchrony<sup>TM</sup> system uses  $r_i$  as the inputs to its tumor position models.<sup>52</sup>

To calculate  $r_i(t)$  for a marker  $i$ , the projection line was determined from the matrix of mean-centered 3D marker positions acquired during training data collection. The direction of the line was given by the first principal component vector of the marker positions, which is defined as the first eigenvector of the marker data covariance matrix.<sup>55</sup> The projection line also was designed to intersect the origin. Each 3D marker position was then projected orthogonally onto the line. For each position  $(x_i(t), y_i(t), z_i(t))$ ,  $r_i(t)$  was defined as the distance from the origin to the sample's projected position.

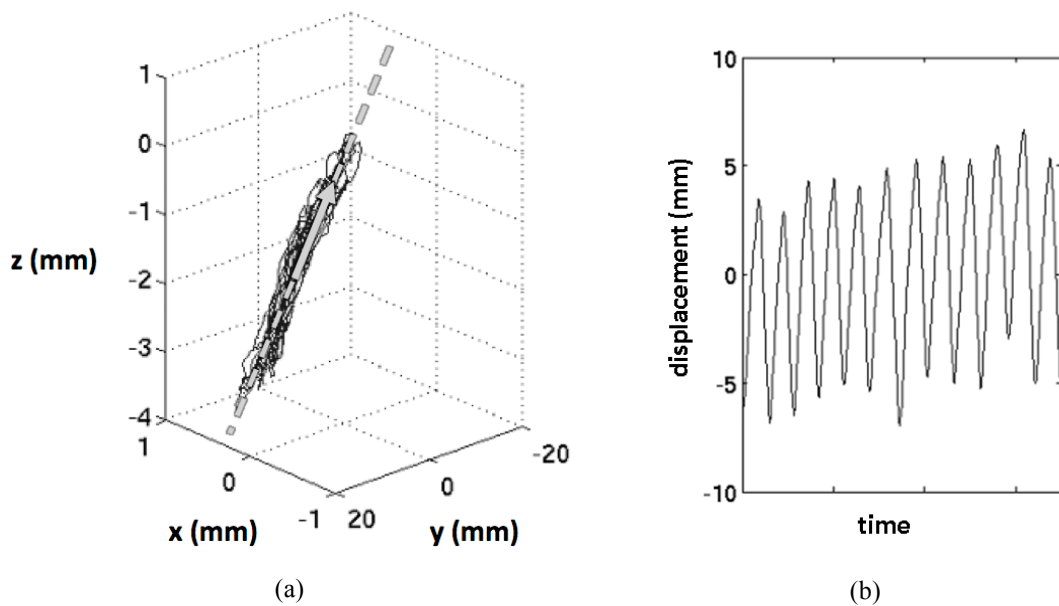


Figure 4.1 Example of (a) 3D surrogate marker motion data (solid) projected onto its first principle component (arrow) line (dashed) to obtain (b) a 1D representation of respiration-induced surrogate marker motion.

#### 4.2.3.2. Model Algorithms

Three model fitting algorithms were considered: OLS regression, PLS regression, and the Synchrony™ algorithm. OLS and PLS are multilinear models of the form  $\hat{Y} = X \cdot B$ , where  $X$  is matrix of inputs (respiratory surrogate positions) with  $m$  measurements and  $n$  inputs,  $B$  is an  $n \times 3$  matrix of regression coefficients, and  $\hat{Y}$  is a matrix of  $m \times 3$  outputs (predicted tumor positions). See Section 2.6 for details regarding how to calculate  $B$  through OLS and PLS, respectively.

The inferential model in the Synchrony™ system was reproduced for this study based on the description by Sayeh *et al.* While the Synchrony™ output was available in the system log files, reproducing the model made it possible to control the training data and timing in order to compare results to that of OLS and PLS models.<sup>52</sup> The algorithm can be stated briefly as follows. Initially, separate linear, quadratic, or hybrid models were developed for each of the three markers. The linear and quadratic models were defined by  $\hat{Y}_i = A_{1,i}r_i + A_{0,i}$  and  $\hat{Y}_i = A_{2,i}r_i^2 + A_{1,i}r_i + A_{0,i}$ , respectively. For quadratic and hybrid models, separate coefficients were calculated for inhalation and exhalation. The final tumor position estimate was given by the average of the outputs of models using the three markers. The system selects between linear or quadratic models through a modified standard error function that selects for increased accuracy and reduced computational complexity.<sup>52</sup> In the clinical Cyberknife Synchrony™ system, the operator selects both the number of images used to train the model and the frequency of images acquired during treatment. Our implementation of the Synchrony™ model, SYNr, based on 15

tumor localizations (the typical training data length in the clinic from which our data originated) was validated against the actual logged 15-sample Synchrony™ model output. In the SI, ML and AP directions, respectively, the mean ( $\pm$  standard deviation) distances between SYNr and actual Synchrony™ outputs were  $0.5 \pm 1.2$  mm,  $0.5 \pm 1.7$  mm, and  $0.3 \pm 0.5$  mm. For this study, only the linear form was considered, because more than 70% of cases in the database did not utilize quadratic models when the modified standard error function was applied.

Both the OLS and the SYNr algorithms utilize an ordinary linear regression step. The SYNr algorithm differs from OLS in that SYNr creates separate linear models for each of the 3 markers and averages their outputs to predict the tumor position. In contrast, the OLS model regresses on one matrix comprising all of the marker data, leading to a different set of regression coefficients.

#### 4.2.3.3. Summary of Models Evaluated

Five tumor position prediction models were considered: OLSxyz, OLSr, PLSxyz, PLSr, and SYNr. OLSxyz and PLSxyz models utilized the 3D marker data. OLSr, PLSr, and SYNr models utilized the one-dimensional, projected marker data.

#### 4.2.4. Training Data Selection

##### 4.2.4.1. Quantity of Training Data

Training datasets of  $N = 6$  to  $N = 35$  samples of measured tumor and external surrogate positions were evaluated for their accuracy in inferring tumor positions that occurred

subsequent to the training data. Mean and 95<sup>th</sup> percentile errors over 20 minutes of data were evaluated.

#### 4.2.4.2. Time Since Training Data Acquisition

Errors for models in which 6 samples of concurrent external marker and tumor positions comprised the training data were binned by time elapsed since the end of training data.

#### 4.2.4.3. Tumor-Surrogate Correlation

The impact of uncorrelated external surrogate inputs on tumor localization model accuracy was explored in OLSr, PLSr, and SYNr models. For each model type, models with 6 samples of concurrent external marker and tumor position were created. Then new models were trained on the same training data (6 samples  $\times$  3 inputs) plus an additional input vector of Gaussian noise (6 random values  $\times$  1 input) for a total of 4 inputs. The accuracies of models with and without the additional noise input were compared.

#### 4.2.5. Inter-Patient and Inter-Fraction Variation

Each patient underwent 1-5 treatment fractions. The mean tumor-surrogate model prediction error for each treatment fraction was determined. Using the 46 patients for whom more than one treatment fraction of data was available, the Kruskal-Wallis one-way analysis of variance test was applied to determine whether the mean error of a fraction was significantly associated with either patient index or fraction index.



#### 4.2.6. Measurement Precision

Tumor-surrogate models created from the training data were compared to models with simulated noise in either input (external marker) or output (tumor) measurements. In each case, models based on 6 training samples were evaluated on the testing dataset.

To simulate radiographic tumor localization uncertainties, noise from a Gaussian distribution was added to the radiographic tumor localizations. Noise levels were varied by randomly selecting the standard deviation of the Gaussian noise in each trial. Another set of models was then created from training data with noise and used to determine new predicted tumor positions in the testing dataset. This process was repeated for noise added to external marker localizations.

### 4.3. Results

#### 4.3.1. Model Design

For OLSxyz, PLSxyz, OLSr, PLSr, and SYNr models trained on 6 samples, 22.8%, 12.7%, 19.0%, 9.1%, and 9.5% of the predictions, respectively, exceeded 0.5 cm (Figure 4.2). The OLSxyz, PLSxyz, and OLSr distributions peaked in the 0.1 cm to 0.2 cm range, and the PLSxyz, PLSr, and SYNr distributions peaked in the 0-0.1 cm range. PLSr and SYNr results did not differ significantly for any quantity of training points.

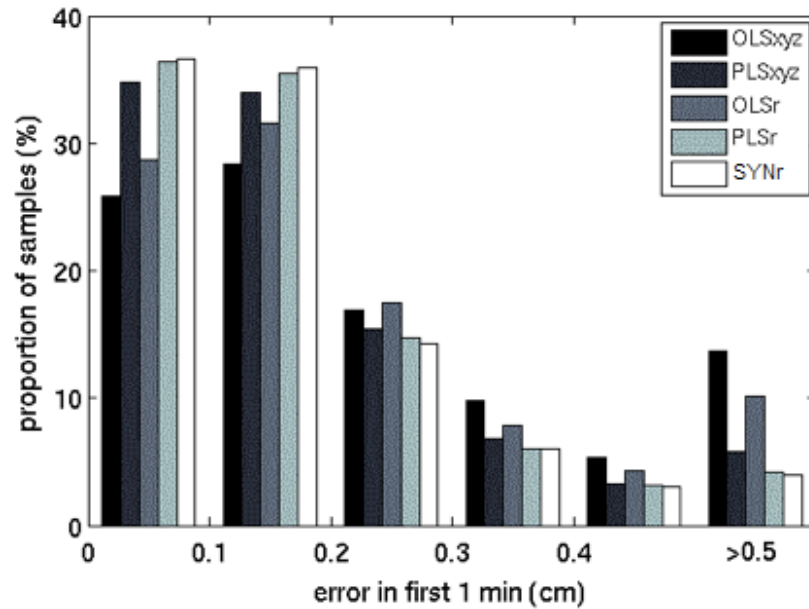


Figure 4.2 Histogram of tumor localization errors during the first minute of testing for models based on 6 training samples. The last bin comprises all errors greater than 0.5 cm.

### 4.3.2. Training Data Selection

#### 4.3.2.1. Quantity of Training Data

The 95<sup>th</sup> percentile and mean tumor position prediction errors for each number of training samples are shown in Figure 4.3. The OLSxyz error peaked to an average of 7.7 cm when  $N = 10$  samples were used to train the model. OLSxyz, and OLSr 95<sup>th</sup> percentile errors exceeded 1 cm for some values of  $N$ , but PLSxyz, PLSr, and SYNr 95<sup>th</sup> percentile errors did not exceed 1 cm in the tested range of  $N$ . Mean errors for the six models converged to approximately 0.2 cm for  $N > 20$ .

#### 4.3.2.1. Time Since Data Acquisition

Average errors for each model type increased as time elapsed after the end of the training data (Figure 4.4). Mean errors in 0-2 min and in 10-20 min of data increased from 0.3 to 1.3 cm for OLSxyz, 0.2 to 0.5 cm for PLSxyz, 0.2 to 0.6 cm for OLSr, 0.2 to 0.4 cm for PLSr, and 0.2 cm to 0.4 cm for SYNr.

#### 4.3.1. Tumor-Surrogate Correlation

The uncorrelated (Gaussian noise) input degraded prediction models (Figure 4.5). Mean errors in the 0-2 min bin increased by 57% for OLSr and by 16% for PLSr.

#### 4.3.2. Tumor Site

For each modeling algorithm, error distributions were comparable across the three tumor sites (Figure 4.6). Lung, liver, and pancreas mean errors were 2.2 mm, 1.9 mm, and 2.3 mm, respectively, and further details are described in Table 4.1. Of the three sites, only the pancreas errors differed significantly (Kruskal-Wallis one-way ANOVA,  $p < 0.05$ ) from errors of the other sites. However, it can be argued that the 0.1 mm mean error difference between lung and pancreas cases is not likely to be clinically significant. It is not clear whether liver results would differ significantly from lung results with a larger sample size.

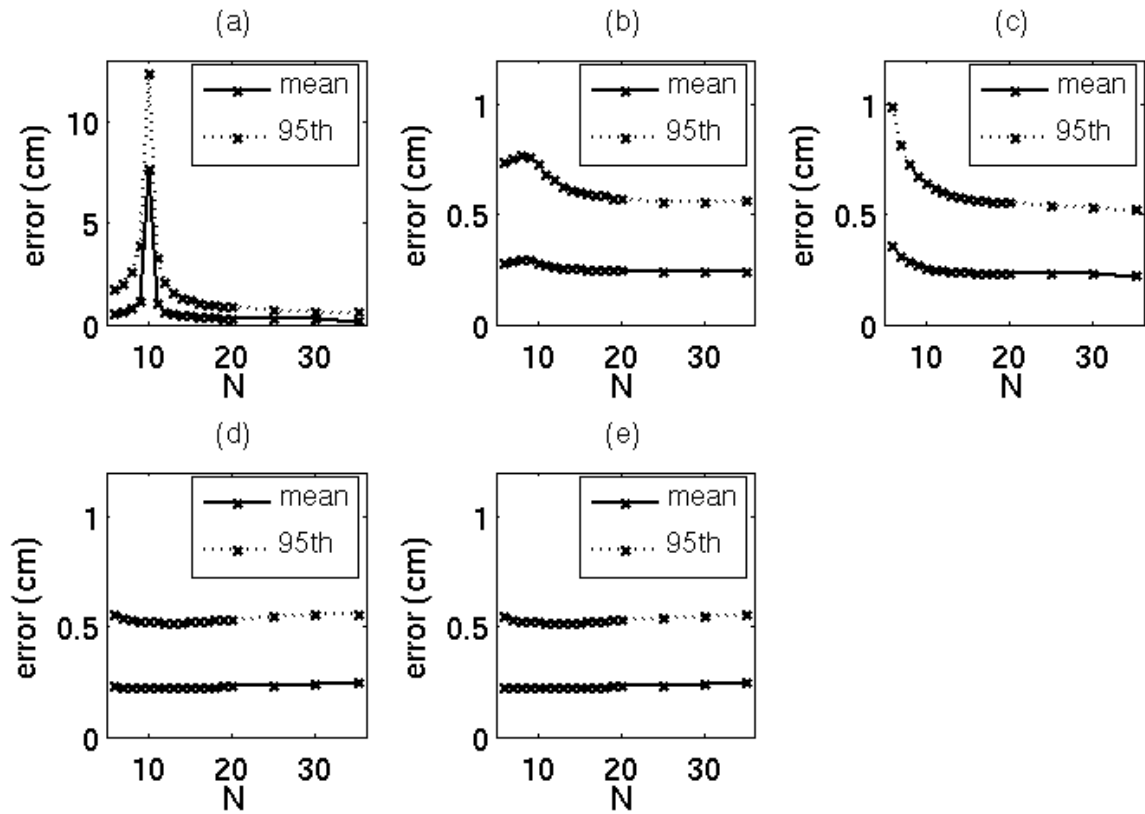


Figure 4.3 Mean and 95<sup>th</sup> percentile tumor position model prediction errors in the test data acquired over 20 minutes for (a) OLSxyz, (b) PLSxyz, (c) OLSr, (d) PLSr, and (e) SYNr models. For clarity, the y-axis in (a) is scaled differently than that of (b-e).

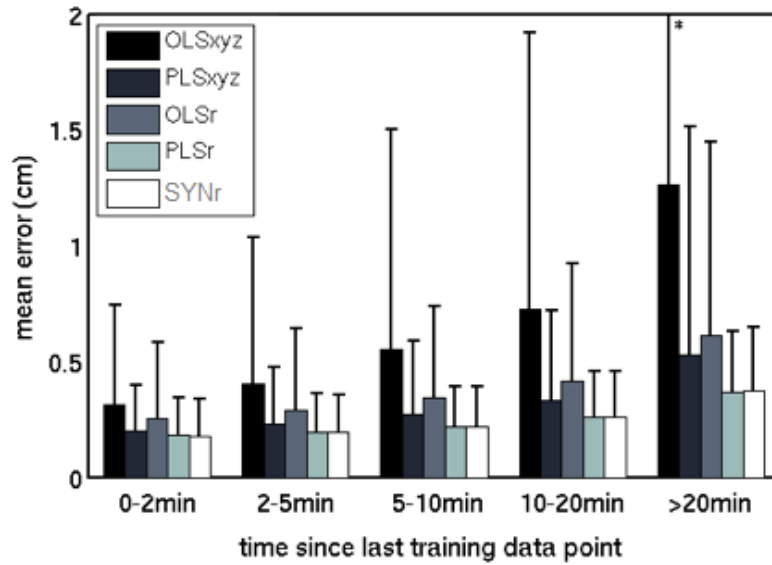


Figure 4.4 Mean and standard deviation (error bars) of tumor position model prediction errors, binned by time elapsed since the end of training data collection. \*The standard deviation of the OLSxyz error bar in the >20 min bin is 2.3 cm.

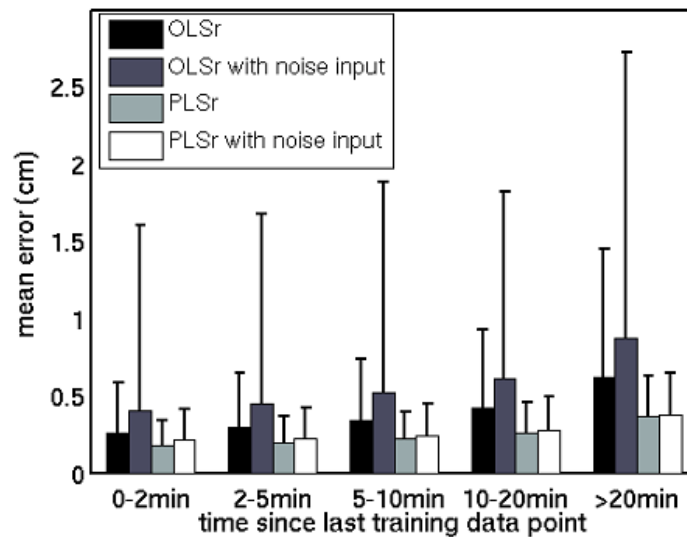


Figure 4.5 The impact of an uncorrelated (Gaussian noise) input variable in OLSr and PLSr models. Mean and standard deviation of model errors indicate that the additional input increased errors. In the 0-2 min bin, OLSr errors increased by 57%, and PLSr errors increased by 16%.

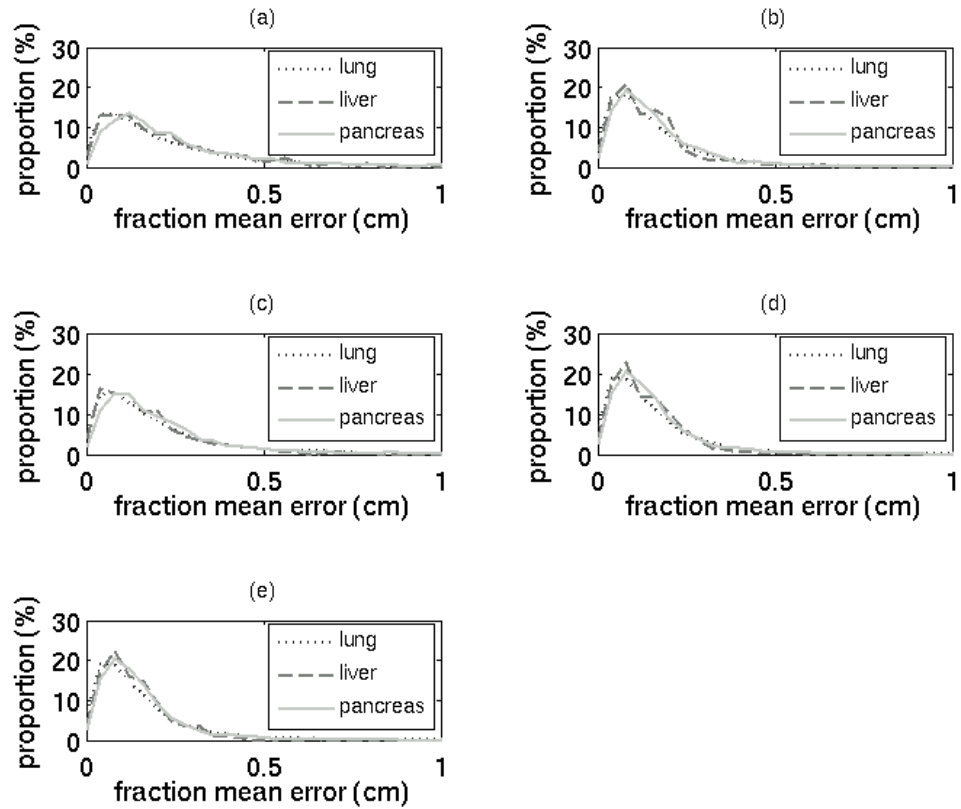


Figure 4.6 Histograms of mean error in each fraction by tumor site for (a) OLSxyz, (b) PLSxyz, (c) OLSr, (d) PLSr, and (e) SYNr models, each based on 6 training data points.

Table 4.1 Errors for models based on 6 training points, stratified by tumor site

Model	Mean $\pm$ standard deviation of error (mm)		
	Lung	Liver	Pancreas
OLSxyz	$3.0 \pm 4.5$	$2.7 \pm 2.7$	$3.3 \pm 4.6$
PLSxyz	$1.9 \pm 2.0$	$1.7 \pm 1.3$	$2.0 \pm 2.0$
OLSr	$2.5 \pm 3.4$	$2.1 \pm 2.6$	$2.6 \pm 2.8$
PLSr	$1.8 \pm 1.6$	$1.6 \pm 1.1$	$1.8 \pm 1.5$
Synchrony	$1.7 \pm 1.6$	$1.6 \pm 1.0$	$1.8 \pm 1.5$
Pooled results	$2.2 \pm 2.9$	$1.9 \pm 1.9$	$2.3 \pm 2.8$

#### 4.3.1. Inter-Patient and Inter-Fraction Variation

For each of the model types, the model error in a single fraction was significantly ( $p < 0.05$ ) associated with the patient from whom the fraction was recorded. This pattern is evident in Figure 4.7, in which the mean errors of the four fractions of patient 2, for instance, cluster around a value that differs from the value associated with patient 8. The mean model error over a fraction was not significantly ( $p > 0.05$ ) associated with the treatment fraction index.

#### 4.3.2. Measurement Precision

When noise was added to measurements of radiographic tumor positions in the training dataset (Figure 4.8), the resulting average error in the testing dataset varied as 1.1, 0.3, and 0.4 times the average noise for OLSr, PLSr, and SYNr, respectively; noise-to-error correlations ranged from 0.44 to 0.53. When noise was added to the measurement of the external surrogate position data, the resulting average error in the testing dataset varied as 3.7, 0.6, and 0.6 times the average noise for OLSr, PLSr, and SYNr, respectively, and noise-to-error correlations ranged from 0.09 to 0.32.

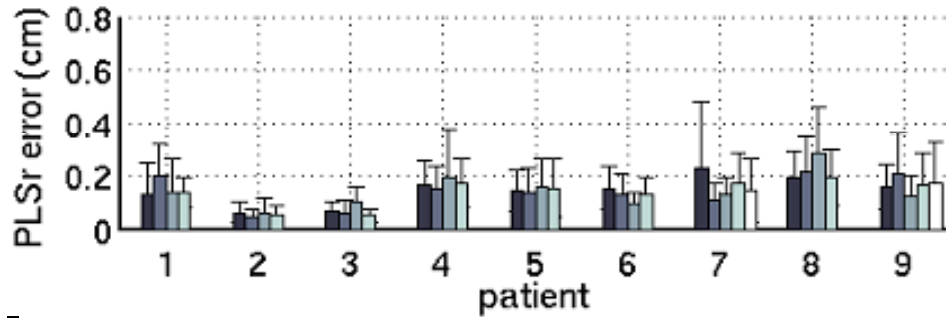


Figure 4.7 Mean and standard deviation of 9-training-datapoint PLSr in each fraction for 9 patients. Errors represent samples acquired within 20 minutes of the training dataset. For clarity, the figure is limited to the 9 patients with at least 4 treatment fractions available for analysis; the results for these patients are consistent with the dataset as a whole.

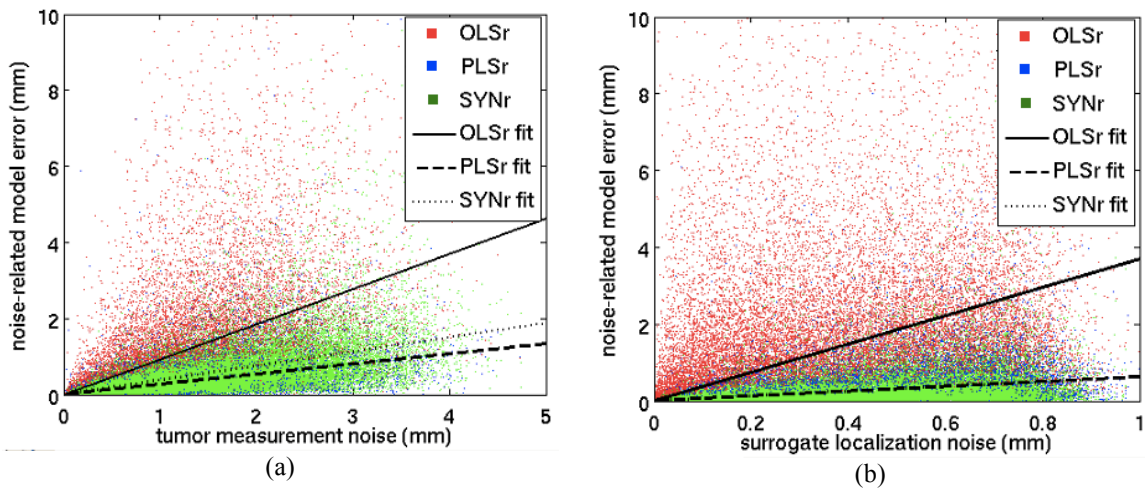


Figure 4.8 (a) Tumor and (b) external marker localization noise (in the training data used to build the model that predict tumor position) versus tumor position prediction error. Best fit lines represent least-squared-error linear regression fits with an assumption of zero error for zero noise. OLSr regression lines have slopes of (a) 1.1 and (b) 3.7. The PLSr line overlies the SYNr line in (b).



#### 4.4. Discussion

In this study, a series of factors impacting the accuracy of respiratory surrogate models of tumor motion were explored. Model accuracy was affected by inter-patient variations, tumor and external surrogate measurement precision, tumor-surrogate correlation, training data selection, tumor-surrogate correlation, and model design. Tumor site and fraction index were not predictive of model accuracy. These results provide the reader with a framework for designing and evaluating a surrogate-based tumor position prediction model. In addition, PLS models were more accurate than OLS models and were as accurate as Synchrony<sup>TM</sup> models.

Many studies reporting high tumor-surrogate correlations have evaluated only a few minutes of data.<sup>3,56</sup> The results of these studies may not be representative of the behavior of the model over entire treatment fractions. Analyses of datasets capturing motion over the duration of a treatment fraction have reported variations in the tumor-surrogate relationship.<sup>6,21,30</sup> In this study, model errors increased over time; we attribute this increasing error to tumor-surrogate relationship changes. In practice, this effect could be overcome by updating the model during the treatment fraction. Intra-fraction model updates have been utilized by tracking systems like Cyberknife Synchrony<sup>TM</sup>, but model updates are not common in gated treatment protocols.

In this work, projecting external marker motion onto a single dimension improved accuracy by increasing the correlation between surrogate signals and tumor motion. Shifting the surrogate signal in time relative to the tumor signal is a common method for increasing tumor-surrogate correlation.<sup>29-30,33,57</sup> However, because of changes in the

tumor-surrogate phase offset, these shifted surrogates are not likely to maintain their improved correlation over time.<sup>6,30</sup>

PLSr and SYNr results did not differ significantly. We investigated other model designs (not described in detail here) but were unable to reduce model errors below those of the PLSr model. Because the continuous external marker motion in the data log files appears to indicate a high signal-noise ratio (SNR), we hypothesize that the accuracy of any model based on this dataset is limited by precision of the gold-standard radiographic tumor localizations. PLSr and SYNr represent the state-of-the-art in indirect tumor localization algorithms. In addition to their accuracy, each requires only milliseconds to derive tumor position from surrogate data. Subject to the limitations of SNR and the other factors investigated in this study, both PLSr and SYNr are candidates for real-time applications.

Decreased measurement precision in either gold-standard tumor localizations or external surrogate measurements was found to have considerable impact on model accuracy. For OLSr models, the errors in tumor position prediction induced by measurement precision limitations were 1-4 times as large as the measurement errors themselves. For PLSr and Synchrony<sup>TM</sup> models, the errors in tumor position prediction were 0.3-0.6 times as large as the measurement errors. Many optical (surrogate) tracking systems are capable of achieving sub-millimeter accuracy,<sup>58-59</sup> but infrared tracking accuracies exceeding one millimeter have been reported in clinically available devices.<sup>60</sup> Typical errors of x-ray-based localizations of bony anatomy or fiducial tracking are 0.6-2 mm.<sup>60</sup>

Surprisingly, utilizing a larger quantity of training data, whether in dimensionality of marker motion or in number of training data points, did not improve the accuracy of tumor position predictions. In the case of OLS models, the error peaked at the transition between underdetermined and overdetermined systems. For any modeling algorithm, the optimal number of training points will also vary as a function of spacing between training samples. Training data captured over a period of minutes may encompass tumor-surrogate relationship changes that would not be present in training data captured in a shorter period of time.

PLS was consistently more accurate than OLS, a conclusion in agreement with the diaphragm tracking work of Qiu *et al.* OLS regression coefficients are volatile when inputs are collinear;<sup>37</sup> the regression coefficients in OLS models often vary considerably for different training samples from the same dataset.<sup>40</sup> As a result, PLS has been described a superior alternative to OLS when the inputs are highly collinear.<sup>61</sup>

Yan *et al.* has shown that multiple-surrogate models of tumor motion can be more accurate than single-marker models by overcoming the location effect, in which tumor-surrogate correlation varies with marker placement.<sup>33,36</sup> Nevertheless, our results support the conclusion that incorporating additional surrogate-based inputs that are uncorrelated with tumor motion may actually degrade the model. Fortunately, respiration-induced tumor motion is correlated with such respiratory surrogates as markers affixed to the torso, spirometry, and bellows systems.<sup>6,33,62</sup>

Finally, patient-specific, fraction-specific, and site-specific results were evaluated. Results did not differ between lung, liver, and pancreas cancers. Furthermore, the model

error was not found to be significantly associated with fraction index. Patient index, on the other hand, was significantly associated with model accuracy. The practical implication of these results is that the design of a study to evaluate tumor motion models should use a large enough group of patients to obtain statistically significant results; multi-site and inter-fraction data are less important unless a model will be applied without revision on multiple treatment days.

#### 4.5. Conclusions

The accuracy of tumor position prediction models using external surrogates was affected by inter-patient variations, measurement precision, tumor-surrogate correlation, training data selection, and model design, but tumor site and fraction index were not predictive of model accuracy. PLS regression models were more accurate OLS models and as accurate as Synchrony<sup>TM</sup> models.

## CHAPTER 5: Incidence of Changes in Respiration-Induced Tumor Motion and its Relationship with Respiratory Surrogates During Individual Treatment Fractions

### 5.1. Introduction

A major challenge of tumor motion management in radiation therapy is that respiration-induced tumor motion is not truly periodic. Both tumor motion and the relationship between tumor position and respiratory surrogate signals can change over time. However, to our knowledge, no study to date has quantified the incidence of tumor motion changes during individual fractions. This information would allow clinicians to better evaluate the need for complex, often time- and resource-consuming motion management techniques. Furthermore, Studies to date have not quantified the incidence of changes in the relationship between tumor motion and respiratory surrogate signals during individual treatment fractions. If it is found that the tumor-surrogate relationship should be evaluated more than once during a fraction, such a change could be implemented rapidly in clinical protocols

In this study, tumor motion and the relationship between tumor displacements and concurrent external marker displacements were evaluated in a retrospective analysis. The purpose of this study was to determine how frequently (1) tumor motion and (2) the spatial relationship between the tumor and respiratory surrogates change over the course

of a treatment fraction in lung and pancreas cancers. Tumor motion differences were evaluated through both displacements and their implications on treatment margins.

## 5.2. Methods

### 5.2.1. Data

A database of Cyberknife Synchrony™ system log files comprising 55 treatment fractions from 37 lung cancer patients and 29 treatment fractions from 16 pancreas cancer patients who underwent stereotactic body radiation therapy (SBRT) was analyzed. Lung tumor locations are described in Table 5.1. The log files included (1) the three-dimensional coordinates of the centroid of fiducials (typically, 3 fiducials) implanted in the tumor and intermittently measured via stereoscopic radiographs, and (2) three-dimensional coordinates of a set of three light-emitting diodes (LEDs) affixed to the patient's form-fitting vest. The frequent (26 Hz) measurements of LED (external) positions were matched to the intermittent (once every 3 beams – approximately once per minute) measurements of tumor positions using timestamps stored in the Cyberknife log files. The data included only the longest period of uninterrupted treatment in each fraction. Thus, any pre-treatment images, patient repositioning events, and unplanned radiographs were excluded from the analysis.

The treatment fraction datasets were divided into 10-min blocks (Figure 5.1). Because radiographic localizations were timed as once every third beam, the images were captured at irregular intervals that varied with the duration of individual treatment beams. Intervals between localizations sometimes exceed five minutes, leading to sparse 10-min

datasets. For this reason, only treatment fractions with at least 9 data points in each of the first three 10-min data blocks were selected for this study.

While it usually takes an hour or longer to deliver hypofractionated treatments using the Cyberknife system, most patients receive hypofractionated treatments on conventional linear accelerators, where treatment times are 30 min or less. Conventional treatment fractions may be shorter in duration. For this reason, this analysis was limited to 30 min of data (Figure 5.1).

### 5.2.1. Tumor Location Analysis

Results were stratified by tumor site (lung and pancreas) and, for lung tumors, by lobe. The lung lobe was known for 26 of 37 (Table 5.1) lung cancer patients.

Table 5.1 Lung tumor locations

Location	Number of patients	Number of fractions
Left upper lobe	7	12
Left lower lobe	6	6
Right upper lobe	4	5
Right middle lobe	3	4
Right lower lobe	6	8
Unknown	11	20

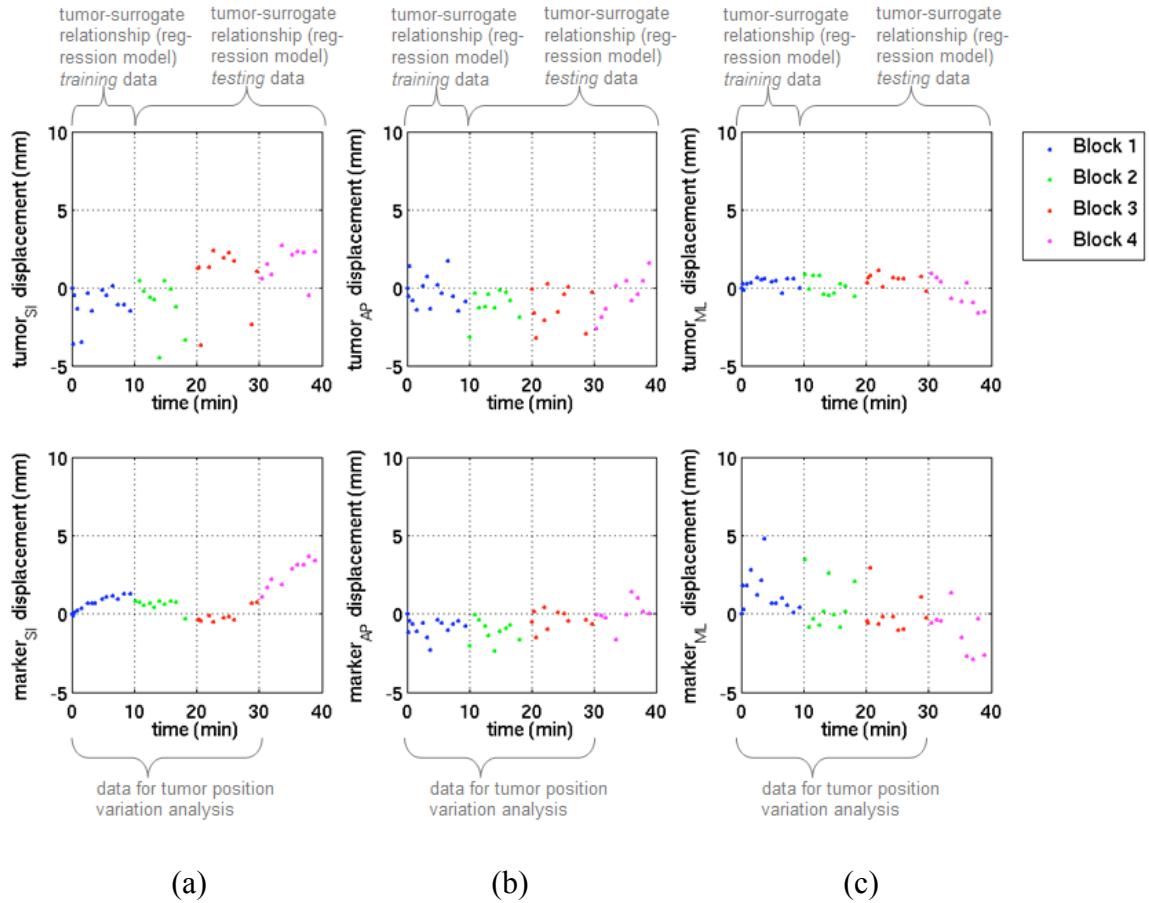


Figure 5.1 Tumor and surrogate marker (a) SI, (b) AP, (c) ML displacements for a single treatment fraction. For clarity, data from only one of the three surrogate markers is shown.

### 5.2.2. Tumor Position Variation

The means of tumor positions (determined directly from the Cyberknife Synchrony™ log files) within 10-min data blocks were evaluated and compared. Differences in mean position across 10-min periods are representative of changes in the baseline tumor position but are subject to under-sampling errors. For this reason, the 10-min data blocks were characterized and compared using the Wilcoxon Rank-Sum test and the Kruskal-



Wallis one-way ANOVA test.<sup>63</sup> These tests are capable of discerning whether detected differences are statistically significant for the available sample size. They calculate the probability that data captured during different 10-min data blocks are representative of the same continuous distribution of tumor positions and can detect changes in both the median tumor position and the tumor position probability density function (PDF). The Wilcoxon Rank-Sum test was used to determine whether the distribution of tumor positions changed significantly from one 10-min period to the next, and the Kruskal-Wallis one-way ANOVA test was used to determine whether the distribution of tumor positions differed during at least one 10-min block in first 30 min of the treatment fraction.

Tumor position variations were further characterized by calculating appropriate treatment margins (1) from the first 10 min of data in the fraction and (2) from the first 30 min of data in the fraction. Anisotropic margins were calculated according to a previously validated margin formulation.<sup>64</sup> Margins were estimated as:  $M = 2.5\Sigma + 0.84\sqrt{\sigma^2 + 0.4096} - 0.5376$ , where  $\sigma$  is the standard deviation of tumor positions about zero and  $\Sigma$  is the standard deviation of tumor positions about the mean tumor displacement. This margin formulation assumes penumbra width of 6.4 mm, 95% isodose coverage and a 90% probability level.

### 5.2.3. Baseline Shift Detection

To determine whether tumor baseline position shifts can be predicted from surrogate marker position baseline shifts, the tumor and surrogate marker displacements from their

positions at the start of the treatment fraction were determined as

$$d_{tumor,i} = \sqrt{\sum_{j=1}^3 (t_{j,i} - t_{j,1})^2} \text{ for 3D tumor positions } (t_{1,i}, t_{2,i}, t_{3,i}) \text{ at sample } i \text{ and}$$

$$d_{marker,k,i} = \sqrt{\sum_{j=1}^3 (m_{k,j,i} - m_{k,j,1})^2} \text{ for surrogate marker positions } (m_{k,1,i}, m_{k,2,i}, m_{k,3,i}) \text{ at}$$

sample  $i$ , where  $k$  indicates the marker index. The correlation between  $d_{tumor}$  and  $d_{marker}$  was determined for each marker and treatment fraction.

#### 5.2.4. Internal-External Relationship Variation

To characterize the relationship between the external surrogate marker and tumor displacements, partial-least-squares (PLS) regression was applied to the data in the first 10 min (the training dataset) of each treatment fraction. PLS is a statistical modeling approach that allows for prediction of tumor positions (output variables) from concurrent surrogate marker positions (input variables). The PLS regression model was of the form  $\hat{Y} = X \cdot B$ , where the model-based estimate of the tumor position,  $\hat{Y}$ , is given by the product of the matrix of surrogate marker positions  $X$  and the matrix of PLS regression coefficients  $B$ . See Section 2.6.2 for details regarding the calculation of  $B$  through PLS regression.

Degradation in the accuracy of the models over time, as indicated by increasing PLS tumor displacement prediction error, would indicate a changing relationship between the tumor positions and the surrogate marker positions. Therefore, the PLS model was then applied to the surrogate marker positions that were localized *after* the first 10 minutes of the fraction to estimate the concurrent tumor positions. The estimated

positions determined by the model were then compared to the tumor positions in the log files to determine the errors between the predicted and actual tumor positions. Time trends in error for each fraction were evaluated.

Reported tumor position error values represent the 3D vector displacement between the actual tumor position and the modeled tumor position. The errors were analyzed in two ways. First, for each fraction, the mean error of each 10-min block of data was calculated. Errors were then compared across 10-min data blocks. Second, each treatment fraction was evaluated individually to determine the incidence of increasing error in the population. To determine whether the error increased significantly, a line was fit to the time versus error data in each fraction using ordinary-least-squares regression. The hypotheses that the slope of each line was non-zero and either positive or negative were tested (F-test,  $p < 0.05$ ) to detect significant time trends.

### 5.3. Results

#### 5.3.1. Tumor Positions

The maximum vector displacements between mean tumor positions in consecutive (either first to second or second to third) data blocks were 7.1 mm for lung and 6.0 mm for pancreas. In each direction and tumor site, the difference in mean tumor position between the first and third 10-min blocks was larger than the differences in first to second and second to third data blocks (Figure 5.2), indicating a trend of increasing divergence of the baseline position over time. For lung and pancreas, respectively, the mean tumor position changed by  $>5$  mm in 2% and 1% of cases comparing consecutive 10-min blocks of data

and in 13% and 7% of cases comparing first and third 10-min blocks of data. SI and ML differences in mean positions between consecutive 10-min blocks were significantly (one-way ANOVA,  $p < 0.05$ ) associated with the lobe of the lung (Figure 5.3).

In consecutive 10-min data blocks, the differences between tumor position distributions were significant (Wilcoxon Rank-Sum,  $p < 0.05$ ) in 23%, 23%, and 41% of lung cases and in 20%, 13%, and 33% of pancreas cases for SI, AP, and ML motion, respectively. In the first three 10-min blocks there was a statistically significant (Kruskal-Wallis,  $p < 0.05$ ) change in tumor position distributions in 76%, 80%, and 90% of lung fractions and in 71%, 60%, and 75% of pancreas fractions for SI, AP, and ML motion, respectively. Incidence of tumor position distribution changes was not significantly associated with lung tumor location.

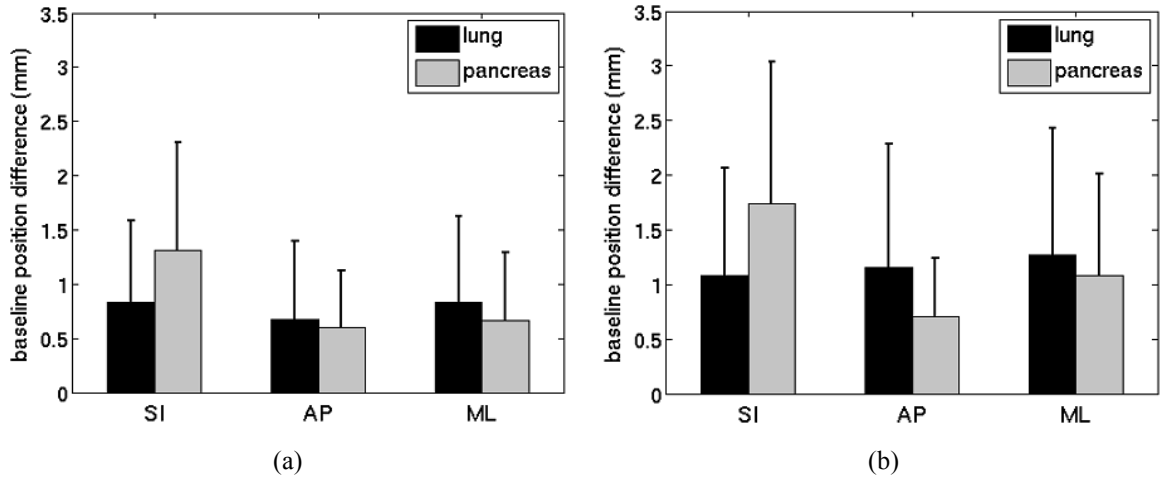


Figure 5.2 Mean and standard deviation (error bars) of absolute differences in mean position of tumor (a) in subsequent (combined data from first to second and second to third) 10-min blocks of data and (b) from the first to third 10-min blocks of data.

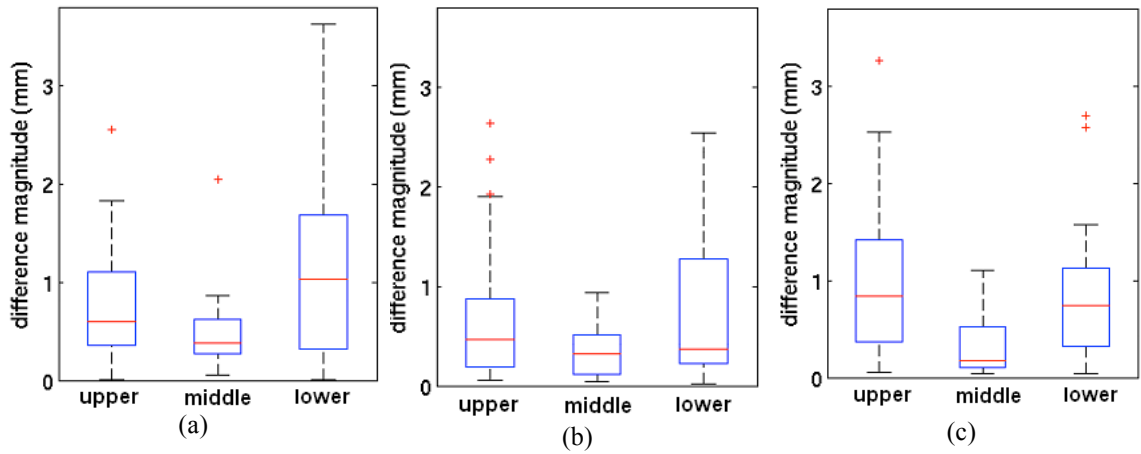


Figure 5.3 Boxplots of changes in mean tumor displacement differences between consecutive (first-to-second and second-to-third) 10-min blocks of data for upper, middle, and lower lung lobes in the (a) SI, (b) AP, and (c) ML directions.

### 5.3.2. Treatment Margins

In 61% and 54% of lung and pancreas fractions, respectively, margins in any of the three orthogonal directions that were calculated from 30 min of data were larger than margins calculated from 10 min of data (Figure 5.4). The absolute difference between margins derived from 10 min of SI data and margins derived from 30 min of SI data was  $>1$  mm in 42% of lung and in 45% of pancreas cases. AP and ML results are given in Table 5.2.

Treatment margins for lower lobe lung tumors were significantly (t-test,  $p < 0.05$ ) larger than those of both upper and middle lobe lung tumors. The difference between 10-min and 30-min SI margins for lower lobe tumors differed significantly (t-test,  $p < 0.05$ ) from those of upper (but not middle) lobe tumors (Figure 5.5). Differences between 10-min and 30-min AP and ML margins were not significant (t-test,  $p > 0.05$ ) for any lung tumor location.

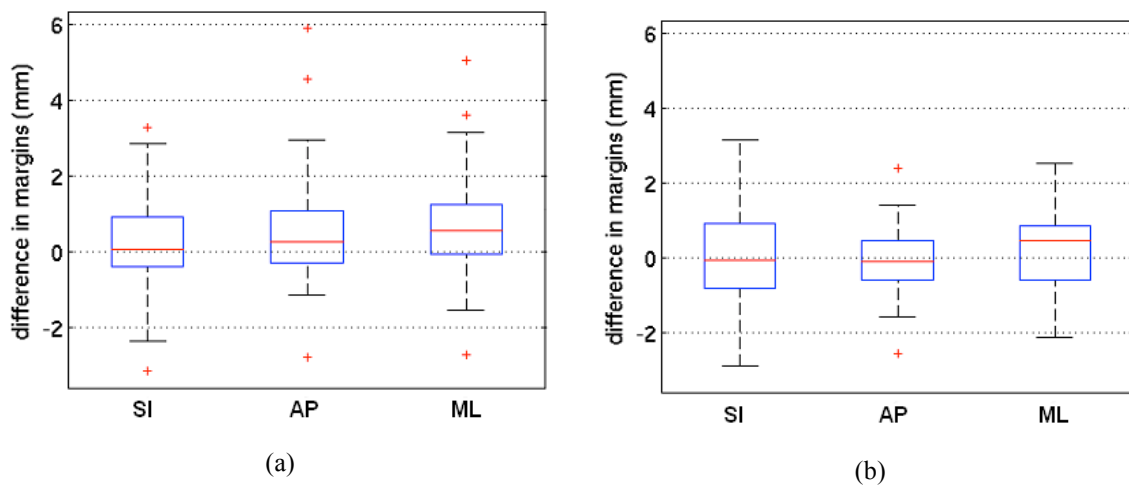


Figure 5.4 Boxplots of differences between treatment margins calculated from the first 10 min and from the first 30 min of SI data for (a) lung and (b) pancreas fractions. Positive values indicate that the 30-min margin was larger than the 10-min margin.

Table 5.2 Incidence of large differences between 10 min- and 30 min-based treatment margins

	Lung			Pancreas		
	SI	AP	ML	SI	AP	ML
Difference > 1 mm	42%	35%	36%	45%	31%	31%
Difference > 2 mm	18%	11%	16%	21%	10%	17%
Difference > 3 mm	4%	4%	5%	3%	3%	0%

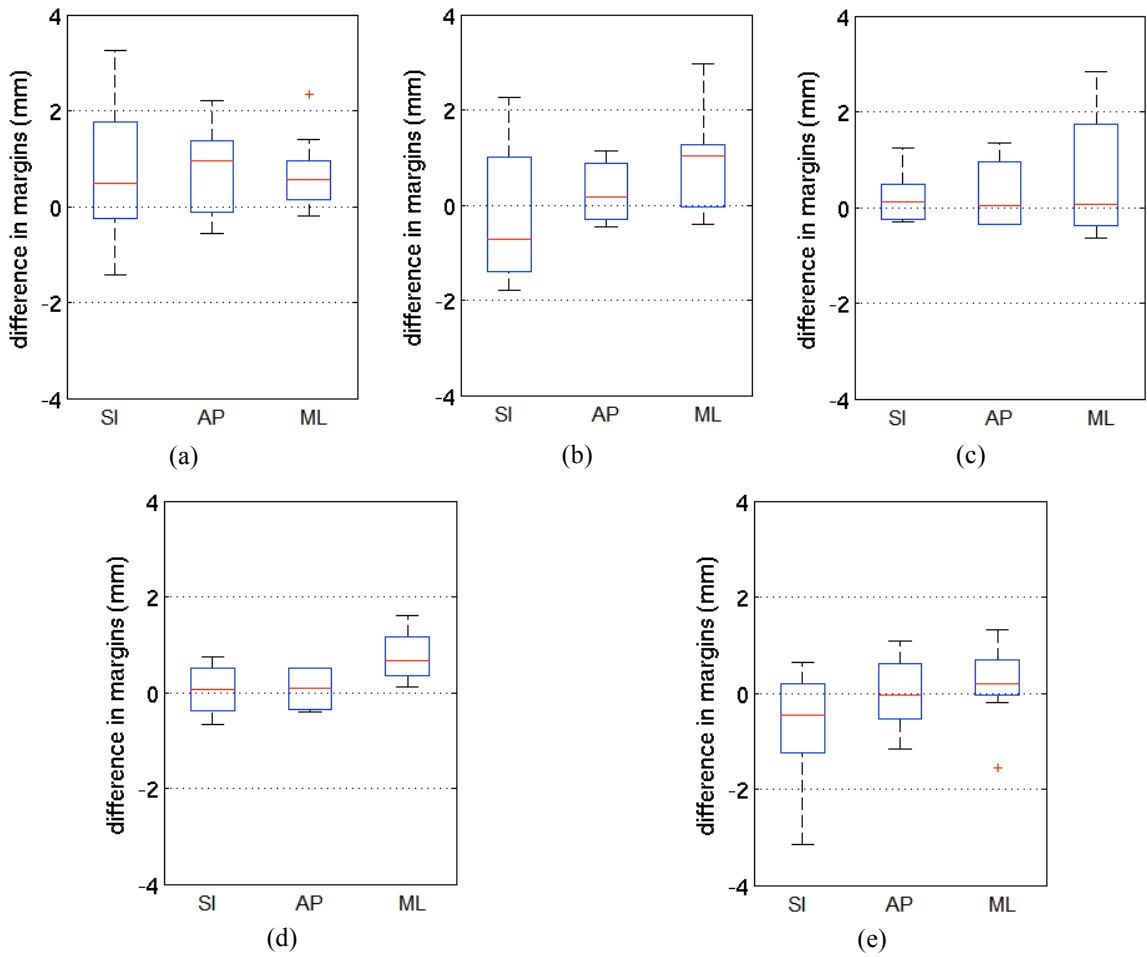


Figure 5.5 Boxplots of differences between treatment margins calculated from the first 10 min and from the first 30 min of SI data for (a) LUL, (b) LLL, (c) RUL, (d) RML, and (e) RLL lung fractions. Positive values indicate that the 30-min margin was larger than the 10-min margin.

### 5.3.3. Baseline Shift Detection

The mean ( $\pm$  standard deviation) of correlations between the displacement of the tumor from its initial position,  $d_{tumor}$ , and the displacement of a marker from its initial position,  $d_{marker}$ , was  $0.70 \pm 0.21$  (Figure 5.6). Eighty-three percent of correlations were  $>0.5$ , indicating a strong correlation. However, when data from all fractions are pooled (Figure 5.7), it is apparent that  $d_{marker}$ , though well correlated with  $d_{tumor}$ , is not predictive ( $R^2 = 0.43$  for linear fit) of  $d_{tumor}$ . Estimating  $d_{tumor}$  from  $d_{marker}$  using a linear least-squares fit can lead to errors exceeding 10 mm (Figure 5.7b).

### 5.3.4. Internal-External Relationships

Regression analysis was used to characterize the relationship between surrogate marker positions and tumor positions. An example of a change in the relationship between motion of a surrogate marker and motion of the tumor is given in Figure 5.8.

When tumor position prediction errors (3D vector displacement between the actual tumor position and the modeled tumor position) were binned by data block and the population considered as a whole, the PLS tumor position model errors increased monotonically for subsequent blocks of data (Figure 5.9). The baseline errors (mean radial error for the model-training data) were 1.1 mm for lung and 1.2 mm for pancreas. The mean radial tumor position prediction errors in the 2nd, 3rd, and 4th 10-min data blocks, respectively, were 2.1 mm, 2.9 mm, and 3.6 mm for lung cases and 2.0 mm, 2.8 mm, and 3.6 mm for pancreas cases.



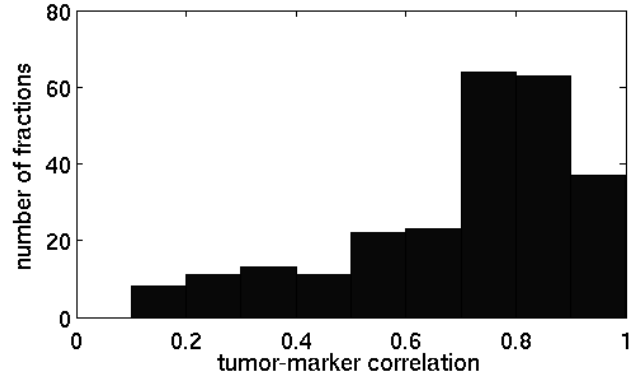
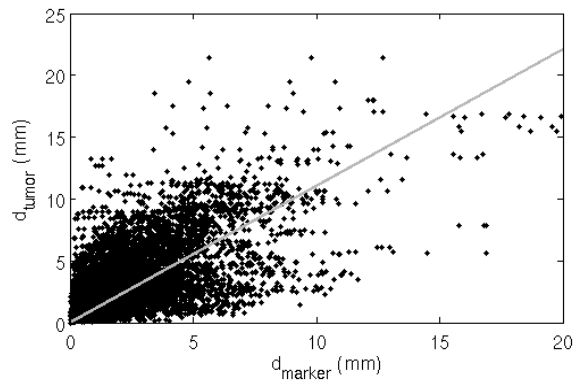
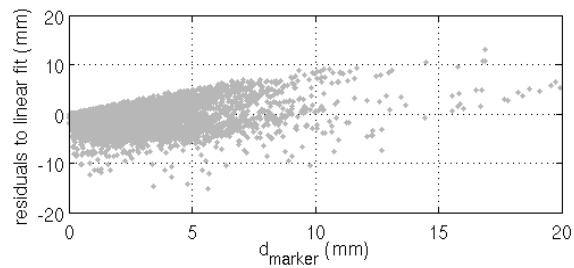


Figure 5.6 Histogram of correlation between dtumor and dmarker for each marker and treatment fraction.



(a)



(b)

Figure 5.7 (a) Displacement from initial position for tumor (dtumor) versus displacement from initial position for surrogate markers (dmarker) with a linear least-squares best fit line ( $R^2 = 0.43$ ). (b) Residuals for linear fit line indicating the errors in predicting dtumor from the best fit line in (a).

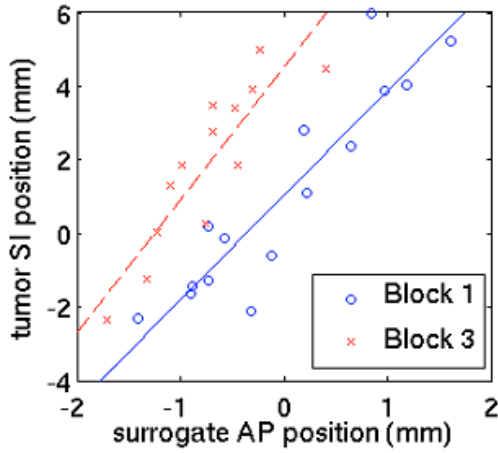


Figure 5.8 Example of a change in the relationship between AP motion of a surrogate marker and SI motion of a tumor from 1st 10-min block (circles) to the 3rd 10-min block (x's). The ratios of tumor motion to surrogate marker motion are indicated by the slopes of the least-squares fit lines: 2.8 mm tumor displacement per mm surrogate displacement and 3.6 mm tumor displacement per mm surrogate displacement.

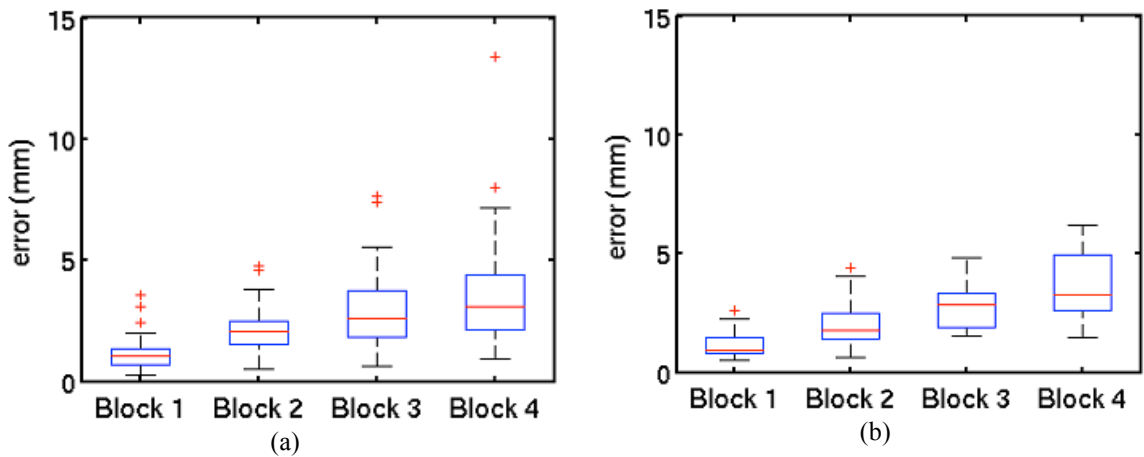


Figure 5.9 Boxplots of PLS model error (mean error in each fraction) in each of the first four 10-min blocks of data for (a) lung and (b) pancreas cases. Models were trained on the data in Block 1. Errors in each population increased monotonically for subsequent blocks of data.

For 10 min and 30 min of data, respectively, there was significant evidence of model degradation in 22% and 67% of lung fractions and 24% and 55% of pancreas fractions (Figure 5.10). The slopes of the trend lines describing tumor position prediction error versus time in each fraction were not significantly (t-test,  $p>0.05$ ) different for the 10-min and 30-min datasets; the mean  $\pm$  standard deviation rates of change were  $1.2 \pm 2.0$  mm per 10 min when measured over the first 10 min of data and  $1.1 \pm 2.1$  mm per 10 min when measured over 30 min data. For the 63% of lung and pancreas fractions showing significant model degradation over 30 min, the mean ( $\pm$  standard deviation) rate of error increase was  $1.6 \pm 2.5$  mm per 10 min.

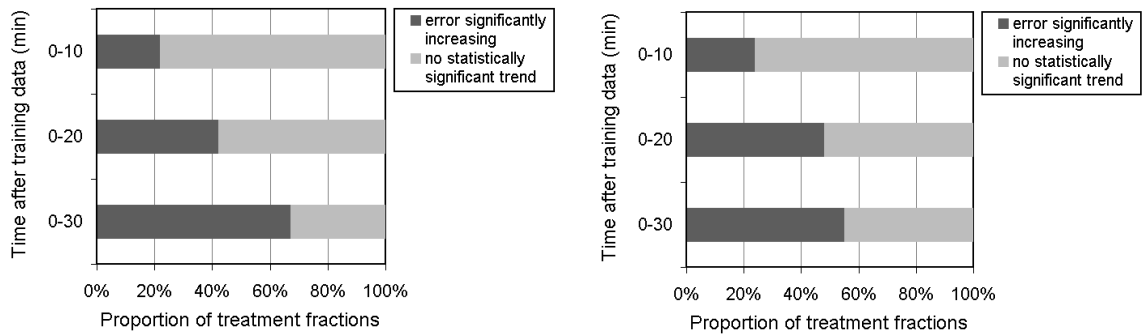


Figure 5.10 Proportion of (a) lung and (b) pancreas treatment fractions associated with a positive trend or no trend in model error over time when the first 10, 20, or 30 min of testing data is considered. There were no cases in which error decreased significantly over the course of the treatment fraction.

#### 5.4. Discussion

The results of this study clarify the scope and significance of the problem of respiration-induced tumor motion during radiation therapy. Cases in which the patient is on the couch for 30 min (in-room rather than beam-on time) were considered. During these 30-min fractions, baseline tumor position shifts greater than 5 mm are unlikely (13% for lung and 7% for pancreas). However, changes in tumor motion patterns over the course of a fraction are common, as tumor position distributions changed in about 75% of datasets. Finally, there was significant evidence of changes in the spatial relationship between tumor positions and surrogate marker positions in 60% of fractions analyzed.

The AAPM Task Group Report 76 recommends applying motion management techniques to tumors that move more than 5 mm.<sup>5</sup> In the absence of motion management, geometric misses are an inevitable consequence of respiration-induced tumor motion. While the motion can degrade the performance of any type of external beam radiation therapy,<sup>5</sup> it has even greater impact on advanced techniques like SBRT and IMRT, given the generally smaller sizes of tumors and the more precise nature of the treatments.<sup>9</sup> For these more *precise* techniques to benefit the patient, it is vital that targeting become correspondingly more *accurate*.

There has been debate on the importance of compensating for intra-fraction variations. Engelsman *et al.* reported that lung tumor set-up errors are generally larger than intra-fraction position variations, and that efforts should be focused on reducing setup error.<sup>65</sup> Conversely, Berbeco reported that the beam-to-beam variations of residual motion of the tumor during gating are greater than fraction-to-fraction variation.<sup>21</sup> In this

study, we conclude that the tumor motion is likely (>50% of cases) to change during a treatment fraction (~30 min).

The results of this study indicate that baseline tumor position and the pattern of tumor motion tend to diverge over time, with more than 6 times as many fractions seeing a shift of greater than 5 mm over 30 min as compared to 10 min. Such changes translate into difficulties in assessing tumor motion for the purposes of choosing an appropriate internal margin. The difference in margins based on 30 min of data as compared to margins based on 10 min of data was at least 1 mm in 42% and 45% of lung and pancreas cases, respectively. These results underscore the importance of either (1) completing treatment as quickly as possible or (2) monitoring real-time tumor motion throughout the duration of the treatment fraction. Of note, however, the rare large shifts between consecutive 10-min blocks of data sometimes exceeded 0.5 cm, a magnitude of potential clinical significance for those few patients. This tissue position divergence phenomenon was also observed by Hoogeman *et al.* In that study, changes of the order of magnitude seen in this study were observed in the spine of prone SBRT patients, which can be shifted by respiration.<sup>66</sup> Of interest, smaller drifts in the bony anatomy (spine of supine extra-cranial and skull of intra-cranial radiosurgery cases) that were not expected to be affected by respiration were also seen. Thus, it is reasonable to conclude that baseline lung and pancreas tumor position shifts may be caused, at least in part, by phenomena other than respiration, such as tissue settling and muscle relaxation.

Tumor motion could be more easily managed if tumor position could be predicted reliably from external surrogates. In this study, we utilized PLS to characterize the tumor-

surrogate relationship. While any form of regression analysis can be used to characterize the relationship between input and output variables,<sup>40</sup> our previous work has shown that models based on PLS tend to maintain their fidelity over a longer period of time than the more conventional ordinary-least-squares (OLS) models (Chapter 4). Thus, PLS is an ideal technique for determining whether the tumor-surrogate relationship truly changes.

By using a regression model to characterize the tumor-surrogate relationship, we were able to show that the relationship changes over time, a conclusion in agreement with Seppenwoolde *et al.*'s analysis of the Cyberknife Synchrony<sup>TM</sup> modeling algorithm output.<sup>18</sup> Previous studies have characterized some of these tumor-surrogate relationship changes as a time-varying phase difference between the tumor and the surrogate marker and have identified some of their causes, including destabilizing events like coughs, deep breaths, and breath-holds.<sup>6,30,36</sup> However, our study is the first to quantify the incidence of such changes in the patient population. Our results indicate that in most cases the tumor-surrogate relationship changes over a 30-min treatment fraction. Furthermore, while baseline tumor position shifts were associated with baseline position shifts in the surrogate markers, the magnitude of the tumor baseline position shift was not directly related to the magnitude of the surrogate marker baseline position shifts.

When a surrogate of respiration is used to infer tumor motion during treatment, it is important that new images be acquired during the fraction to confirm the model and correct for potential changes. The Cyberknife Synchrony<sup>TM</sup> system, for instance, intermittently localizes the tumor through radiographs at an average rate of once per minute. However, Seppenwoolde *et al.* suggests that capturing new training data once,

halfway through the treatment fraction, may be sufficient.<sup>18</sup> The optimal frequency of gold-standard tumor localizations will vary by patient but can be optimized for a patient population. The frequency for a clinical protocol will vary with the form of the tumor-surrogate model, the type of respiratory surrogate, and the desired tumor localization accuracy.

Results for lung and pancreas cases were similar. However, baseline position changes and tumor-surrogate relationship degradation were greater in the pancreas than in the lung. Similarly, lower lobe tumors, which generally have larger respiration-induced motion than other lung tumors,<sup>47</sup> were associated with larger treatment margins and changes in treatment margins for 10- and 30-min datasets.

The data in this study corresponded to free-breathing condition. It is unclear whether the results of this study may have changed if respiratory coaching was used to make breathing patterns more consistent. Nevertheless, Nehmeh *et al.* has shown that respiratory variations can be significant even with coaching.<sup>43</sup>

## 5.5. Conclusions

Both the tumor motion and the relationship between tumor and surrogate marker displacements change over most 30 min treatment fractions. Such changes must be taken into account for optimal motion management.

## CHAPTER 6: Inferring Positions of Tumor and Nodes in Stage III Lung Cancer from Multiple Surrogates Using 4D CT

### 6.1. Introduction

4D CT has emerged as a widely used tool for respiration-induced tumor motion assessment.<sup>67-69</sup> Recently, a number of groups have recommended the use of 4D CT to assess patient-specific nodal volume motion in Stage III lung cancer.<sup>70-74</sup>

Typical 4D CT image datasets include 10 volumetric images of the patient anatomy, each of which is associated with a different stage of respiration. To utilize the information in 4D CT images, it is necessary to identify relevant structures (primary tumor, nodal volumes, nearby organs) in each volumetric image. Current limitations of image analysis tools necessitate manual contouring for identifying these structures. To manually contour structures, a clinician traces the edge of the structure in each individual slice of the multi-slice volumetric image. For radiation targets such as the primary tumor and the nodal volumes, this process must be repeated for each respiratory phase image set.

The time-consuming nature of manually contouring relevant structures each of the volumetric datasets in a 4D CT image precludes its routine use in many clinics. In this study, we propose a new approach (Figure 6.1) for decreasing the contouring burden of 4D treatment planning for Stage III lung cancer, whereby (1) the target volumes



(including the primary tumor and nodes) in a *subset* of respiratory phase bin images are localized, (2) a group of anatomical respiratory surrogates in *all* image sets corresponding to respiratory phase bins are localized, (3) a mathematical model relating target position to anatomical surrogate positions is created, and (4) target positions in the *uncontoured* images are determined using the model.

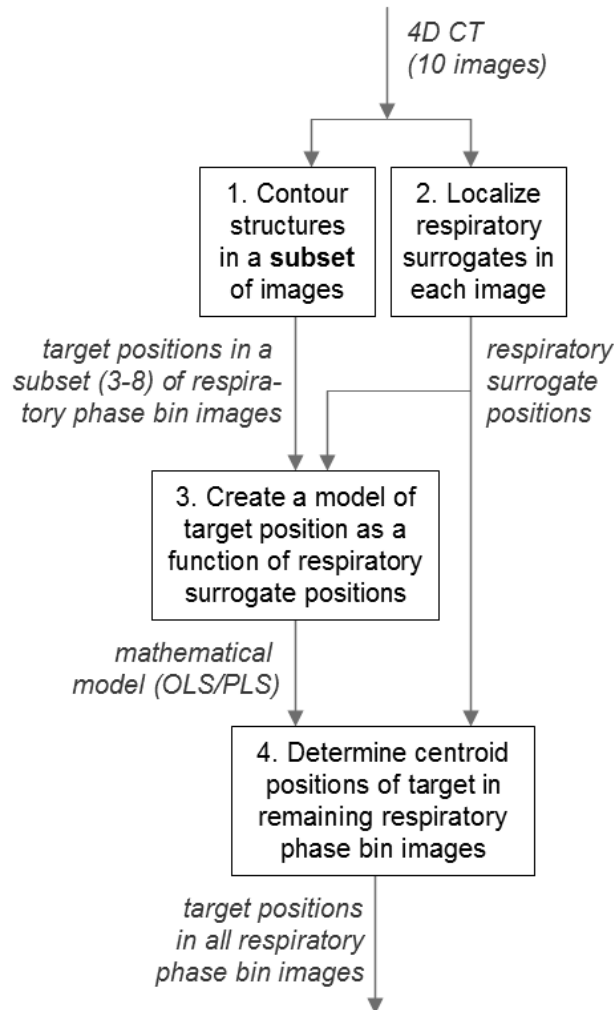


Figure 6.1 Summary of methodology employed for inferring the positions of the primary tumor and nodal volumes.

The purpose of this study was *to evaluate respiratory surrogate-based tumor motion modeling as a means of improving the workflow associated with contouring radiation targets in 4D CT scans*. We first characterized the relationship between radiation targets (primary tumors and nodal volumes) and a series of anatomical surrogates visible in 4D CT images: carina, xyphoid, nipples, and mid-sternum. We then applied two mathematical modeling techniques, Ordinary-Least-Squares (OLS) and Partial-Least-Squares (PLS), for inferring tumor and nodal volume positions from the surrogates. To examine the limits of this method, we tested models based on as few as 3 contoured respiratory phases, and we compared models based on all available surrogates to models based on carina position alone.

## 6.2. Methods

### 6.2.1. 4D CT Position Data

The VU University Medical Center database of planning scans was evaluated retrospectively to identify patient scan with both clearly demarcated mediastinal lymph nodes and the absence of 4D imaging artifacts. Patients were scanned in the supine position on a 16-slice CT scanner (LightSpeed 16; GE Healthcare; Waukesha, WI) with no intravenous contrast. Scans were performed in cine acquisition mode at 2.0 cm intervals, and images had a slice thickness of 2.5 mm. Patients were instructed to breathe normally with a regular rhythm. The respiratory signal was detected using the Real-time Position Monitoring (RPM) system (Varian Medical Systems, Palo Alto, CA). Images were obtained only after a quiet, regular breathing pattern was observed. All images and

corresponding respiratory signal files were binned into 10 separate respiratory phases of equal time intervals. The phases were labeled from 0% to 90%, with end-inspiration corresponding to the 0% bin.

A single radiation oncologist manually contoured the primary tumors and the nodal volumes and localized the anatomical respiratory surrogates, and a second radiation oncologist verified the contours. We included both benign and malignant nodes, regardless of size, and classified them according to the 1997 Mountain and Dresler system (Table 5.1).<sup>75</sup>

The anatomical surrogates were xyphoid (n=16), carina (n=16), left (n=7) and right (n=11) nipples (tracked in male patients only), and mid-sternum (n=15). We localized the mid-sternum by identifying a metal marker placed at the time of 4D CT, and we localized the carina by identifying the peak between main-stem bronchi on coronal image slices, which had been automatically interpolated by the treatment software.

Depending on their visibility in the 4D CT scan, 3-5 anatomical surrogates were tracked for each patient. In total, 3D position data from 16 primary tumors, 53 nodal volumes, and 65 anatomical surrogates from the 16 patients were analyzed. Subsequently, the centroid of the contoured volumes was used to describe their displacements.

### 6.2.2. Nodal Volume- and Tumor-Surrogate Correlation

We measured the correlations between positions of each primary tumor/nodal volume and positions of each anatomical surrogate in three orthogonal directions: medial-lateral (ML), anterior-posterior (AP), and superior-inferior (SI).

### 6.2.3. Modeling Tumor and Nodal Volume Position with Anatomical Surrogates

#### 6.2.3.1. Modeling Methods

We used two methods, ordinary least squares (OLS) and partial least squares (PLS) regression, to model the position of the primary tumor or a node as a function of anatomical surrogate positions. Both OLS and PLS operate according to  $\hat{Y} = X \cdot B$ , where  $X$  is an  $m \times n$  matrix of anatomical surrogate coordinates with  $m$  measurements (phases) and  $n$  variables (position coordinates),  $B$  is an  $n \times 3$  matrix of regression coefficients, and  $\hat{Y}$  is a matrix of  $m \times 3$  target position coordinates. See Sections 2.6.1 and 2.6.2 for details regarding how  $B$  was calculated through OLS and PLS regression, respectively.

#### 6.2.3.2. Impact of the Quantity of Contoured Respiratory Phase Images

We attempted to infer primary tumor and node positions from anatomical surrogates using image datasets corresponding to 3-8 randomly chosen respiratory phases. In creating each model, we randomly partitioned the image datasets into *training* and *testing* subsets, where the *training* subset contained 3-8 datasets. We used the *training* subset to create the model and then assessed the accuracy of the results (in the form of target inferred position errors) by applying the model to the *testing* subset. To cross-validate our analysis, we randomly partitioned the dataset 50 times and repeated the analysis for each primary tumor and nodal volume coordinate. Figure 6.1 (above) summarizes the methodology employed in this work.

#### 6.2.3.3. Three-Phase Model Analyses

We next determined the set of three phase bins that, when used to create models, resulted in the lowest overall mean error. To choose this set of phases, we tested models based on each of the 120 combinations of three respiratory phase bins ([0%, 10%, 20%], [0%, 10%, 30%], etc.) for each target, determining separate *3-phase* sets for OLS and PLS. Finally, we used the 3-phase sets to create and analyze OLS and PLS models from (1) all available anatomical surrogates and (2) the carina alone.

#### 6.2.3.4. Impact of Target Position

To determine whether the 3-phase model error varies with target position, we separated the 53 nodes into (1) upper mediastinal zone (stations 2 and 3), (2) mid-mediastinal zone (stations 4, 5, and 6), and (3) lower mediastinal zone (stations 7 and 8). We did not subdivide the primary tumors by location, because we had insufficient data (N=16).

### 6.3. Results

#### 6.3.1. Tumor-Surrogate Correlation

The mean ( $\pm$  standard deviation) correlations between target position and anatomical surrogate position for nodal volumes and primary tumors were  $0.41 \pm 0.26$  and  $0.42 \pm 0.26$ , respectively. Correlations between target coordinates and anatomical surrogate SI, AP, and ML coordinates (Figure 6.2) were  $0.47 \pm 0.27$ ,  $0.42 \pm 0.25$ , and  $0.34 \pm 0.24$ , respectively.

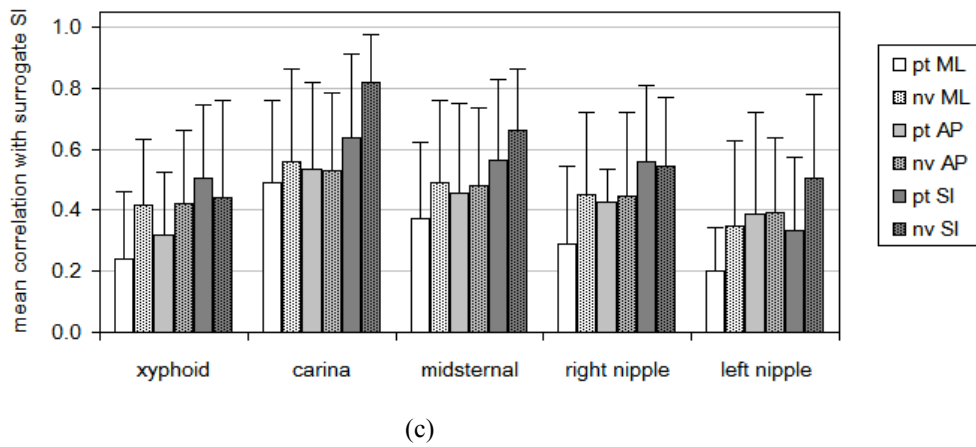
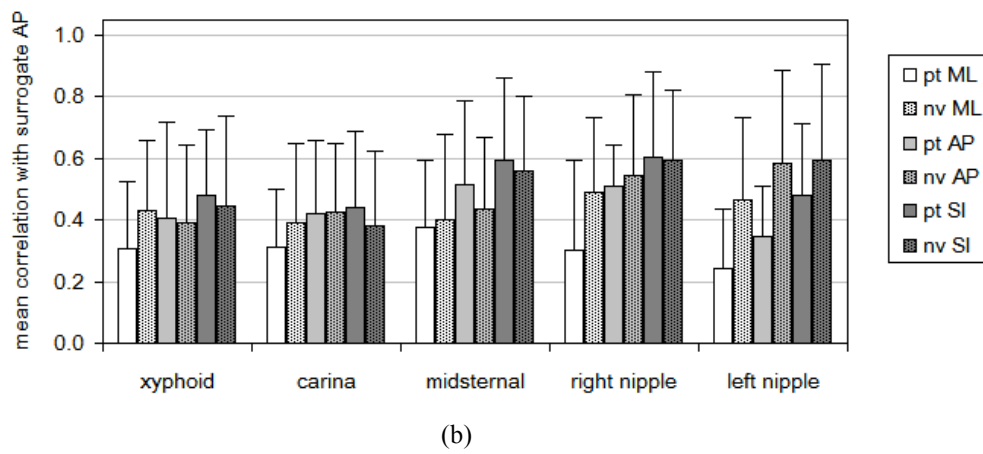
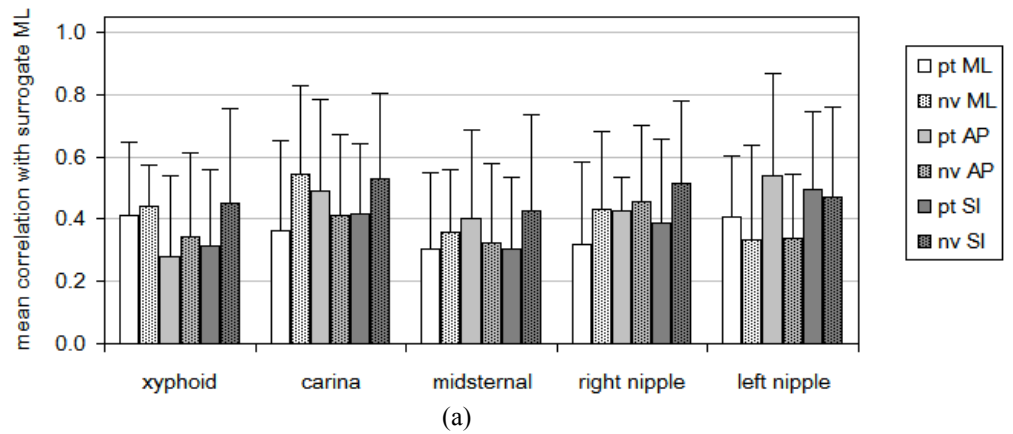


Figure 6.2 Mean and standard deviations of correlation between anatomical surrogate and tumor for surrogate (a) ML, (b) AP, and (c) SI coordinates. pt = primary tumors, nv = nodal volumes.

We determined the anatomical surrogate coordinate that was best correlated with each tumor/node coordinate (Figure 6.3). Since some surrogates were not visible in every 4D CT, we normalized the histogram by dividing each anatomical surrogate coordinate count by the number of target coordinates (number of nodal volumes and primary tumors times three orthogonal directions) available for comparison. The carina SI motion was most correlated with both primary tumor and nodal volume motion more often than any other anatomical surrogate coordinate. The mid-sternal AP motion and carina ML motion showed a better correlation with motion of the primary tumor than did the coordinates of other anatomical surrogates, while the nipple AP motion showed a better correlation with motion of the nodes than anatomical surrogate coordinates.

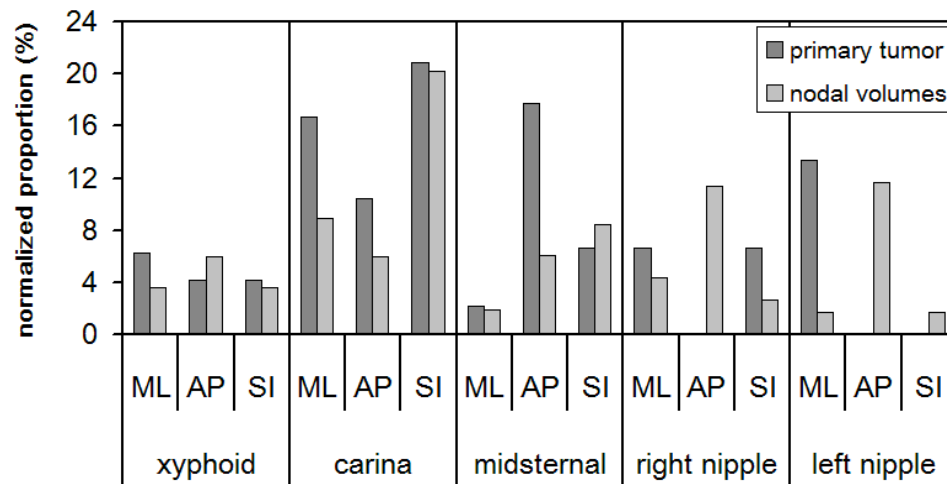


Figure 6.3 Proportion of primary tumor and nodal volume coordinates that are most highly correlated with each anatomical surrogate coordinate, normalized according to the quantity of data available for that anatomical surrogate.

### 6.3.1. Inferring Position of Primary Tumor and Nodes Using Anatomical Surrogates

We created OLS and PLS models from a randomly chosen subset of 3D datasets corresponding to respiratory phases and using all available surrogates for each patient dataset. While the quantity of latent variables,  $A$ , varied for each dataset, most PLS models (100% for 3-phase models decreasing to 65% for 8-phase models) were based on a single latent variable. The models' errors varied with the number of contoured 3D datasets from the 4D CT used to train the models (Figure 6.4). OLS model error decreased slightly when the number of image sets corresponding to respiratory phases was increased from 3 (mean = 1.1 mm) to 4 (mean = 1.0 mm) but increased monotonically with each additional contoured respiratory phase image set. In contrast, the mean PLS error decreased monotonically from 1.0 mm for 3 phases to 0.8 mm for 8 phases. Errors for nodal volumes were comparable to those of primary tumors. Mean PLS error was significantly less than mean OLS error ( $p < 0.05$ ) for each quantity of training phases.

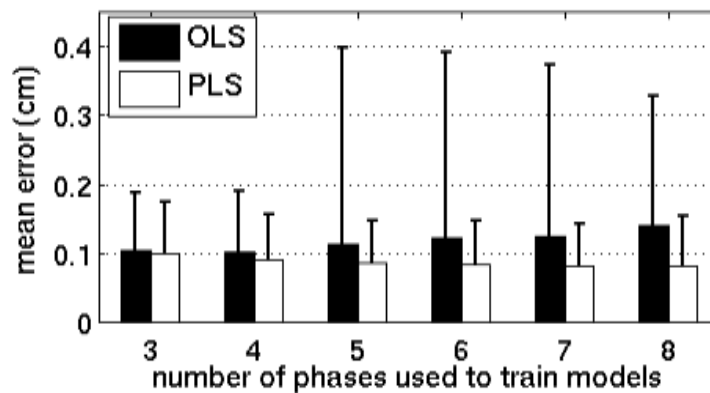


Figure 6.4 Means and standard deviations (error bars) of OLS and PLS errors for models trained on a range (3-8) of quantities of contoured volumetric respiratory phase bin images. The standard deviation of the PLS errors is smaller and more consistent than the standard deviation of the OLS errors.



The average model errors were minimized when the 0%, 40%, and 70% phase bins and the 0%, 40%, and 80% phase bins were used to create the model with OLS and PLS, respectively. In the following analyses, OLS analyses referring to “3-phase” models refer to models trained on data from the datasets corresponding to the 0%, 40%, and 70% respiratory phases; PLS analyses referring to “3-phase” models refer to models trained on data from the datasets corresponding to the 0%, 40%, and 80% respiratory phases.

The overall mean ( $\pm$  standard deviation) 3-phase model error for all nodal volumes and primary tumors included in the study and when all anatomical surrogates were used to create the model was  $0.8 \pm 0.5$  mm for OLS and  $0.8 \pm 0.5$  mm for PLS. Model error generally increased with increasing peak-to-peak motion of the target coordinates (Figure 6.5). The mean ( $\pm$  standard deviation) model error for target coordinates whose motion was greater than 5 mm was  $1.1 \pm 0.6$  mm for OLS and  $1.1 \pm 0.5$  mm for PLS. PLS errors for 3-phase models exceeded 2 mm in only 7% of inferred positions (Figure 6.6).

The mean ( $\pm$  standard deviation) 3-phase PLS model error for upper, middle, and lower mediastinal nodes were  $0.9 \pm 0.6$  mm,  $0.9 \pm 0.7$  mm, and  $1.1 \pm 0.8$  mm, respectively. Complete OLS and PLS results are included in Figure 6.7.

Lastly, we created 3-phase models using 3D carina position data alone. The overall mean ( $\pm$  standard deviation) errors for carina-only OLS and PLS models were  $2.4 \pm 1.1$  mm and  $1.1 \pm 1.1$  mm. The carina-only PLS mean ( $\pm$  standard deviation) errors for primary tumors and nodal volumes were  $1.2 \pm 1.4$  mm and  $1.1 \pm 0.9$  mm, respectively.

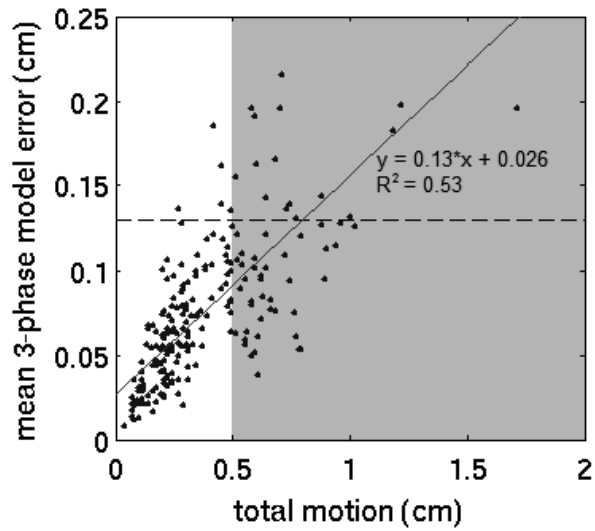


Figure 6.5 Target coordinate peak-to-peak motion vs. mean 3-phase PLS model error. Mean error (1.1 mm) for coordinates with peak-to-peak motion >0.5 cm (points in the gray area) is indicated by the dashed line.

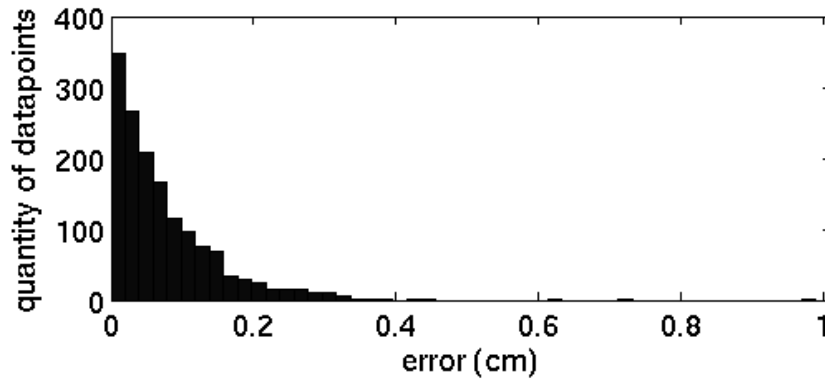


Figure 6.6 Histogram summarizing inferred position errors of 3-phase PLS models, including all primary tumors and nodal volumes in the dataset. Errors exceeded 0.2 cm in 7% of inferred positions.

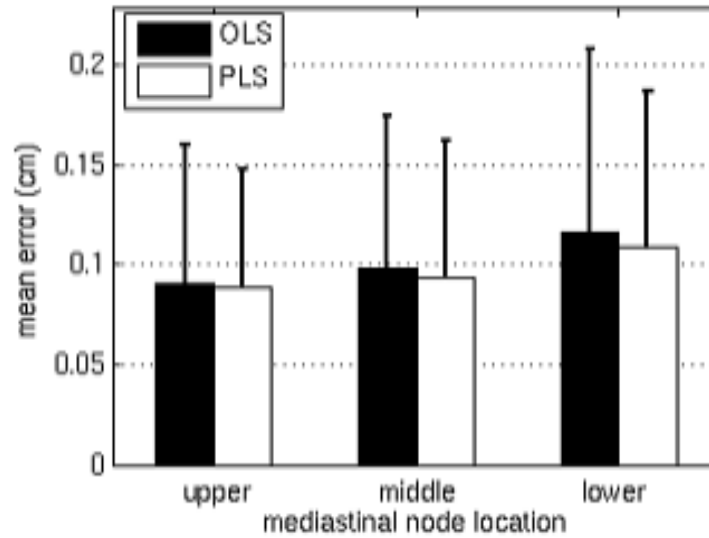


Figure 6.7 Mean and standard deviation (error bars) of 3-phase model error for nodal volumes, subdivided by zone of nodal station.

#### 6.4. Discussion

To our knowledge, the correlation between lung tumor motion and multiple respiratory surrogates' motion in 4D CT images has not been reported previously. Our results indicate that it is possible to model both primary tumor and nodal volume motion in Stage III lung cancer from anatomical respiratory surrogates. Our main findings were that 1) correlation of tumor motion with a specific respiratory surrogate was patient-specific, 2) carina SI motion was best-correlated with both primary tumor and nodal volume motions more often than any other anatomical surrogate coordinate, and 3) mean modeling error using PLS was on the order of CT resolution

The correlations in our study were lower than the correlations between *abdominal* tumor motion and surrogate motion in 4D CT images reported by Beddar *et al.* and Gierga *et al.*<sup>3,56</sup> However, both Gierga *et al.* and Ozhasoglu *et al.* observed that surrogate

motion and abdominal tumor motion are in phase, whereas the common phase differences between lung tumor and surrogates result in decreased correlation.<sup>3,6</sup> Gierga suggested that variability in abdominal- and chest-breathing may contribute to a complex relationship between respiratory surrogates and thoracic tissue motion, whereas the relationship between abdominal skin markers and abdominal tumor motion is more direct. This is supported Koch *et al.*, who reported correlations between external respiratory surrogate motion and pulmonary tissue motion that were comparable to the surrogate-target correlations in our study.<sup>76</sup>

In agreement with Koch *et al.* and Yan *et al.*, no single respiratory surrogate was consistently better correlated to tumor or nodal volume motion.<sup>33,76</sup> Rather, the correlation of tumor motion with a specific respiratory surrogate varies by patient. In addition, ML or SI surrogate motion was sometimes better correlated with target motion than AP motion. This implies that external markers tracking only skin AP motion, though common, may not be ideal for all patients.

We did not use the diaphragm as a respiratory surrogate in this study because of the difficulty in localizing the same portion of the diaphragm in images corresponding to the different respiratory phases. The carina is smaller, less deformable, and easier to localize accurately in 4D CT images. The performance of the carina-only models is in agreement with Higgins *et al.*, who found that the carina may be better suited as a registration landmark for inter-fraction patient alignment than the lung tumor itself.<sup>77</sup>

To date, only a few studies have compared carina positions to tumor or nodal volume positions. Van der Weide *et al.* reported that carina SI motion is well-correlated

with total lung volume, while Piet *et al.* reported that the distance between the carina and nodal volumes is highly variable.<sup>78-79</sup> However, Piet *et al.* did not attempt to characterize the relationship between carina motion and nodal volume motion. We found that the mean error for carina-only PLS models was 1.1 mm, an average of less than 0.5 mm greater than mean error of PLS models incorporating data from all surrogates. The proximity of the carina to locally advanced lung cancer target volumes and its tendency to be in phase with target motion make the carina well-suited to be a surrogate for Stage III primary tumor and nodal volume motion.<sup>78</sup>

When only 3 phases were used to train the models, the sets of 3 phase bins for which target position prediction was most accurate were the 0%, 40%, and either 70% (for OLS) or 80% (for PLS). The 0% phase bin represents end-inspiration. The phase associated with end-expiration varies by patient due to the gradual change in direction at the end of expiration. Thus, the three phase bins used to train the models include one extreme position (0% phase) and, we speculate, two additional phase bins representing the partial inhalation and partial exhalation data are necessary to characterize the path of motion of the target.

The mean 3-phase carina-only PLS model accuracies for primary tumors and nodal volumes differed by only 0.1 mm. Localization accuracy for superiorly positioned mediastinal nodes was slightly better than for inferior nodes. Our conclusion that the model error was positively correlated with peak-to-peak target motion is in agreement with prior studies showing that mediastinal nodes below the carina move more than mediastinal nodes in superior stations.<sup>70-72</sup>

Our results are based on data acquired during normal respiration without coaching aids. We speculate that our models may be improved by using training or audio-visual coaching to induce more regular breathing during 4D CT acquisition. Finally, while our method does not take target volume deformation into account, Liu *et al.* and Wu *et al.* showed that deformable and rotational registration, respectively, results in negligible improvement over rigid tumor registration across 4D CT phases.<sup>80-81</sup> Thus, our method of combining centroid tracking with target contours determined manually in a single respiratory phase bin image is likely to be sufficient for target delineation in 4D CT.

The modeling methods described in this study may make it possible to localize targets in uncontoured images with an accuracy of approximately 1 mm. This technique would require manually identifying anatomical surrogates in only three phases. Comprehensive motion management in Stage III lung cancer, including developing accurate patient-specific treatment margins to account for motion, may be made more accessible, and thus treatment more effective, by reducing the contouring burden of 4D CT through models similar to those tested in this study.

## 6.5. Conclusions

In summary, we established the feasibility of inferring the primary tumor and nodal volume motion from anatomical surrogates in 16 4D CT scans of Stage III lung cancer. The results from this work suggest that inferential modeling may have the potential to decrease the time required to process 4D CT scans, thereby improving therapy by allowing for incorporation of patient-specific margins in the planning process.

## CHAPTER 7: Online Monitoring and Error Detection of Real-Time Tumor Displacement Prediction Accuracy Using Control Limits on Respiratory Surrogate Statistics

### 7.1. Introduction

Tumor motion inferred from an external marker block during gated radiation treatments varies beam-to-beam and day-to-day with no apparent external warning.<sup>21</sup> *To our knowledge, no prospective method for detecting inferential model breakdown from surrogate signals has been developed.* Instead, systems must frequently interrupt treatment to validate a model through additional ground-truth measurements of tumor position. The Cyberknife Synchrony<sup>TM</sup> system, for instance, validates its model at a user-selected rate of about once per minute by localizing tumor-implanted fiducials with stereoscopic radiographs.<sup>18</sup> This technique of pre-scheduled intermittent data collection for model validation has at least three shortcomings:

- (1) If changes to the tumor-surrogate relationship occur shortly after one tumor localization, then the model can have large localization errors until the changes are detected at the next tumor localization minutes later;
- (2) Added and unnecessary tumor localizations not leading to model updates result in unnecessary exposure to ionizing radiation; and

(3) Pausing for image-based tumor localization extends the duration of the treatment fraction.

In this study, we propose a novel method for continuously monitoring a respiratory surrogate model of tumor motion through exclusive analysis of respiratory surrogate measurements (Figure 7.1). The purpose of this study was to describe and evaluate Hotelling's  $T^2$  statistic and the input variable squared prediction error,  $Q^{(X)}$ , for predicting the accuracy of tumor localization models in lung, liver and pancreas cases. The impact of this monitoring method on clinical workflow was also evaluated.

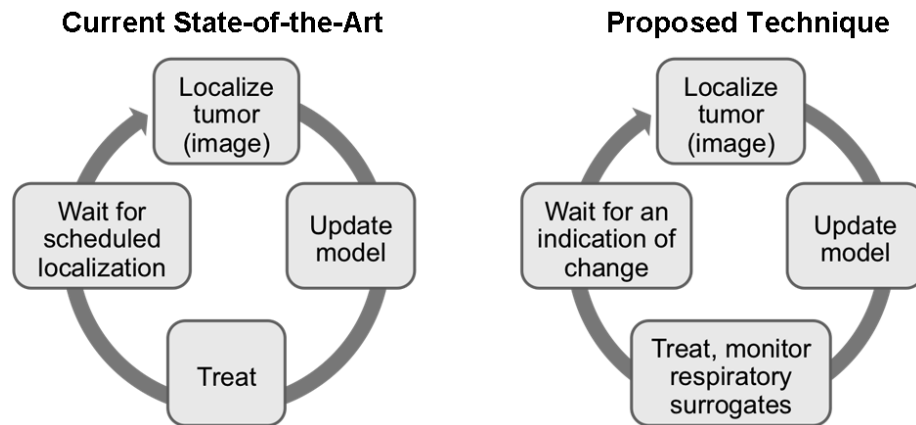


Figure 7.1 Schematic of proposed improvement to respiratory surrogate-based model monitoring.



## 7.2. Methods

### 7.2.1. Data

A database of Cyberknife Synchrony<sup>TM</sup> system log files consisting of 130 fractions from 63 lung cancer patients, 10 fractions from 5 liver cancer patients, and 48 fractions from 23 pancreas cancer patients was analyzed. The Cyberknife Synchrony<sup>TM</sup> log files included independently measured but concurrent 3D tumor and external marker localizations captured once every 3 beams (or an average of 63 sec apart). Tumors were localized as the centroid of a set of implanted fiducial markers measured in stereoscopic radiographs. Three LED surrogate markers affixed to the torso were localized optically by a camera system. The position of the tumor was aligned in time with those of the external markers according to the timestamps in the system log files. Each treatment fraction dataset consisted of at least 40 (ranging from 40 to 112, median of 61) concurrent tumor and external sensor localizations. The data was truncated to include only the longest period of uninterrupted treatment in each fraction and to exclude both pre-treatment image acquisitions and unplanned radiographs acquired during treatment for the purpose of repositioning the patient.

### 7.2.2. Partial Least Squares (PLS) for Predicting Tumor Positions

A Partial Least Squares (PLS) model for inferring tumor position from the surrogate marker displacements was developed for each treatment fraction, as described in Section 2.6.2. Tumor position was predicted as  $\hat{Y} = X \cdot B$  or, from a single new set of measurements,  $z_{new}$ , as  $\hat{y}_{new} = z_{new} \cdot B$ . The inferential model error,  $e$ , was calculated as

$e = \sqrt{\sum (\hat{y}_{new} - y_{new})^2}$ , the Euclidean distance between PLS-predicted tumor positions ( $\hat{y}_{new}$ ) and radiographically measured tumor predictions ( $y_{new}$ ).

### 7.2.3. Tumor Motion Models and Model Monitoring

Two PLS models were created for each training dataset: one for prediction and a second for monitoring. In our previous work (Section 4.3.1), we have shown that the input projection process leads to models that can more accurately predict tumor displacement from surrogate marker motion. However, we have found that projecting the inputs degrades the ability to monitor the model for tumor-surrogate relationship changes. The PLS models differed in their input matrix,  $X$ , as follows.

In either case, the first 10 samples ( $n = 10$ ) of concurrent surrogate marker and tumor localizations in the treatment fraction dataset were used as training data for the model. For the monitoring model,  $X$  was a  $10 \times 9$  matrix describing the 3D positions of three surrogate markers at 10 samples. For the tumor displacement prediction model,  $X$  was a  $10 \times 3$  matrix in which each column was a one-dimensional (1D) representation of the three-dimensional (3D) motion of one of the surrogate markers. These 1D surrogate signals were created by orthogonally projecting the surrogate marker displacements captured during the training data acquisition period onto a line. This line was defined by the displacements' 3D mean,  $M$ , and first principal component vector (Figure 7.2). The 1D representation for each sample was defined as the distance between the projected point and  $M$ .

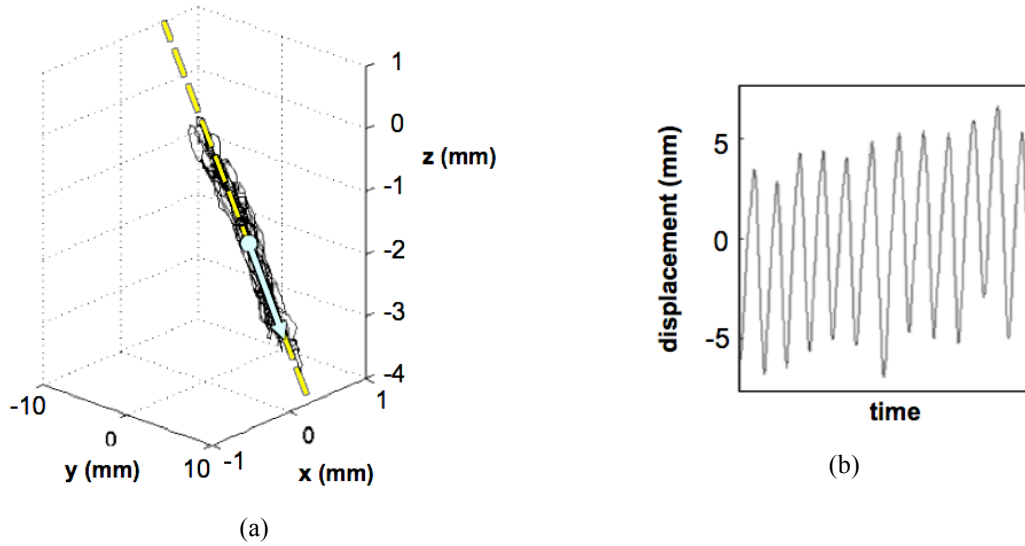


Figure 7.2 The surrogate marker projection process. (a) Example of 3D surrogate marker motion data, including its mean and first principal component vector (blue dot and arrow, respectively) and its projection line (dashed). (b) The 1D representation of the 3D data in (a).

#### 7.2.4. Respiratory Surrogate Metrics

Respiratory surrogate data captured during the initial model development period were compared to respiratory surrogate data captured over the course of a treatment fraction. Using this technique, whether the real-time tumor displacement prediction is occurring under conditions described by the model could be determined. Thus, the quality of the model can be monitored without stopping treatment to explicitly measure the tumor position.

For each  $1 \times 3$  vector of inputs,  $z_i$ , at sample  $i$ , an associated score vector,  $\hat{t}_i$ , was calculated as  $\hat{t}_i^T = z_i \cdot \hat{W}$ , where  $\hat{W}$  was the compressed weight vector calculated as part of the PLS regression process. The scores were then used to calculate the associated Hotelling statistic,  $T^2$ , and input variable squared prediction error,  $Q^{(X)}$ , for each surrogate

marker displacement dataset as described in Section 2.8. The  $T^2$  and  $Q^{(X)}$  statistics rely on measurements of the surrogate markers exclusively and do not utilize gold-standard tumor position measurements.

## 7.2.5. Performance of Respiratory Surrogate-Based Monitoring

### 7.2.5.1. Large Error Detection

Treatment fraction-specific limits on  $T^2$  and  $Q^{(X)}$  were calculated and tested for  $(1 - \alpha)$  percentile confidence limits for  $0 < \alpha < 1$ . The confidence limits were used as control limits for  $T^2$  and  $Q^{(X)}$ .

For  $T^2$ , confidence limits were determined from  $T_\alpha^2 = \frac{(n^2 - 1)A}{n(n - A)} F_\alpha(A, n - A)$ ,

where  $n = 10$  was the quantity of training samples used to generate the model, one score was used in the PLS model created to monitor the tumor localization model ( $A = 1$ ), and  $F_\alpha(A, n - A)$  was the upper  $(100\%) \cdot (\alpha)$  critical point of the  $F$  distribution with  $(A, n - A)$  degrees of freedom.

Confidence limits on  $Q^{(X)}$  were calculated through the Jackson-Mudholkar formula,<sup>51</sup>  $Q_\alpha = \theta_1 \left[ 1 - \frac{\theta_2 h_0 (1 - h_0)}{\theta_1^2} + \frac{z_\alpha \sqrt{2\theta_2 h_0^2}}{\theta_1} \right]^{1/h_0}$ , in which  $z_\alpha$  is the upper  $(100\%) \cdot (\alpha)$

critical point of the normal distribution,  $\theta_j = \sum_{i=A+1}^m \lambda_i^j$ ,  $n = 10$ ,  $h_0 = 1 - \frac{2\theta_1\theta_3}{3\theta_2^2}$ , and  $\lambda_i$  is the

$i$ th eigenvalue of  $(\hat{z}_{new,i} - z_{new,i})^T (\hat{z}_{new,i} - z_{new,i})$ .

The ability of  $T^2$  and  $Q^{(X)}$  to predict whether a tumor displacement prediction is accurate to within 3 mm was evaluated for each  $\alpha$ . Prediction of large ( $>3$  mm) errors was based on whether  $T^2$  or  $Q^{(X)}$  exceeded the treatment fraction-specific confidence limits and was validated against radiographic measurements. To evaluate the performance of the method, sensitivity and specificity were explored under various conditions. Sensitivity measured the proportion of errors  $>3$  mm that was detected. Specificity represents the proportion of errors  $<3$  mm that was identified as likely to be  $<3$  mm. Sensitivity and specificity were determined for: (1)  $T^2$  confidence limit; (2)  $Q^{(X)}$  confidence limit; and (3) the union of results from  $T^2$  confidence limit and  $Q^{(X)}$  confidence limit, in which the method predicts large error if either  $T^2$  or  $Q^{(X)}$  exceeds its respective confidence limit threshold. Receiver operating characteristic (ROC) analysis was performed to evaluate sensitivity versus specificity at any confidence limit between 0% and 100%. Matlab code written to implement this analysis is included in Appendix B.

In addition to the surrogate marker measurements concurrent with the tumor displacement, the utility of past surrogate marker measurements was evaluated for data up to 10 sec prior to the surrogate marker-based tumor localization. For this multiple measurement method, the proportion of  $T^2$ ,  $Q^{(X)}$ , or  $T^2 \cup Q^{(X)}$  values in the testing period that exceeded the confidence limit(s) was calculated. A threshold value for predicting large inferential model errors (for example, *at least 10%* of the measurements during the 5 sec prior to the tumor localization) was selected to maximize specificity at the target sensitivity.

#### 7.2.5.2. Time to Error and Time to Alarm

For each treatment fraction and monitoring method, the times from the end of the training dataset to the first large error (time to error) and to the first confidence limit-based indication of large error (time to alarm) were determined. Results were compared to the timing of images captured by the Cyberknife Synchrony™ system to validate its own model during the treatment.

#### 7.2.5.3. Effect of Tumor Site

Results were stratified by tumor site for lung (130 fractions) and pancreas (48 fractions) cases, using 2 sec of surrogate marker data preceding the tumor localization.

### 7.3. Results

#### 7.3.1. Large Error Detection

The  $T^2$  and  $Q^{(X)}$  statistics were able to indicate such phenomena as large errors associated with gradual decreases in inferential model accuracy and transient surrogate marker tracking errors. All three confidence limit tests,  $T^2$ ,  $Q^{(X)}$ , and  $T^2 \cup Q^{(X)}$ , were predictive of large errors. Sensitivity and specificity varied with confidence limit selection, with increasing sensitivity associated with decreased specificity (Figure 7.3).  $T^2 \cup Q^{(X)}$  was associated with specificity 1-2% higher than either  $T^2$  or  $Q^{(X)}$  alone at 90-95% sensitivity (Table 7.1).

Neither  $T^2$  nor  $Q^{(X)}$  increased monotonically, and  $T^2$  in particular varied cyclically with phase of respiration (Figure 7.4). Incorporating 2 sec of past measurements of

surrogate marker displacements improved model monitoring performance for  $Q^{(X)}$  and  $T^2 \cup Q^{(X)}$ . For 95% sensitivity, the best specificity for  $T^2 \cup Q^{(X)}$  was achieved by requiring that 5% of  $T^2 \cup Q^{(X)}$  values acquired over the past 3 sec exceed the confidence limit threshold.

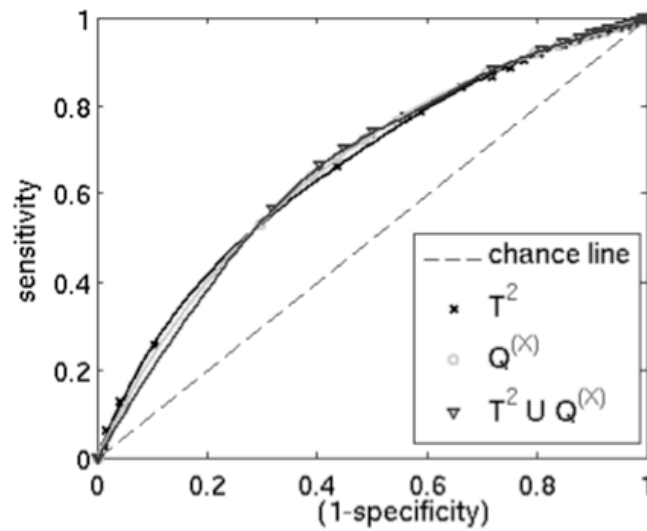


Figure 7.3 Receiver operator characteristic (ROC) curves showing ability to predict localization errors exceeding 3 mm for various confidence levels.

Table 7.1 Summary of monitoring performance for all tumor sites at 90% and 95% sensitivity.

Method	Sensitivity	Specificity	Time to alarm	
			mean	st. dev.
$T^2$	90%	23%	6.0 min	8.8 min
$Q^{(X)}$	90%	24%	7.6 min	9.9 min
$T^2 \cup Q^{(X)}$	90%	24%	7.2 min	9.8 min
$T^2$	95%	13%	4.0 min	8.1 min
$Q^{(X)}$	95%	14%	4.6 min	8.1 min
$T^2 \cup Q^{(X)}$	95%	15%	5.3 min	8.2 min

### 7.3.1. Time to Error and Time to Alarm

For the inferential modeling method used in this study, the mean ( $\pm$  standard deviation) time from the last tumor localization to an error  $>3$  mm was  $12 \pm 12$  min for those fractions in which errors  $>3$  mm. This mean time excludes the 6% of fractions in which no tumor position prediction error was  $>3$  mm.

For this dataset, the mean time to alarm for the Cyberknife Synchrony system was 1.1 min. For  $T^2$  and  $Q^{(X)}$  values giving the highest specificity at 90% sensitivity (Table 7.1), the mean times from training data to indication of large errors (mean time to alarm) for  $T^2$ ,  $Q^{(X)}$ , and  $T^2 \cup Q^{(X)}$  were 6.0 min, 7.6 min, and 7.2 min, respectively. In 5% of fractions, the error never exceeded 3 mm. However, there were no fractions for which neither  $T^2$  nor  $Q^{(X)}$  did not exceed the confidence limit threshold for at least one set of surrogate marker measurements.



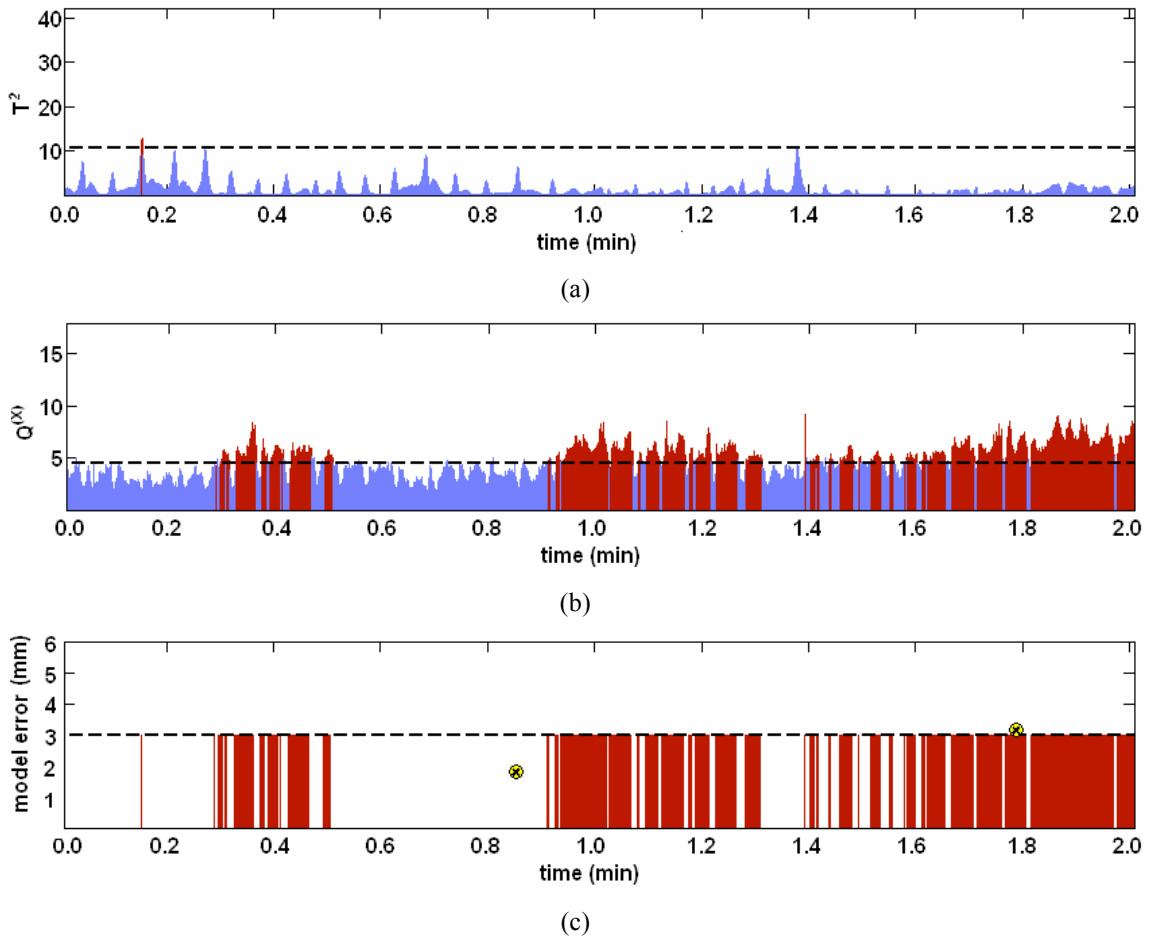


Figure 7.4 Example of (a)  $T^2$ , (b)  $Q^{(X)}$ , and (c) tumor localization error versus time elapsed since the training data. In (a) and (b), horizontal dashed lines represent control limits, and times in which the control limit is exceeded are shaded red. In (c), the horizontal dashed line represents a 3 mm error limit, and radiographic tumor localizations errors are indicated at  $t = 0.8$  min and  $t = 1.8$  min by circled x's ( $\otimes$ ). It is likely that localization errors exceed 3 mm from 0.3 to 0.5 min and after 0.9 min, but radiographic validation is only possible at two moments over this 2 min period.

### 7.3.2. Effect of Tumor Site

There was no significant difference between lung and pancreas cases in time to alarm (Figure 7.5). The specificities for each site were equal to the specificities for the pooled lung, liver, and pancreas results at 90-95% sensitivity given in Table 7.1 (above).

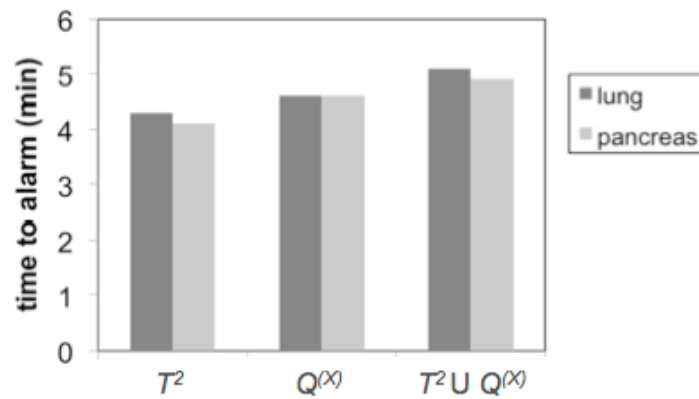


Figure 7.5 Comparison of mean time to alarm for lung and pancreas results using 2 sec of data.

### 7.4. Discussion

The results of this study establish the feasibility of using confidence limits on  $T^2$  and  $Q^{(X)}$  statistics of respiratory surrogate measurements in online monitoring of the accuracy of real-time respiration-induced tumor motion models. The  $T^2$  and  $Q^{(X)}$  statistics were able to indicate whether inferential model errors exceeded 3 mm with high sensitivity. For

95% error prediction sensitivity, specificity was 15%, and the mean time to alarm was 5.3 min. Modest improvements in specificity were achieved by combining  $T^2$  and  $Q^{(X)}$  results and by expanding the input to include the previous 3 sec of respiratory surrogate data.

Real-time motion management systems rely on rapid, accurate tumor localization. For respiratory surrogate-based systems, current clinical practice is to establish a model before beginning treatment and then either to assume that the model will remain valid or to periodically validate the model according to some pre-established schedule. If the gold-standard radiographic tumor localizations are too sparse, large targeting errors may occur in the interim. Conversely, radiographic images captured while the model remains accurate result in exposure to unnecessary ionizing radiation and extend the duration of the treatment fraction. Seppenwoolde *et al.* found that the timing of gold-standard image-based tumor localizations determines the accuracy of the model but that the patient-specific benefit of increasing the imaging frequency varies widely.<sup>18</sup> The method described by this study is a novel, knowledge-based technique for timing image acquisitions used to update respiratory surrogate tumor motion models by relying exclusively on surrogate measurements.

Applying a confidence limit-based threshold made it possible to detect errors >3 mm with a high degree of sensitivity (>90%). As shown in the ROC curves of Figure 7.4, varying  $\alpha$  led to a tradeoff between sensitivity and specificity. In the context of this application, sensitivity refers to the probability that a large error will be detected by the confidence limit method. Thus, in this dissertation, we have focused on parameters leading to high (90-95%) sensitivity and decreased (13-24%) specificity. Low specificity

indicates an increased rate of false positives. In this application, false positives correspond to unnecessary image acquisitions. To investigate the impact of this relatively low specificity on clinical workflow, we have described the time to alarm for 90-95% sensitivity.

The mean time to alarm for 90-95% sensitivity was 4-8 min, representing a four- to eight-fold decrease in image acquisition frequency over the Cyberknife Synchrony™ method. Because there was considerable variability in the time to errors >3 mm, acquiring images at a preselected regular interval often would result in missing large errors. For this dataset, the Cyberknife Synchrony™ system localized the tumor via radiographs every third beam delivered, with a mean interval of 63 sec between image acquisitions. The current version of the Cyberknife Synchrony™ software allows the operator to select a constant time interval of up to 2.5 min between radiographic image acquisitions. This maximum time interval for the Cyberknife Synchrony™ system is more than double the average frequency of the proposed  $T^2 \cup Q^{(x)}$  method.

This study determined the performance of respiratory surrogate monitoring for predicting PLS-based tumor localization errors. This method can be extended to other tumor displacement inferential approaches to minimize the imaging frequency of existing systems, thereby decreasing treatment interruptions and overall patient in-room time. Through monitoring, this method also has the potential to increase the targeting accuracy of any real-time motion compensation device, including radiation gating systems. Berbeco *et al.* has concluded that gating margins based on a single simulation session at the beginning of the treatment may not be enough to evaluate residual motion of a gated

treatment.<sup>21</sup> Respiratory surrogate monitoring through  $T^2$  and  $Q^{(X)}$  can detect increases in residual motion during the treatment, allowing the clinicians to pause treatment to collect images *when necessary* to ensure that tumor motion is in accordance with the internal margin for the plan.

In many cases, the Hotelling statistic ( $T^2$ ) and the input variable squared prediction error ( $Q^{(X)}$ ) both exceeded confidence limit thresholds together, a result commonly seen in process control monitoring through these metrics.<sup>49</sup> However, the statistics did not always indicate alarm concurrently. In some cases  $T^2$  indicated large error first, but in other cases  $Q^{(X)}$  indicated large error first. As a result, combining the metrics resulted in a slight increase in performance of the method. Mathematically,  $T^2$  and  $Q^{(X)}$  are independent. Their concurrent increase is indicative of a common cause: some change in the tumor-surrogate relationship. Transient and long-term changes in the tumor-surrogate relationship have been described by Ozhasoglu *et al.* (2002), Seppenwoolde *et al.* (2002), Hoisak *et al.* (2004), and Ionsascu *et al.* (2007) and are manifested as shifts in the phase offset between tumor and surrogate motion, baseline drifts in tumor position or surrogate signal, or other complex behavior leading to lapses in correlation. Our previous work has shown that the tumor-surrogate relationship changes during most treatment fractions (Chapter 5).

The method described in this study resembles statistical process control (SPC) monitoring utilized in chemical process control applications.<sup>49,51,82</sup> However, in classical SPC, metrics are derived directly from the model that is being monitored. By contrast, in this method separate models for monitoring and for tumor displacement prediction were

created. For optimal tumor localization accuracy, it was necessary to project surrogate marker data from 3D to 1D (Chapter 4). This reduction in input dimensionality from  $m = 9$  to  $m = 3$  reduced the number of scores available for calculating  $T^2$ , which uses scores 1 to  $A$ , and  $Q^{(X)}$ , which uses scores  $A+1$  to  $m$ . As a result, reducing input dimensionality from 9 to 3 decreased the specificity, and consequently the time to alarm, for a given sensitivity. For instance, by utilizing the 3D (9 input) marker data for monitoring, at 95% sensitivity the mean time to alarm increased from 2-4 min to 4-8 min.

Neither  $T^2$  nor  $Q^{(X)}$  increased monotonically over time. The  $T^2$  statistic was cyclic in nature, increasing during certain phases of respiration, and both  $T^2$  and  $Q^{(X)}$  were associated with some degree of noise. In the future, it may be possible to reduce this periodicity by carefully selecting training data encompassing a wide range of respiratory phases. It was possible to improve specificity for  $Q^{(X)}$  and  $T^2 \cup Q^{(X)}$  by considering time trends in  $T^2$  and  $Q^{(X)}$  values. Utilizing multiple surrogate marker data samples (1-3 sec of data from 26 Hz measurements) helped to overcome the effects of both noise and training data selection.

## 7.5. Conclusions

In this work, we present a novel approach to determining tumor position prediction errors in real time and from measurements of external marker respiratory surrogates exclusively. In a large cohort of lung, liver, and pancreas cases, the  $T^2$  and  $Q^{(X)}$  statistics can predict whether tumor localization error exceeds 3 mm with 95% sensitivity and 15% specificity and a mean time to alarm of 5.3 min. The mean time to alarm for 90-95% sensitivity was 4-8 min, representing a four- to eight-fold decrease in image acquisition

frequency over the Cyberknife Synchrony<sup>TM</sup> method. Thus, this approach has the potential to reduce imaging frequency and, consequently, imaging dose during respiratory-surrogate-guided treatments. Results did not differ by tumor site.

## CHAPTER 8: Maintaining Tumor Targeting Accuracy in Real-Time Tumor Motion Compensation Systems for Respiration- Induced Tumor Motion

### 8.1. Introduction

To ensure accuracy over the course of treatment, respiratory surrogate models of tumor motion can be rebuilt during the fraction from new training data.<sup>18</sup> Few studies have explored how best to update respiratory surrogate models to compensate for changes in the tumor-surrogate relationship. Seppenwoolde *et al.*, concluded that updating the model quickly after the tumor-surrogate relationship had changed can reduce overall residual error over the course of a fraction.<sup>18</sup> However, imaging the tumor to collect data for updating the model as frequently as Seppenwoolde *et al.* described, every 5-25 sec, may not be practical, as each image acquisition imparts non-therapeutic ionizing radiation.

In a previous chapter (Chapter 7), we evaluated a method for determining when to update a respiratory surrogate model without directly measuring tumor position. That initial study demonstrated the feasibility of monitoring respiratory surrogate models through external measurements alone, without explicitly measuring tumor position. However, *further study is needed to determine how the model accuracy and the frequency*



*of model updates for the surrogate monitoring method compare to that of either error-based methods or methods in which the model is updated at arbitrary intervals.*

The purpose of this study was to evaluate the impact of timing model updates based on respiratory surrogate monitoring. A database of concurrent radiographic tumor localizations and respiratory surrogate measurements from a large cohort of lung and pancreas cancer patients was analyzed retrospectively. The cases we considered for determining when to update a model were: (1) never, (2) when surrogate model-based tumor localization error exceeded 3 mm, (3) at each gold-standard tumor localization (once per minute), and (4) when either  $T^2$  or  $Q^{(X)}$  exceeded preset confidence limits.

## 8.2. Methods

### 8.2.1. Data

A database of Cyberknife Synchrony<sup>TM</sup> system log files was analyzed. 121 treatment fractions of lung tumor motion data from 61 patients and 45 treatment fractions of pancreas tumor motion data from 23 patients were considered. Each log file consisted of two sets of recordings that were aligned using system-recorded timestamps: (1) intermittent measurements of tumor position, as localized through identification of the centroid of 2-3 implanted fiducial markers in stereoscopic radiographs; and (2) frequent (26 Hz) measurements of the positions of each of three LED markers affixed to a form-fitting vest. Stereoscopic radiographs were captured once every three beams for a mean frequency of approximately once per minute. From these datasets we were able to extract

concurrent internal (tumor) and external (marker) localizations at each radiographic measurement.

### 8.2.2. Tumor Motion Prediction

For each treatment fraction, a regression model was created to predict tumor positions,  $Y$ , from the external marker data,  $R$ . The initial model was created from the first 6 radiographic tumor localizations in each treatment fraction.

As described in Section 2.6.2, the SIMPLS Partial Least Squares (PLS) regression algorithm was used to develop the respiratory surrogate tumor motion models. Three one-dimensional PLS inputs were derived from external surrogate data, one for each of the three external surrogate markers, as described in Section 4.2.3.1.

### 8.2.3. Model Monitoring and Updates

#### 8.2.3.1. Analysis of Respiratory Surrogate Marker Data

The relative motion of the external respiratory surrogate markers was characterized during the model training period and then, to monitor the model, was re-evaluated over the course of the treatment fraction. The  $T^2$  and  $Q^{(X)}$  statistics were utilized as described in Section 2.8. If either  $T^2$  or  $Q^{(X)}$  exceeded control limits determined from the 6 training data samples, the instantaneous tumor localization error was assumed to be greater than 3 mm. In the testing data captured after the 6 training data samples, the surrogate-based metrics were calculated from measurements of the surrogate markers exclusively and did not utilize additional image-based measurements of tumor position.

### 8.2.3.2. Updating the Tumor Displacement Model

To update the tumor displacement model at time  $t_0$ , a new model was trained on the six tumor localizations captured prior to  $t_0$ . The new model was applied to all respiratory surrogate marker positions in the dataset captured after  $t_0$ .

### 8.2.3.3. Model Update Timing

The tumor localization accuracy of the respiratory surrogate models was evaluated for four possible update timing methods. Each method was tested against 20 min of data following the initial 6-sample training dataset.

#### 8.2.3.3.1. Never Update

Currently, despite possible intra-fraction tumor-surrogate relationship changes, most clinics do not update respiratory surrogate models during gating procedures. To simulate this case, we applied the initial model based on the first 6 measurements in the treatment fraction to the entire 20 min testing dataset.

#### 8.2.3.3.2. Always Update

To evaluate the opposite extreme, we updated the model at each tumor localization (separated by an average of 63 sec) in the log files. Specifically, 1 sec after a radiographic tumor localization, the 6 most recent measurements were used to train a new model predicting tumor motion from external marker positions. This predictive model was then applied to predict tumor position up to the next update, 1 sec after the next radiographic tumor localization.

#### 8.2.3.3.3. Error-Based Update

The Cyberknife Synchrony™ system is an example of a device that periodically captures radiographs in order to validate its respiratory surrogate model. The radiographically measured tumor position is compared to the model-predicted tumor position. If the difference (the localization error) exceeds a user-set threshold such as 3 mm,<sup>8</sup> the model is updated. To simulate this process, a new model was created each time the localization error exceeded 3 mm. An updated model was applied to data acquired 1 sec after the each tumor localization error was greater than 3 mm.

#### 8.2.3.3.4. Respiratory Surrogate-Based Update

Rather than base the decision of whether to update a model on gold-standard tumor localizations, the respiratory surrogate method is based on external measurements alone. The  $T^2$  and  $Q^{(X)}$  values were evaluated for each set of surrogate marker measurements. If either  $T^2$  or  $Q^{(X)}$  of a sample exceeded the 70<sup>th</sup> percentile  $T^2$  or  $Q^{(X)}$  confidence limit, then a new model was created from the previous 6 localizations. This model was applied to data in the fraction following 1 sec after either  $T^2$  or  $Q^{(X)}$  exceeded its confidence limit threshold.

### 8.3. Results

The update timings differed considerably across the four methods. More frequent updates did not always correspond to more accurate tumor motion prediction (**Figure 8.1**).

### 8.3.1. Model Errors

Tumor localization errors (mean  $\pm$  standard deviation) for never, surrogate-based, error-based, and always update schema were  $2.4 \pm 1.2$  mm,  $1.9 \pm 0.9$  mm,  $1.9 \pm 0.8$  mm, and  $1.7 \pm 0.8$  mm, respectively (**Figure 8.2**). For never, surrogate-based, error-based, and always update methods, respectively, 7%, 3%, 3%, and 3% of tumor position prediction errors exceeded 5 mm, and 26%, 14%, 11%, and 13% exceeded 3 mm (**Figure 8.3**). Error distributions for update schema other than never-update did not differ significantly from one another (t-test,  $p > 0.05$ ). However, the never-update tumor localization errors were significantly larger (t-test,  $p < 0.05$ ) than those of the other update methods.

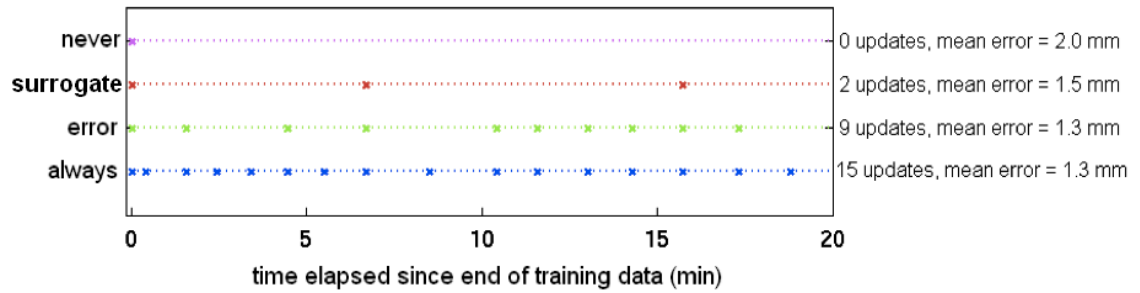


**Figure 8.1.** Timing of model updates for the four update methods in a representative treatment fraction. Updates are indicated by “x”s at the appropriate time. Results for this fraction for each method are summarized at right.

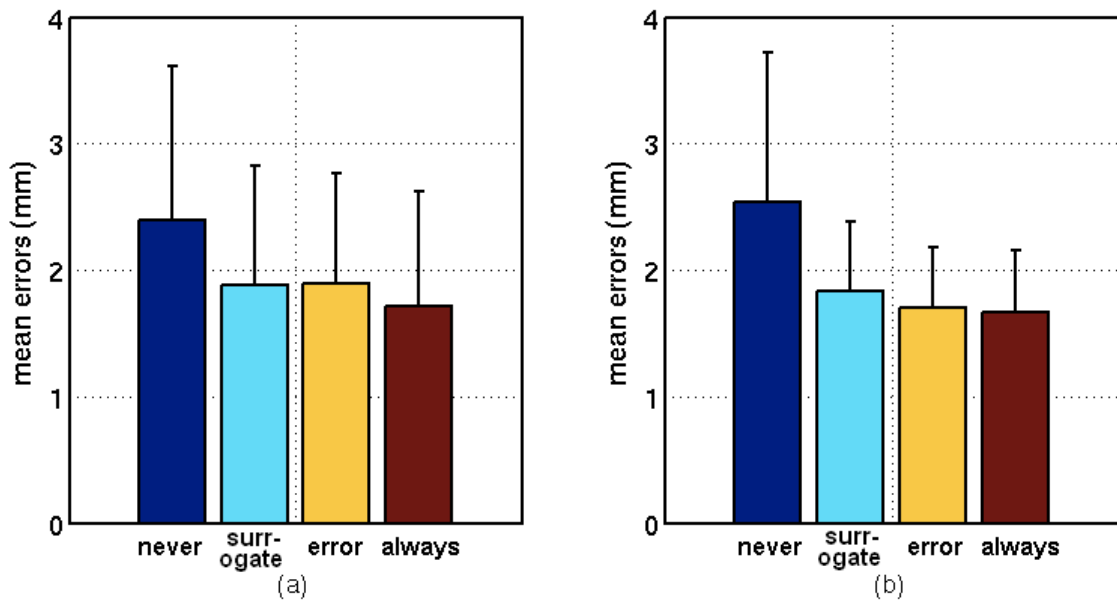


**Figure 8.2.** Mean and standard deviation (error bars) tumor position prediction errors over 20 min for each update method. There is no significant difference ( $p > 0.05$ ) between results for surrogate-based, error-based, and always update methods.

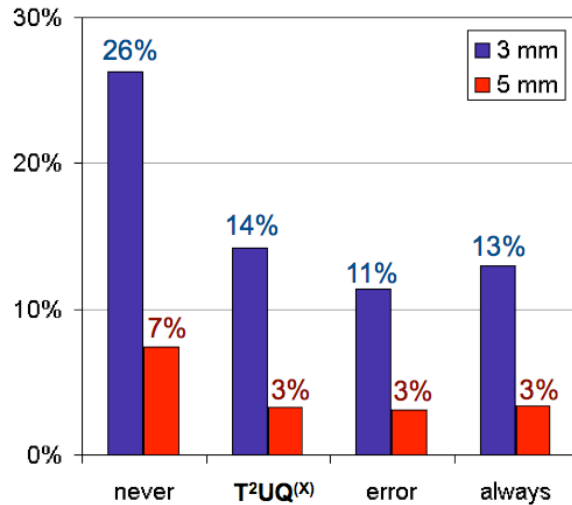


**Figure 8.3.** Incidence of large (>3 mm and >5 mm) errors for each update method.

### 8.3.2. Update Timing

The median numbers of updates over the course of 20 min were 0, 4, 9, and 24 for never, surrogate-based, error-based, and always update schema, respectively (**Figure 8.4**). There were significant (t-test,  $p < 0.05$ ) differences in quantities of updates between each of the four methods. 24% of the tumor localizations associated with an error-based update were also associated with a surrogate-based update, and 55% of tumor localizations that were associated with surrogate-based updates corresponded to simultaneous error-based updates.

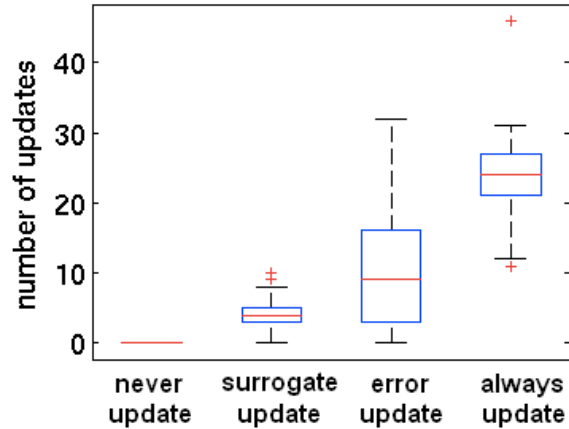


**Figure 8.4.** Numbers of model updates per 20-min fraction for each update method.

### 8.3.1. Site-Specific Results

Neither mean error nor number of updates was significantly associated with tumor site (lung vs. pancreas, two-way ANOVA,  $p > 0.05$ ).

## 8.4. Discussion

This study evaluated the hypothesis that intelligent model update timing can lead to an accurate model while limiting model update frequency. The results of this study indicated that more frequent updates do not guarantee a more accurate model. While any update method resulted in smaller tumor localization errors than no updates at all, errors were not significantly different across the three update methods (surrogate-based, error-based,



or always update). This lack of difference in tumor localization performance came about despite large differences in the mean number of updates in 20 min: 4, 9, and 24 for the surrogate-based, error-based and always updates methods, respectively.

The prediction accuracy of respiratory surrogate-based tumor localization models degrades over the course of a treatment fraction (Chapters 4-5). In Chapter 7, we concluded that the  $T^2$  and  $Q^{(X)}$  were able to predict large respiratory surrogate model errors with high sensitivity (95%) but limited specificity (15%). In this chapter, we have shown that instantaneous error may not be the best way to decide whether to update a model. By updating the model each time a localization error exceeded the threshold of 3 mm, many updates were carried out without significant improvement to mean model accuracy. Over the course of a fraction, the surrogate method was associated with more localization errors >3 mm than the error-based method (14% vs. 11% of localizations), but for both methods only 3% of errors were >5 mm. Despite no improvement in error, the error-based method required more than twice as many updates as the surrogate-based method. This result is in agreement with Seppenwoolde *et al.*, who also concluded that more frequent updates do not necessarily lead to a more accurate model.<sup>18</sup>

In both the error-based and the surrogate-based update methods, parameters can be selected to trade off between tumor localization error and number of updates. For error-based updates, 3 mm was used as the threshold, because it has been cited as a clinically utilized error threshold for the Cyberknife Synchrony system.<sup>18</sup> The surrogate metrics' confidence limits were set to the 70<sup>th</sup> percentile expected value, such that the accuracy was not significantly different than the error-based method. This allowed us to

compare number of updates for the two methods when localization errors were equal. For either technique, a larger localization error tolerance would necessitate fewer updates.

In this work, the number of updates was evaluated for 20 min of data. For many modern treatments, beam-on time is less than 20 min, but in-room time can be longer. At our institution, the patient is usually on the couch for about 20 min for conventionally fractionated treatments and for about 30 min for stereotactic body radiotherapy treatments. In practice, model update implementation would be implemented differently on each system, but it is likely that the process of capturing images for new model-building data during an update would take some time, potentially extending the duration of the treatment fraction. A shorter treatment would require fewer updates. Thus, even with respiration monitoring, it is important to complete a treatment fraction, including the setup process, as quickly as possible.

The surrogate-based monitoring method explored in this study was applied to PLS respiratory surrogate models. The  $T^2$  and  $Q^{(X)}$  metrics are based on the scores developed as part of the PLS regression process. However, it would be possible to monitor any multiple-input respiratory surrogate model through these metrics. In particular, because the PLS output is very similar to that of the Cyberknife Synchrony<sup>TM</sup> system (Chapter 4), it is likely that the surrogate-based monitoring method evaluated in this study would be equally effective for the Cyberknife Synchrony<sup>TM</sup> tumor localization algorithm. In any real-time tracking technology,<sup>18-19</sup> accurate tumor localization is essential, and a knowledge-based method for model update timing could improve system performance. This type of monitoring would also benefit gating technologies.<sup>21,60</sup> Berbeco *et al.* and

Cai *et al.* have shown that breath-to-breath variations even in the relatively stable end-exhale position necessitate use of an internal margin for gated treatments.<sup>21,83</sup>

The surrogate-based timing uses respiratory surrogate measurements alone. By contrast, the error-based method requires concurrent respiratory surrogate measurements and radiographic images to validate the model directly. For this work, to allow validation of the method, updates were limited to the moments at which gold-standard tumor localizations were available (about once per minute). However, because the surrogate method does not require internal localization, it has the potential to give early warnings of large errors by checking for updates at the surrogate measurement rate (26 Hz in this dataset). Further study is needed to determine how to best implement surrogate-based monitoring when high-frequency surrogate data is available.

### 8.5. Conclusions

With no model updates, mean tumor localization errors were 2.4 mm, and 26% of errors exceeded 3 mm. With the update methods, mean errors were reduced to 1.7-1.9 mm, and 11-14% of errors exceeded 3 mm. Differences in errors between surrogate-based, error-based, and always update methods were not significant, but the number of updates in a fraction varied considerably with update method. On average, the surrogate method required 44% as many updates as the error method and 17% as many updates as the always-update method.

## CHAPTER 9: Understanding the Performance of Control Limit-Based Monitoring of Respiratory Surrogate Tumor Motion Models

### 9.1. Introduction

The surrogate-based monitoring technique described in Chapters 7 and 8 is associated with poor specificity when tuned to high sensitivity. The consequence of low specificity is frequent model updates that interrupt treatment. Our surrogate-based monitoring technique consists of placing control limits on variables derived from model inputs, which in this case are the respiratory surrogate signals. This technique<sup>51</sup> is used widely in industrial applications with a high degree of predictive value. It is not immediately clear why high specificity cannot be achieved along with high sensitivity in this application.

The purpose of this study was *to develop a better understanding of mechanisms underlying the performance of a respiratory surrogate-based monitoring technique for maintaining real-time tumor localization model accuracy*. Through increasingly complex respiratory surrogate and tumor motion simulations, we evaluated measurement precision, period variations, amplitude variations, gross patient motion, and end-exhale position variations as possible phenomena contributing to poor specificity in this monitoring technique. We confirmed these results in data from 5 lung cancer patients who underwent a total of 13 magnetic resonance imaging sessions.

## 9.2. Methods

### 9.2.1. Patient Data

#### 9.2.1.1. Dynamic Magnetic Resonance Imaging

Five lung cancer patients undergoing radiation therapy at the University of Maryland Medical Center Department of Radiation Oncology underwent magnetic resonance (MR) imaging as part of an ongoing Institutional Review Board-approved study. The scans took place during three stages of the participants' radiation therapy treatments. The first scan took place 1-2 weeks prior to the start of the treatments. For patients undergoing conventionally fractionated radiation therapy, a second scan took place between the 5<sup>th</sup> and 11<sup>th</sup> treatments and a third scan took place between the 15<sup>th</sup> and 21<sup>th</sup> treatments. For patients undergoing hypo-fractionated radiation therapy, a second scan took place between the 1<sup>st</sup> and 2<sup>nd</sup> treatments, and a third scan took place between the 2<sup>nd</sup> and last treatments. One of the five patient-volunteers completed only the first imaging session, and the other four completed all the three imaging sessions.

Images of the tumor were acquired on a 1.5 T MR imager (Manetom Avanto, Siemens, Erlangen, Germany) using a TrueFISP sequence (200 images, 5 sagittal slices, 8 mm slice thickness, interleaved acquisition, TE 1.29 ms, TR 2.57 ms, 60° flip angle, matrix 176 × 256 matrix, in-plane spatial resolution of 1.6-2.2 mm in each direction, 1028 bandwidth, 500 s total acquisition time). The field of view was selected to encompass the thorax and was centered at the tumor position in the medial-lateral dimension.

The slice of the imaging volume passing through the approximate center of the tumor was utilized to localize the tumor in the anterior-posterior (AP) and the superior inferior (SI) directions. This image slice was acquired once every 2.5 s, and 200 frames were captured in each scan session. The tumor was localized in each frame by finding the centroid of a bounding box around the tumor (**Figure 9.1**).

In addition to drawing the box circumscribing the tumor, the tumor was also contoured in one image set by three individuals. The centroid of the contour was compared to the centroid of the box in each frame. The difference between contour centroid position and box centroid position was of the same magnitude as inter-observer contouring variation in the same dataset.



**Figure 9.1.** Tumor localization (box) in a sagittal slice through the tumor.

#### 9.2.1.2. Respiratory Surrogate Measurements Captured During Imaging

Prior to each scan, five spherical reflective markers were affixed to the abdomen in an arc configuration about the umbilicus. The reflective markers were tracked by a stereoscopic infrared camera system (Polaris Spectra, NDI, Waterloo, Ontario). The camera system (**Figure 9.2**) calculates the position of each marker in three dimensions from concurrent images captured through two lenses.



**Figure 9.2.** Stereoscopic camera system in position at the MR scanner.



The respiratory surrogate marker positions were logged by in-house-developed software (Labview, National Instruments, Austin, Texas). The software polled the camera system for 3D marker positions at a rate of 30 Hz, parsed the camera system's response, and logged the 5 marker positions. Simultaneously, the software sent voltage pulses through a DT9800 USB Function Module for Data Acquisition (Data Translation, Marlboro, MA). The 100-ms pulses were initiated every 500 ms and were sent to the scanner through its electrocardiogram input hardware. The scanner was programmed to acquire one image slice per pulse. In addition, to synchronize the computer with the scanner, the software began polling the camera system for marker positions as the first voltage pulse was initiated.

The camera system utilized in this study sometimes reports more positions than there are markers. This is an artifact of the system's image analysis software, which is unable to correctly localize all of the markers when any two markers are coplanar with the two camera lenses (**Figure 9.3**). Instead, two "phantom" marker positions are reported in addition to the positions of the two real markers. Because of the arrangement of the markers inside the scanner bore and the position of the camera near the subject's feet, the phantom markers were always significantly superior and inferior, respectively, to the set of real markers. Thus, the phantom markers were easily identified by plotting all marker data in an imaging session and drawing a box around the real markers (**Figure 9.4**). The phantom markers were excluded from subsequent analyses.

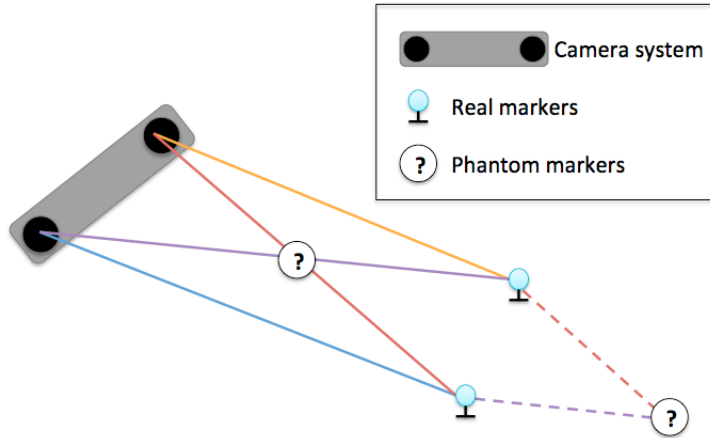
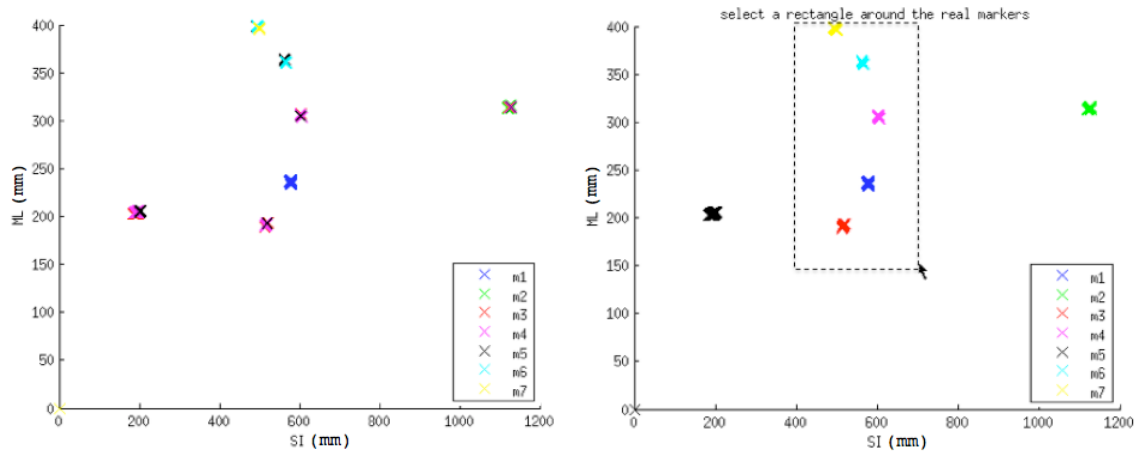
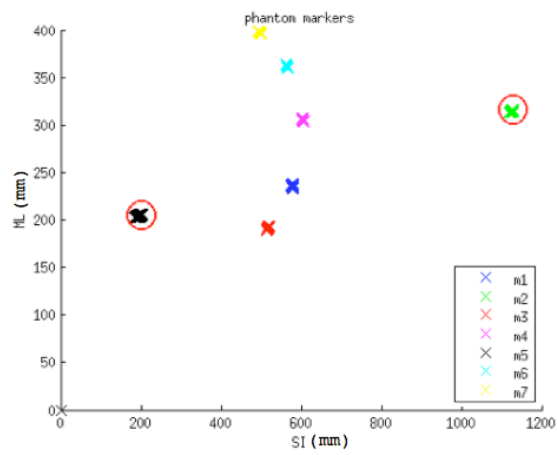


**Figure 9.3.** Phantom marker artifact of the stereoscopic camera system. The system is unable to distinguish between the real and phantom markers when two real markers are coplanar with the two camera lenses. The dashed purple and red lines are parallel to the solid purple and red lines, respectively, and the phantom marker positions are reported at the intersections of the purple and red lines.



(a)

(b)



(c)

**Figure 9.4.** Respiratory surrogate marker data processing for patient #1 imaging session #1. (a) Unsorted surrogate marker data. (b) Surrogate marker data replotted after automated sorting. On this plot, the user selects a box around the data known to be associated with true (non-phantom) marker data. (c) Phantom marker data circled on the sorted marker plot.

The tracking camera's marker localization algorithm does not associate the markers in one set of images with those of another. As a result, the markers' positions are not reported in the same order for every sample (**Figure 9.4**). For this study, the entire marker position dataset for each imaging session was sorted retrospectively using *k*-means clustering. The *k*-means clustering algorithm separates the marker positions into *k* clusters such that the total sum of the distances between each marker position and the associated cluster's centroid is minimized.<sup>84</sup> The algorithm begins with *k* initial points, which for this study were the *k* marker positions reported by the camera at a single sample. One-by-one, each point in each of the other samples was then assigned to the cluster whose centroid was closest to that marker position; the cluster's centroid position was updated as each point was added to the cluster. After assigning each reported marker position to a cluster, the algorithm continues to move points between clusters until the sum of the distances cannot be decreased further. The success of the *k*-means clustering was confirmed by visual inspection and by counting the missing samples for each marker. To account for setup errors in 2 of the 13 imaging sessions, marker datasets in which more than 1% of points were missing were not used to predict tumor displacement.

After sorting, the mean-centered surrogate marker positions were orthogonally projected onto a line calculated from each surrogate marker's positions recorded during the training data period. The line passed through the origin, and its direction was given by the first principal component of the marker position matrix. The first principal component vector was given by the first eigenvector of the data's covariance matrix. Each projected

surrogate marker position was defined as the distance from the position of the projected point on the line to the origin.

Each tumor position was determined from an image slice that was acquired over the course of 450 ms. Thus, for patient data, 15 surrogate marker positions were captured during each image acquisition period. The projected respiratory surrogate positions corresponding to each image slice, therefore, were taken as the average of the 15 values captured during the slice acquisition period.

## 9.2.2. Respiratory Surrogate Models of Tumor Displacement

### 9.2.2.1. Training Datasets

Respiratory surrogate models can be created from a “training” dataset of concurrent tumor and respiratory surrogate marker positions. Training datasets were created from the first 30 sec of the 500 sec-long datasets. In the patient data, training datasets were created at 0.4 Hz (the maximum possible frequency for the images captured 2.5 sec apart) and at a 0.1 Hz rate. In simulations, training datasets were created at sampling rates of 0.1 Hz to 30 Hz.

### 9.2.2.2. Partial Least Squares (PLS) Regression

For each imaging session, partial least squares (PLS) regression was used to fit linear, multivariate models that estimate tumor position from respiratory surrogate marker data as described in Section 2.6.2. The model was applied to a testing dataset consisting of the subsequent respiratory surrogate marker data in the imaging session. For patients, the

testing data was sampled at 0.4 Hz. For simulations, the testing data was sampled at 30 Hz. Tumor positions were predicted from respiratory surrogate measurements at these testing points to determine tumor localization errors. Errors reported are the Euclidean distance between the two-dimensional true tumor position (MR image-measured tumor position or simulated tumor position) and the two-dimensional position predicted by the model.

### 9.2.3. Monitoring Respiratory Surrogate Models of Tumor Displacement

#### 9.2.3.1. Control Limits for Monitoring Respiratory Surrogate Models

Control limits on Hotelling's  $T^2$  statistic and the input variable squared prediction error,  $Q^{(X)}$ , were created for each model as described in Section 2.8. The  $T^2$  and  $Q^{(X)}$  values were determined for each data point in the testing dataset. When either  $T^2$  or  $Q^{(X)}$  exceeded the control limits determined from  $T^2$  or  $Q^{(X)}$  values in the training dataset, errors were predicted to be large.

#### 9.2.3.2. Performance of the Monitoring Technique

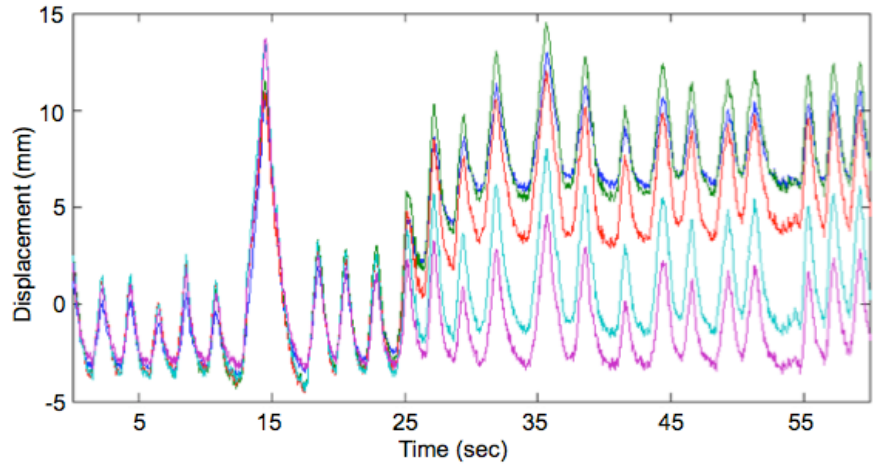
Performance of the monitoring technique can be measured as the sensitivity and the specificity in detecting errors greater than 3 mm. Sensitivity was given by the number of errors correctly predicted to be greater than 3 mm divided by the total number of errors that were actually greater than 3 mm. Specificity was given by the number of errors correctly predicted to be less than 3 mm divided by the total number of errors that were actually less than 3 mm.

Control limits on  $T^2$  and  $Q^{(X)}$  were 99.9<sup>th</sup> percentile expected values of  $T^2$  and  $Q^{(X)}$  except where otherwise noted. In these exceptions, the control limits were selected retrospectively such that the sensitivity for predicting errors greater than 3 mm was 95%. To find the control limit resulting in 95% sensitivity, the sensitivity was determined for a variety of control limits. The optimal control limit for 95% sensitivity was determined iteratively. Because sensitivity and specificity are dependent upon one another, keeping sensitivity constant makes it possible to directly compare monitoring performances through a single variable: specificity.

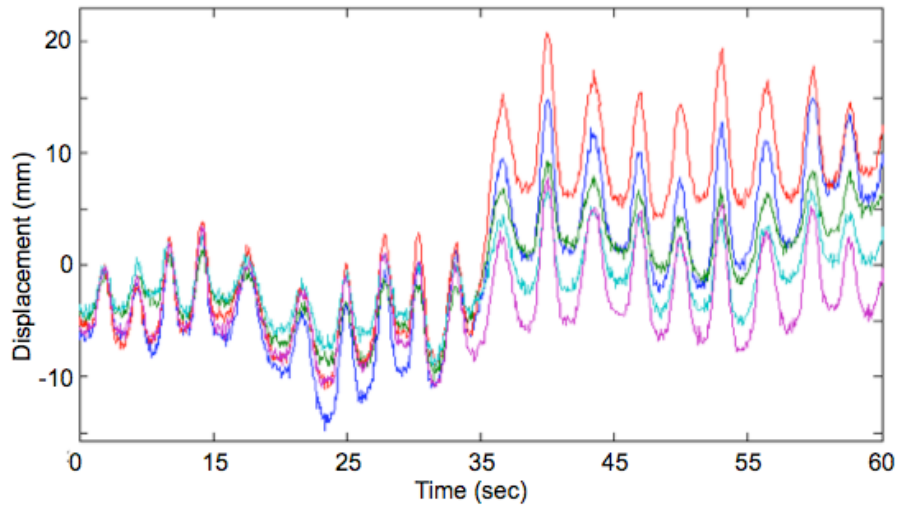
#### 9.2.4. Simulations

A series of simulations were performed in order to form an understanding of the results in the patient data. For each simulation dataset, two-dimensional tumor motion and the three-dimensional motion paths of each of 5 respiratory surrogate markers affixed to the torso were simulated. Like the patient datasets, simulated datasets were 500 sec in duration. Except where otherwise noted, the simulated data was sampled at 30 Hz.

Seppenwoolde *et al.* showed that most tumors move through space in a pattern that most closely resembles a cosine to the fourth power curve.<sup>47</sup> Upon evaluation of the patient data collected for this study, it was apparent that the respiratory surrogate signals were also shaped like cosine to the fourth power curves (**Figure 9.5**). Each breath was simulated as one period of a cosine to the fourth curve for both the respiratory surrogate marker motion and the tumor motion.



(a)



(b)

**Figure 9.5.** The five respiratory surrogate marker datasets projected onto one dimension in (a) a patient dataset showing gross patient motion, amplitude variations, period variations, and measurement noise but no baseline variations, and (b) a simulated dataset incorporating all sources of variation.



In each set of simulations, respiratory surrogate signals ( $X$ ) and tumor motion ( $Y$ ) for individual respiratory cycles were simulated as follows:

$$X_{i,SI} = (6 \cdot R_{i,SI} + 4) \cdot A(t) \cdot \cos^4\left(\frac{\pi}{T(t)} \cdot t\right) + M_{i,SI}(t) + G_{i,SI}(t) + E_{i,SI}(t) \quad (1)$$

$$X_{i,AP} = (3 \cdot R_{i,AP}) \cdot A(t) \cdot \cos^4\left(\frac{\pi}{T(t)} \cdot t\right) + M_{i,AP}(t) + G_{i,AP}(t) + E_{i,AP}(t) \quad (2)$$

$$X_{i,ML} = (3 \cdot R_{i,ML}) \cdot A(t) \cdot \cos^4\left(\frac{\pi}{T(t)} \cdot t\right) + M_{i,ML}(t) + G_{i,ML}(t) + E_{i,ML}(t) \quad (3)$$

$$Y_{SI} = 10 \cdot A(t) \cdot \cos^4\left(\frac{\pi}{T(t)} \cdot t\right) + M_{0,SI} + G_{0,SI} + D_{SI} \quad (4)$$

$$Y_{AP} = 5 \cdot A(t) \cdot \cos^4\left(\frac{\pi}{T(t)} \cdot t\right) + M_{0,AP} + G_{0,AP} + D_{AP} \quad (5)$$

where  $X_{i,j}$  represents the  $j$  dimension of the motion of respiratory surrogate marker  $i$ ,  $Y_k$  represents the  $k$  dimension of tumor motion,  $T(t)$  is a function describing the periods of each respiratory cycle, and  $A(t)$  is a function that scales the data associated with each respiratory cycle by a constant value.  $M_{i,j}(t)$ ,  $G_{i,j}(t)$ ,  $E_{i,j}(t)$ , and  $D_j(t)$  are functions simulating measurement error, gross patient motion, respiratory surrogate marker end-exhale position variations, and tumor drift, respectively. These functions will be defined in later sections. In each simulation, unless otherwise noted,  $A_{i,j} = 1$  mm,  $T = 3.3$  sec,  $M_{i,j}(t) = 0$  mm,  $G_{i,j}(t) = 0$  mm,  $E_{i,j}(t) = 0$  mm, and  $D_j(t) = 0$  mm.  $X_{i,SI}$  was designed to be larger in magnitude than  $X_{i,AP}$  and  $X_{i,ML}$  to match the patient data (**Table 9.1**). Directions of motion are given in patient coordinates: superior-inferior (SI), anterior-posterior (AP), and medial-lateral (ML). 100 datasets were simulated for each experiment.

**Table 9.1.** Respiratory cycle measurements for a randomly selected surrogate marker in the first imaging session for each patient

Patient ID	Magnitude of surrogate marker motion (mm)			Magnitude of surrogate marker motion (mm)			Mean period (sec)	St. dev period (sec)
	SI	ML	AP	SI	ML	AP		
1	8.7	2.1	1.9	1.3	0.4	0.3	3.4	0.3
2	6.0	2.0	3.0	2.2	0.6	1.3	3.2	1.1
3	5.3	1.3	2.4	1.1	0.2	0.4	3.6	0.4
4	4.0	2.5	2.8	1.0	0.7	0.7	3.4	0.6
5	5.1	0.8	1.3	0.7	0.2	0.2	2.7	0.4
Average	5.8	1.7	2.3	1.3	0.4	0.6	3.3	0.6

#### 9.2.4.1. Basic Simulations

To establish a baseline of performance for a simple simulation dataset, the modeling and monitoring techniques were tested for the default values of  $A_{i,j} = 1$  mm,  $T = 3.3$  sec,  $M_{i,j}(t) = 0$  mm,  $G_{i,j}(t) = 0$  mm,  $E_{i,j}(t) = 0$  mm, and  $D_j(t) = 0$  mm.

#### 9.2.4.2. Variations in Waveform Period and Amplitude

To simulate breath-to-breath variations in the respiratory surrogate and tumor motion data, the five datasets described by Equations 1-5 were generated one respiratory cycle at a time. Periods and amplitudes were constant over individual respiratory cycles such that  $T(t) = T_n$  and  $A(t) = A_n$  for  $t$  from the beginning to the end of respiratory cycle  $n$ . Because the mean  $\pm$  standard deviation period of the respiratory cycles in the patient dataset was  $3.3 \text{ sec} \pm 0.6 \text{ sec}$  (Table I), the period for each respiratory cycle of index  $n$  was calculated as  $T_n = 3.3 + 0.6 \cdot r_T$  sec, where  $r_T$  was a random variable with a normal distribution and a standard deviation of 1 sec. Similarly, each amplitude scaling factor was calculated as  $A_n = 1 + 0.25 \cdot r_A$ , where  $r_A$  was random variable with a normal distribution and a standard deviation of 1. The factor of 0.25 in this expression was included so that the amplitude variations would match the average ratio of the standard deviation of surrogate marker magnitude to the mean surrogate marker magnitude in each direction (**Table 9.1**).

#### 9.2.4.3. Measurement Noise

To evaluate the effect of finite precision in the respiratory surrogate signals and in the image-based tumor localizations, random noise was added to the equations in the form of

$M_{i,j}(t)$ . The values at each sample were calculated as  $M_{i,j} = \frac{r_M}{3}$  for respiratory surrogate  $i$  and  $M_{i,k} = r_M$  for tumor motion, where  $r_M$  was a normally distributed random variable with a standard deviation of 1 mm. Noise of a standard deviation of 0.3 mm in the respiratory surrogate measurements approximates the errors in the patient dataset (Figure 1). The magnitude of the noise in the tumor positions, with a standard deviation of 1 mm, was approximately equal to the inter-observer variability for localizing the tumor in the MR images.

#### 9.2.4.4. Gross Patient Motion

Gross patient motion caused by conscious muscle movements or gradual muscle relaxation is apparent in patient datasets in which there are concurrent baseline shifts in respiratory surrogate signals and tumor motion traces. This type of event was simulated by adding a logistic curve defined as  $G_{i,j} = \frac{5 \cdot r_{G,i}}{1 + e^{-(t-250)}}$  to the respiratory surrogate marker signals, where  $r_{G,j}$  was a random variable with a uniform distribution on the open interval from 0 to 1, and by adding  $G_{0,k} = \frac{3 \cdot (-1)^k}{1 + e^{-(t-250)}}$  to the tumor motion traces.

#### 9.2.4.5. End-Exhale Variations

While the end-exhale respiratory surrogate marker position tends to be more stable than the end-inhale position, the end-exhale position is not constant.<sup>6</sup> To simulate realistic end-exhale variations, the end-exhale positions from a patient dataset were duplicated in the simulated datasets. For each simulated respiratory cycle,

$$E_{i,j}(t) = \frac{x_{i,n+1} - x_{i,n}}{t(T_n + t_0) - t(t_0)} \cdot t + x_{i,n}, \text{ where } x_{i,n} \text{ is the position of } i \text{ at end-exhale for respiratory}$$

cycle number  $n$ ,  $t(t_0)$  is the time at the start of simulated respiratory cycle number  $n$ , and  $T_n$  is the period of simulated respiratory cycle number  $n$ . The resulting dataset incorporates end-exhale variations without creating discontinuities in the signals (**Figure 9.5**). The end-exhale positions were based on a patient dataset that had a gradual drift in the end-exhale positions but did not include any sudden, large baseline shifts like those simulated in Section 9.2.4.4.

#### 9.2.4.6. Drift in Tumor Position

In the patient data, gradual drifts in tumor position occurred independently from drifts in respiratory surrogate signals. Consequently, tumor position drifts were simulated independently from respiratory surrogate signal variations. Gradual drifts in tumor position were simulated as a linear 1-2 millimeter drift in each direction of tumor motion over the 500 sec simulated. Specifically,  $D_{SI}(t) = -0.004 \cdot t$  and  $D_{AP}(t) = 0.002 \cdot t$ .

#### 9.2.4.7. Intermittent Sampling

Datasets incorporating all of the sources of variation described above (period variations, amplitude variations, measurement errors, respiratory surrogate end-exhale variations, tumor drift, and gross patient motion) were developed. In these simulations, tumor drift, gross patient motion, and end-exhale variations were included in datasets at a probability of 23%, 23%, and 46%, respectively, to match the incidences observed in patient data. Results were calculated for training datasets 30 sec in duration and with sampling rates of

0.1 Hz, 0.4 Hz, 1 Hz, and 15 Hz to simulate tumor localization rates possible in various imaging systems.

#### 9.2.4.8. Averaging Across Acquisition Periods

In the patient dataset, the tumor localizations were acquired in images captured over a period of 0.45 sec. During that time, 13 respiratory surrogate marker position samples were captured. Therefore, to match tumor positions with respiratory surrogate marker positions, it was necessary to average the higher frequency surrogate marker data over the image acquisition period. The intermittent sampling simulations (Section 9.2.4.7) at 0.1 Hz, 0.4 Hz, and 1 Hz were repeated with the additional averaging step applied such that each surrogate marker position and each tumor position were calculated as the average of data captured over 0.45 sec.

### 9.3. Results

#### 9.3.1. Imaging Study Results

##### 9.3.1.1. Surrogate Marker Tracking

Because of setup errors involving the positions of the markers on the abdomen and the arrangement of the patients' clothing, the camera failed to reliably track a few surrogate markers during the course of the study. One surrogate marker from one imaging session and two surrogate markers from a second imaging session were excluded from the analyses for this reason. In these two imaging sessions, tumor localization models were based upon 3 and 4 of the surrogate markers, respectively.

#### 9.3.1.2. Motion Patterns

Amplitude variations, period variations, and measurement noise were present in all 13 imaging sessions. While end-exhale variations were observed in every respiratory surrogate dataset, end-exhale variations greater than 2 mm were less common. Gradual drifts of at least 2 mm in the end-exhale positions, like those simulated in Section 9.3.2.5, were present in 6 of the 13 respiratory surrogate datasets. Rapid shifts of at least 2 mm within 10 sec, such as those simulated in Section 9.2.4.4, were visible in 3 of the 13 respiratory surrogate datasets.

In low-pass filtered image-based tumor localization data, gradual baseline shifts of at least 2 mm, like those simulated in Section 9.2.4.6, were present in 3 of the 13 datasets. No rapid (<10 sec) 2 mm shifts were visible in any of the 0.4 Hz tumor localizations datasets.

#### 9.3.1.3. Tumor Localization Model and Monitoring

Although respiratory surrogate model-predicted tumor localizations were validated at 0.4 Hz, applying the PLS model of tumor motion to individual respiratory surrogate marker positions yielded realistic tumor motion curves (**Figure 9.6**). For 0.4 Hz and 0.1 Hz training datasets, the mean  $\pm$  standard deviation PLS model tumor localization errors in the testing data were 1.5 mm  $\pm$  1.0 mm and 1.9 mm  $\pm$  1.7 mm, respectively (**Table 9.2**). Given a sensitivity of 95%, the specificities for detection of errors greater than 3 mm were 8% for the 0.4 Hz training data and 17% for the 0.1 Hz training data.

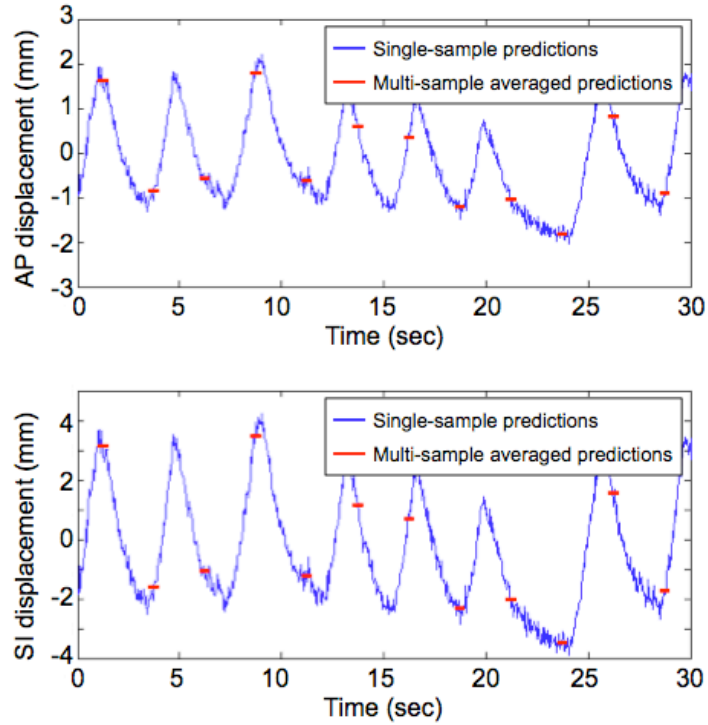


**Figure 9.6.** Tumor localizations (predictions) based on either a single set of respiratory surrogate marker positions (continuous blue lines) or the average of respiratory surrogate marker positions recorded over the course of 450 msec (450-msec-long red horizontal lines).

**Table 9.2.** Modeling and model monitoring performance for patient datasets

Training data sampling rate (Hz)	Mean error (mm)	St. dev. error (mm)	Sensitivity	Specificity
0.4	1.5	1.0	95%	8%
0.1	1.9	1.7	95%	17%



### 9.3.2. Simulation Study Results

#### 9.3.2.1. Baseline Simulation Results

For the baseline simulations in which no sources of variation were included, all tumor localization errors were less than 0.1 mm. Specificity was 100% (no large errors were predicted by the monitoring technique), and sensitivity could not be quantified, because no errors exceeded 3 mm.

#### 9.3.2.2. Variations in Waveform Period and Amplitude

The respiratory surrogate models were able to predict tumor displacement to within less than 0.1 mm at every sample when simulated data included period variations, amplitude variations, or a combination thereof. Specificity was 100%, and sensitivity could not be quantified, because no errors exceeded 3 mm.

#### 9.3.2.3. Measurement Precision Limitations

When measurement errors were simulated in the form of noise added to the respiratory surrogate signals and tumor positions, the tumor localization errors increased. For the simulated magnitude of measurement precision errors, tumor localization errors (mean  $\pm$  standard deviation) increased to 1.3 mm  $\pm$  0.0 mm, and only 1% of errors exceeded 3 mm. Specificity was 99% and sensitivity was 1%.

To induce large errors and in order to better understand the effect of measurement noise, results were also determined for a case in which the measurement noise was tripled in each direction. With measurement noise of this magnitude, 39% of errors exceeded 3

mm. For this hypothetical larger measurement noise, the tumor localization error increased to  $3.8 \text{ mm} \pm 2.0 \text{ mm}$ , and sensitivity and specificity were 0% and 100%, respectively.

#### 9.3.2.4. Gross Patient Motion

When gross patient motion was simulated, the mean  $\pm$  standard deviation of tumor localization errors was  $5.5 \text{ mm} \pm 2.8 \text{ mm}$ . The sensitivity and specificity were 100% and 83%, respectively. The specificity was 100% except during the transition period when the shift was in progress.

#### 9.3.2.5. End-Exhale Variations

As compared to the baseline simulations, varying the position of the respiratory surrogate markers at end-exhale had the effect of increasing tumor localization error while decreasing both sensitivity and specificity. The mean  $\pm$  standard deviation error was  $5.1 \text{ mm} \pm 2.3 \text{ mm}$ , sensitivity was 89%, and specificity was 90%.

#### 9.3.2.6. Drift in Tumor Position

As compared to baseline simulations, applying a drift in the tumor motion had the effect of increasing the tumor localization error to  $2.2 \text{ mm} \pm 1.2 \text{ mm}$ . No errors exceeded 3 mm, so sensitivity could not be measured, and specificity was 100%.

In order to better understand the effect of tumor position drift, results were also determined for a case in which the tumor position drift was tripled in each direction. For this hypothetical larger tumor drift, while 79% of errors exceeded 3 mm, no large errors

were detected by the monitoring technique. Sensitivity and specificity were 0% and 100%, respectively.

#### 9.3.2.7. Intermittent Sampling

For simulations including phase variations, amplitude variations, end-exhale variations, phase offsets, measurement errors, and gross patient motion, results for 0.1 Hz to 30 Hz training data sampling rates and 95% sensitivity are given in (**Table 9.3**). With the exception of 30 Hz, specificity increased from 36% to 64% as training data sampling rate increased from 0.1 Hz to 15 Hz. Specificity for 30 Hz sampling was 57%. Tumor localization error did not vary significantly with training data sampling rate.

#### 9.3.2.8. Averaging Across Acquisition Periods

The effect of averaging over the acquisition period varied with training data sample frequency (**Table 9.4**). For 0.1 Hz, 0.4 Hz, and 1 Hz, the specificities were 38%, 60%, and 62%, respectively.

**Table 9.3.** The effect of sampling rate on modeling and model monitoring performance for simulations incorporating all sources of cycle-to-cycle variation

Training data sampling rate (Hz)	Control limits	Mean error (mm)	St. dev. error (mm)	Sensitivity	Specificity
30	79%	4.3	3.4	95%	57%
15	85%	4.3	3.2	95%	64%
1	89%	4.4	3.5	95%	53%
0.4	94.5%	4.3	3.4	95%	41%
0.1	95%	4.4	3.3	95%	36%

**Table 9.4.** Modeling and model monitoring performance for acquisition-time averaged training data

Training data sampling rate (Hz)	Control limits	Mean error (mm)	St. dev. error (mm)	Sensitivity	Specificity
1	85%	4.3	3.7	95%	62%
0.4	85.3%	3.9	3.3	95%	60%
0.1	95%	4.3	4.1	95%	38%

#### 9.4. Discussion

In this work, we have evaluated the effects of measurement errors, period variations, amplitude variations, end-exhale variations, tumor drift, and gross patient motion on the performance of a control limit-based respiratory surrogate model monitoring technique. Respiratory cycle amplitude and period variations had no effect on monitoring performance. With measurement noise or tumor drifts alone, specificities were 99-100% and sensitivities were 0-1%. Gross patient motion was detected with sensitivity of 100% and specificity of 97%. For end-exhale variations, sensitivity was 97%, and specificity was 57%. In simulations that incorporated all sources of signal variations, specificity increased monotonically from 33% at 0.1 Hz to 69% at 30 Hz when sensitivity was 95%. In the patient data, specificity also increased with sampling rate, but the magnitude of the specificities were lower (8% and 17% for 0.1 Hz and 0.4 Hz, respectively) than the specificities in the simulations.

The period and amplitude variations did not impact the tumor localization errors and therefore were not relevant to the control limit monitoring technique. Tumor localization errors increased when variations were not consistent between input and output signals. For instance, end-exhale variations in the respiratory surrogate signals could lead to large errors, which were detected with sensitivity of 97% and specificity of 57%. At the other end of the spectrum, measurement noise-induced errors and tumor drift went undetected, because they were not associated with changes in respiratory marker signal patterns.

When designing training datasets for tumor displacement models, it is tempting to draw upon common engineering techniques such as the Nyquist-Shannon sampling theorem, which specifies a minimum sampling rate for reconstructing a signal. However, for this application there is no need to reconstruct the analog signals. Instead, the sampling rate need only be high enough to fully characterize the relationship between tumor motion and respiratory surrogate signals. In this study, we found no significant difference in tumor localization errors for 30-sec training datasets sampled at 30 Hz to 0.4 Hz. However, the control-limit-based monitoring performance varied considerably across this range of frequencies; there were half as many false alarms in the prediction of large tumor localization errors at the highest sampling rate, 30 Hz, as compared to the lowest sampling rate, 0.1 Hz.

The tumor localizations in this study were based on dynamic MR data captured at 0.4 Hz. In future work, we plan to collect dynamic MR data at 2 Hz by reducing the acquisition volume from 5 slices to 1. It may also be possible to localize the tumor at a rate of up to 15 Hz using x-ray fluoroscopy, but the poor soft tissue contrast of fluoroscopic imaging may preclude its use without first implanting radio-opaque markers in the tumor, a procedure that results in pneumothorax in as many as 38% of patients.<sup>85</sup> Still, fluoroscopic imaging may be more practical in the application of these techniques, because modern radiation treatment machines are equipped with x-ray imaging systems.

In this study, sagittal image slices were analyzed such that superior-inferior (SI) and anterior-posterior (AP) tumor motion could be measured. Depending on the tumor geometry in each patient-volunteer, it is possible that the tumor position in the sagittal

slice is not a perfect representation of the instantaneous SI and AP displacement of the tumor centroid. This effect is likely to be small, because out-of-plane motion through the imaging slice would be in the medial-lateral (ML) direction, which is rarely larger in magnitude than a few millimeters, which was smaller than the spacing between slices.<sup>47</sup>

Every effort was made to ensure that the simulation datasets were representative of patient data. The distribution of measurement errors, period variations, and amplitude variations was equal to that measured in the patient population. Gross patient motion, end-exhale variations, and tumor drift were each based upon a single imaging session and were simulated at the incidence (probabilities of 0.23, 0.46, and 0.23, respectively) seen in the patient data. The averaging inherent in MR data in which images are acquired over 450 msec was simulated as well. The averaging step had little if any effect on either tumor localization accuracy or monitoring method performance.

The simulation results were qualitatively in agreement with the patient data. However, specificities simulations that incorporated all types of cycle-to-cycle variations were larger than those in the patient data. This may have been a consequence of the timing of respiratory cycle variations. For instance, the simulated gross patient motion was modeled halfway through the 500-sec simulations, and the gross patient motion sometimes happened later in the imaging sessions. The gross patient motion had the effect of increasing the error detection specificity for the session as a whole and would have increased the specificity in the simulation datasets.

Tachibana *et al.* have also described a technique for detecting surrogate-based tumor localization errors from optically tracked markers.<sup>86</sup> They have created a system

that optically tracks a marker affixed to the chest for the sole purpose of detecting baseline position shifts of the chest wall. In the surrogate data control limit technique that we have explored in this study, baseline shifts in surrogate marker motion are not identified. However, gross patient motion is detected consistently; the technique identifies large errors associated with baseline shifts with 100% sensitivity and 97% specificity.

This study illuminates the reasons underlying poor specificity in this respiratory surrogate model monitoring technique. Because measurement precision is a factor, some improvement can be expected by improving the signal-to-noise ratio in either the respiratory surrogate measurements or the tumor localizations. Both measurement errors and variations in the end-exhale respiratory surrogate positions, which may not be associated with corresponding tumor position variations, can trigger false alarms. For this reason, it is important to look for trends in the  $T^2$  and  $Q^{(X)}$  statistics. As described in Chapter 7, specificity for identifying large tumor localization errors can be improved by evaluating all respiratory surrogate data captured over the past 1-3 sec rather than using a single set of respiratory surrogate measurements. Unfortunately, it may not be possible to detect tumor drifts caused by internal tissue settling using respiratory surrogates alone.

## 9.5. Conclusions

Control-limit-based monitoring was successful during gross patient motion and end-exhale variations but not with tumor drifts or errors induced by measurement noise. Period and amplitude variations occurring concurrently in tumor and respiratory surrogate signals did not affect errors or monitoring performance. The specificity of the



monitoring technique increased with increasing training dataset tumor localization rate. Simulation results were in qualitative agreement with patient results.

## CHAPTER 10: Conclusions

### 10.1. Main Objective

We have completed the main objective of this dissertation by developing novel techniques for modeling respiration-induced tumor motion from external surrogate measurements of respiration. Two patents are pending on these techniques.

#### Patent Applications:

1. D'Souza, W.D., Zhang, H.H., and **Malinowski, K.T.** Techniques for compensating movement of a treatment target in a patient. US Patent Application 13/172,010, filed June 2011. Patent Pending.
2. D'Souza, W.D., **Malinowski, K.T.**, and McAvoy, T.J. A method for monitoring the accuracy of tissue motion prediction from surrogates. U.S. Provisional Patent Application 61/506,667, filed July 2011. Patent Pending.

The following specific objectives were addressed in this dissertation:

### 10.1.1. Specific Objective #1: Identify Sources of Error in Multivariate Respiratory Surrogate Tumor Localization Models

For tumors that move with respiration, there is a body of literature describing and benchmarking individual algorithms for predicting tumor displacement from respiratory surrogate signals. However, each study describes an algorithm's performance under a specific set of conditions, and no study performed outside of this dissertation work has systematically identified factors that contribute to the accuracy of respiratory surrogate models of tumor motion.

#### Factors contributing to surrogate model accuracy include:

1. Variations between individual patients
2. Tumor position measurement precision
3. Respiratory surrogate signal measurement precision
4. Correlation between tumor motion and surrogate signals
5. Modeling algorithm design (investigated further in Specific Objective #2)
6. Training data timing (investigated further in Specific Objective #3)

The factor that most impacted respiratory surrogate model accuracy was timing. Tumor localization errors 20 minutes after the training data were collected were twice as large as errors captured during the first 2 minutes after the training data were collected. The precise effect of timing varies from one individual to the next. However, within 30 min, the typical length of time that a patient spends in a radiation treatment room for a

single radiotherapy session, surrogate model accuracy degrades significantly in over 60% of patients.

#### 10.1.2. Specific Objective #2: Develop and Validate an Algorithm for Predicting Tumor Position from Multiple Surrogates of Respiration

In order to develop an algorithm for predicting tumor displacement from multiple surrogates of respiration, a series of multivariate regression techniques were evaluated for this application. To our knowledge, our group was the first to apply partial least squares (PLS) regression to the problem of tumor motion modeling. We evaluated our PLS models of tumor motion under a variety of conditions and benchmarked PLS against other regression techniques such as ordinary least squares (OLS) regression. PLS was more accurate for tumor tracking than OLS. In general, OLS regression has a tendency to over-fit the training data at the expense of prediction accuracy. PLS was more effective, because its compression step generates latent variables from the original set of respiratory surrogate signal inputs in a way that combines correlated signals and separates out the input variance that is not correlated with tumor variance.

The accuracy of the PLS regression models was improved by projecting each three-dimensional respiratory surrogate motion dataset onto a single dimension before regressing on the data. The projection step increased the correlation between surrogate-based inputs and tumor motion by increasing the signal to noise ratio in the surrogates.

##### Final tumor localization algorithm:

1. Capture images of the tumor while collecting respiratory surrogate data.

2. Localize the tumor in each image to obtain a set of tumor positions ( $Y$ ).
3. Orthogonally project the three-dimensional respiratory surrogate motion onto the line defined by the data's first principal component to obtain respiratory surrogate signals ( $X$ ).
4. Apply PLS to calculate a multivariate regression model ( $Y = X \cdot B$  with regression coefficient matrix  $B$ ) defining tumor displacement as a function of respiratory surrogate marker signals.
5. Apply the regression model to new surrogate marker data to predict tumor displacements without capturing additional images of the tumor.

Although the main focus of this work was real-time tumor displacement prediction, we were able to apply this technique successfully in a second radiation therapy application. 4D CT data is often collected prior to radiation treatment in order to obtain an estimate of the range of tumor motion during free breathing. However, the labor-intensive and time-consuming nature of analyzing the multiple (usually 8-12) volumetric images in a 4D CT dataset precludes many clinics from utilizing 4D CT data. We proposed and validated a technique in which manually contouring all ten of the image datasets could be avoided by instead combining three manually contoured image sets with the easily identified positions of anatomical surrogates of respiration such as the carina. The net effect of this technique was that analyzing 4D CT datasets could be completed more quickly, making it possible for more patients to have access to 4D CT technology. The surrogate model-predicted tumor centroid position matched the contour-

based centroid position to within an average error of 1 mm in each direction, a magnitude within the contouring certainty of the CT images.<sup>87</sup>

### 10.1.3. Specific Objective #3: Develop and Validate Methods of Monitoring Changes in Respiratory Surrogate Model Accuracy

The main factor precluding clinicians from utilizing respiratory surrogate models of tumor motion is a lack of confidence in the models themselves. In current clinical practice, the variations in tumor position are estimated prospectively in order to develop a treatment plan that balances the risk to healthy tissues with the goal of tumor control. Hypothetically, devices that adjust treatment according to the instantaneous tumor position can deliver radiation to a smaller volume to spare the healthy tissue. However, this more precise treatment can miss the tumor either partially or altogether if the tumor localization is not sufficiently accurate.

We have developed a technique by which the respiratory surrogate model accuracy can be monitored through external (respiratory surrogate) measurements alone, without capturing images of the tumor to directly validate the model. In this technique, control limits are placed on statistical process control metrics that evaluate the relative respiratory surrogate positions and their relationship to the model created at the start of treatment. Using this method, we have been able to achieve high sensitivity (95%) and moderate specificity (8-17%) in patient datasets. The characteristics of the data used to train the model, including image sampling rate and measurement precision, significantly impact the performance of the monitoring technique. It is possible to improve specificity by a factor of 2 to 3 if the training data tumor positions are captured fluoroscopically (30

Hz) rather than through dynamic magnetic resonance imaging (0.4 Hz). Still, in its current form, the method can be used to reduce model update frequency considerably (more than a factor of 2) over clinically available technologies.

Final respiratory surrogate monitoring algorithm:

1. Develop a PLS model ( $Y = X \cdot B$  with regression coefficient matrix  $B$ ) relating three-dimensional respiratory surrogate marker positions ( $X$ ) to three-dimensional tumor positions ( $Y$ ).
2. Calculate  $T^2$  and  $Q^{(X)}$  for each training data sample used to develop the PLS model in (1).
3. Calculate  $\alpha$ -percentile limits on  $T^2$  and  $Q^{(X)}$  for some  $\alpha$  that has been selected to achieve the desired sensitivity for the relevant imaging modality.
4. Calculate  $T^2$  and  $Q^{(X)}$  for each new respiratory surrogate measurement and compare to control limits.
5. When  $T^2$  and  $Q^{(X)}$  exceeds a control limit in the majority of samples collected over 3 sec, develop a new tumor localization model (Section 10.3) with new training data.

## 10.2. Significance and Future Work

The novel techniques for modeling tumor motion and monitoring those models that have been developed in the course of this work are patent-pending. These techniques have the potential to improve patient outcomes by reducing radiation-induced side effects while improving tumor control.

The techniques described here will be incorporated into a product<sup>19,88</sup> at the center of a new startup company, Immoventions Medical. Future work will involve further refining the monitoring technique as well as integrating the technologies described in this dissertation into a tumor motion-compensating patient support system.





## APPENDIX B: Selected Matlab Code

### B.1 parseExternalData

```
% parseExternalData.m
%
% This script parses the MRI study's Polaris Spectra
% log files. Results are saved in a subdirectory.
%
% Kathleen Malinowski
% December 14, 2011

clear
clc
colors = 'bgrmkcybgrmkcy';

% collect external marker file names
DIR = dir('/data/home/kmalinowski/data_MRI/external_motionscans');

% process all external marker files
for filei = 3:length(DIR)
    close all

    % load tracking data
    C = csvread(['/data/home/kmalinowski/data_MRI/external_motionscans/' ...
                DIR(filei).name],5,0);

    % begin to parse filename and data
    external.patientID = str2double(DIR(filei).name(4:5));
    external.sessionID = str2double(DIR(filei).name(13));
    external.t          = C(:,1);
    external.tsec       = (external.t-external.t(1))*1/60;
    external.markeroutofvolume = C(:,2:4:end);
    Xunsrt = C(:,3:4:end); Yunsrt = C(:,4:4:end); Zunsrt = C(:,5:4:end);

    %% apply k-means clustering to sort columns into marker order
    % list all points in an nx3 vector
    allpoints = [];
    for i = 1:size(Xunsrt,2)
        pointsListi = [Xunsrt(:,i) Yunsrt(:,i) Zunsrt(:,i)];
        allpoints   = [allpoints; pointsListi];
    end
    % find a line of data in which there are no failed tracking
    % points to use as a starting point for the cluster analysis
    linei = 1;
    foundline = 0;
    while foundline==0
        if min(abs(Xunsrt(linei,:)))>0
            foundline=1;
        else
            linei = linei+1;
        end
    end
    %initial condition for k-means clustering
    ismissngpts = (min(min(Xunsrt))==0);
    initpts = zeros(ismissngpts,3);
    for i = 1:size(Xunsrt,2)
        initpts(end+1,:) = [Xunsrt(linei,i) Yunsrt(linei,i) Zunsrt(linei,i)];
    end
end
```

```

        numclusters = size(Xunsrt,2)+ismissngpts;
%apply algorithm
        clstri = kmeans(allpoints,numclusters,'start',initpts);

% re-sort the points into a new matrix
        clstriRshp = reshape(clstri,size(Xunsrt,1),size(Xunsrt,2));
        sorted = zeros(size(clstriRshp,1),size(clstriRshp,2)*3);
        for line = 1:size(Xunsrt,1)
            for cluster = (ismissngpts+1):numclusters
                ci = find(clstriRshp(line,:)==cluster);
                if length(ci)==1
                    sorted(line,((cluster-1-ismissngpts)*3+1):((cluster-1-ismissngpts)*3...
                        +3)) = [Xunsrt(line,ci) Yunsrt(line,ci) Zunsrt(line,ci)];
                elseif length(ci)>1
                    %do not record either point. (This error checking code was
                    %added for 1 instance of this error in patient #3 scan #1)
                    fprintf('Warning: point uncategorized (see m-file line 73) ...
                        in patient %i scan %i\n',...
                            external.patientID,external.sessionID);
                end
            end
        end
        mkrX = sorted(:,1:3:end); mkrY = sorted(:,2:3:end); mkrZ = sorted(:,3:3:end);

% find the false markers by selecting the five markers in an arc across the abdomen
        for mkri=1:size(mkrX,2)
            figure(30)
            set(gcf,'Color',[1 1 1]); set(gca,'FontSize',16)
            hold on
            plot(mkrX(:,mkri),mkrY(:,mkri),['x' colors(mkri)],'MarkerSize',10) %top view plot
            hold off
            xlabel('SI'); ylabel('ML')
        end
        title('select a rectangle around the real markers')
        rect = getrect(30);
        false = [find(mkrZ(linei,:)<rect(1)) find(mkrZ(linei,:)>(rect(1)+rect(3)))];

% plot to verify visually
        figure(30)
        hold on
        plot(mkrZ(linei,false),mkrY(linei,false),'or','MarkerSize',20,'LineWidth',2)
        title('phantom markers')
        pause(.5)

        external.realmarkers = setdiff(1:size(mkrX,2),false);
        L = zeros(1,length(external.realmarkers));
        for mkri=external.realmarkers

            % find and count missing datapoints
            datai = setdiff(1:length(mkrX(:,mkri)),find(mkrX(:,mkri)==0));
            L(mkri)=length(datai);
        end

% finish parsing and save processed data
        external.numMarkers = length(markers);
        external.markerX = mkrX(:,markers);
        external.markerY = mkrY(:,markers);
        external.markerZ = mkrZ(:,markers);
        external.markerXdirection = 'SI';
        external.markerYdirection = 'ML';
        external.markerZdirection = 'AP';
        save(['externaldataProcessed/extData_pat' num2str(external.patientID) 'scan' ...
            num2str(external.sessionID)],'external');
        clear external
    end
end

```

end

## B.2 func\_projectData

```
% function [R n m] = func_projectData(X,trainingi)
%
% X: a cell array in which each cell is an nx3
%     matrix of positions.
% training i: a vector of indices from which to
%             calculate the projection line
% n,m: The equation of the line is [x,y,z] = n*t+m
%
% Orthogonally project 3D external surrogate data
% positions onto a single dimension. The projection
% line is in the direction of the first principal
% component of the 3D data and also passes through
% the mean position of the data.
%
% Kathleen Malinowski
% January 2, 2012
%
% (modified from original func_projectData file
% in the SPC follow-up directory)

    for i=1:length(X)
        % projection lines - based on data acquired during training image acquisitions
        [n{i} m{i}] = func_lineFinder(X{i}(trainingi));
        % project external marker positions at image acquisition timepoints
        R{i} = (X{i}-repmat(m{i},size(X{i},1),1))*n{i};
    end
end
```

## B.3 func\_lineFinder

```
function [n m] = func_lineFinder(X)
% Fits a line to an array of datapoints.
% The equation of the line is [x,y,z] = n*t+m
%
% X = NxM array of datapoints
% m = 1xM mean position of input data
% n = Mx1 first principal component defining direction of line
%
% Kathleen Malinowski
% May 30, 2011

    m = mean(X,1);           %mean of input data
    coeff = princomp(X);    %principle components
    n = coeff(:,1);         %unit vector, direction of the line
end
```

## B.4 applyPLSandSPC

```
% applyPLSandSPC.m
%
% Apply statistical process control model monitoring
% methods. SPC results are derived from 3D input data
% and models are built on 1D input data.
%
% Kathleen Malinowski
% June 10, 2011

clear
clc
close all
DIR = dir('data_tumorMotionResults/');

% set parameters
qtyTrainPts = 10;
qtyLV = 4;
maxe = 3;
T2perc = .99; Qperc = .99;

% initialize variables
alldata.T2ok=[];alldata.Qok=[];alldata.eok=[];alldata.pat=[];
alldata.frac=[];time2.e=zeros(0,1); time2.u = zeros(0,1);
for i = 1:3
    sitedata{i}.T2ok = []; sitedata{i}.Qok = []; sitedata{i}.eok = [];
end

for fileid = 3:length(DIR);
    load(['data_tumorMotionResults/' DIR(fileid).name])
    load([fileparts(cd) '/data_MarkerFiles/' cybdata.sessionID 'markerext.mat'])
    traini = 1:qtyTrainPts;
    ti = find(cybdata.t>markerextt(1),1):find(cybdata.t<markerextt(end));
    t = cybdata.t(ti,1,'last');
    if length(t)>length(traini)

        % collect input (intermittent X, high-frequency mvect) and output (Y) data
        Y = cybdata.internalFiducial(ti,1,'last',:);
        mvect{1} = markerext1; mvect{2} = markerext2; mvect{3} = markerext3;
        testi = (qtyTrainPts+1):size(Y,1);
        X = [cybdata.externalMarker1 cybdata.externalMarker2 cybdata.externalMarker3];

        % project marker motion onto 1D
        [R rContinuous] = func_projectData(mvect,markerextt,cybdata,traini,t);
        r=[R{1} R{2} R{3}];

        % apply PLS
        [model3D validation3D] = func_spcPLS_presetLV_v2(X(testi,:),...
            X(traini,:),Y(traini,:),qtyLV);
        [model1D validation1D] = func_spc_PLS_v2(r(testi,:),r(traini,:),Y(traini,:));
        errs = sum((Y(testi,:)-validation1D.pred{2}).^2,2).^(1/2);

        % T^2
        tsqsTrain = model3D.tsqs;
        tsqsTest = validation3D.tsqs{1,1};
        tsqcl = tsqlim(model3D,T2perc);
        outoftsqlim = find(tsqsTest>tsqcl);

        % Q(X)
        QTrain = model3D.ssqresiduals{1,1};
        QTest = validation3D.ssqresiduals{1,1};
        rescl = residuallimit(model3D,Qperc);
    end
end
```

```

outofreslim = find(QTest>rescl);

[sens,spec,T2OK,QOK,eOK]=func_pp_v1(tsqsTest,tsqcl,QTest,rescl,errs,maxe);

% collect all results
alldata.T2ok(end+1:end+length(T2OK))=T2OK;
alldata.Qok(end+1:end+length(QOK)) =QOK;
alldata.eok(end+1:end+length(eOK)) =eOK;
alldata.pat(end+1:end+length(eOK)) =ones(1,length(eOK))*cybdata.patientNum;
alldata.frac(end+1:end+length(eOK)) =ones(1,length(eOK))*cybdata.fractionNum;
end
end

[alldata.sens_t2 alldata.spec_t2] = func_calcss(alldata.T2ok,alldata.eok);
[alldata.sens_q alldata.spec_q] = func_calcss(alldata.Qok,alldata.eok);
[alldata.sens_u alldata.spec_u] = func_calcss( ~or(~alldata.T2ok,~alldata.Qok),...
alldata.eok);

```

## B.5 func\_pp\_v1

```

function [sens,spec,T2OK,QOK,eOK]=func_pp_v1(tsqsTest, tsqcl, QTest, rescl, errs, thresh)
%
% This function processes the tsqsTest, QTest, and errs results
% from the SPC study to determine the predictive power of the
% SPC monitoring technique.
%
% Kathleen Malinowski
% June 14, 2011

T2OK = (tsqsTest<=tsqcl);
QOK = (QTest<=rescl);
eOK = (errs<=thresh);
[sens.T2 spec.T2] = func_calcss( T2OK,eOK); % sensitivity and specificity T^2
[sens.Q spec.Q] = func_calcss( QOK,eOK); % sens. and spec Q(X)
[sens.UNION spec.UNION] = func_calcss( ~or(~T2OK,~QOK),eOK); % sens and spec T^2UQ(X)
end

```

## B.6 func\_calcss

```

function [sens spec] = func_calcss(varOK,eOK)
%
% calculates the sensitivity and specificity
% from "varOK" by aligning the T^2 and Q(X)
% pass/fail to the error pass/fail
%
% Kate Malinowski
% February 22, 2010

TP = length(find(and(~varOK,~eOK)));
FP = length(find(and(~varOK, eOK)));
TN = length(find(and( varOK, eOK)));
FN = length(find(and( varOK,~eOK)));
sens = TP/(TP+FN);
spec = TN/(TN+FP);
end

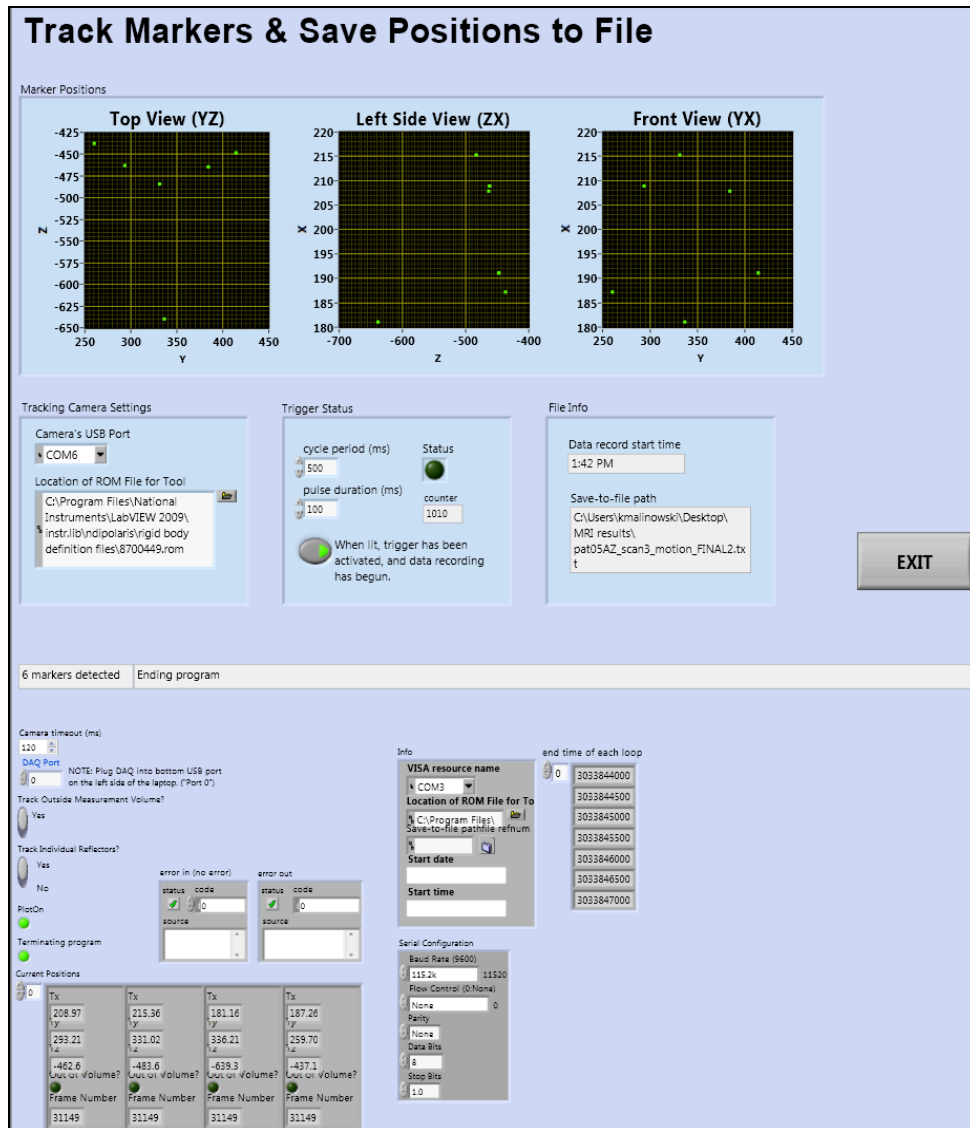
```

# APPENDIX C: Selected Labview Code

## C.1 Main Program for Spectra Tracking During MR Study

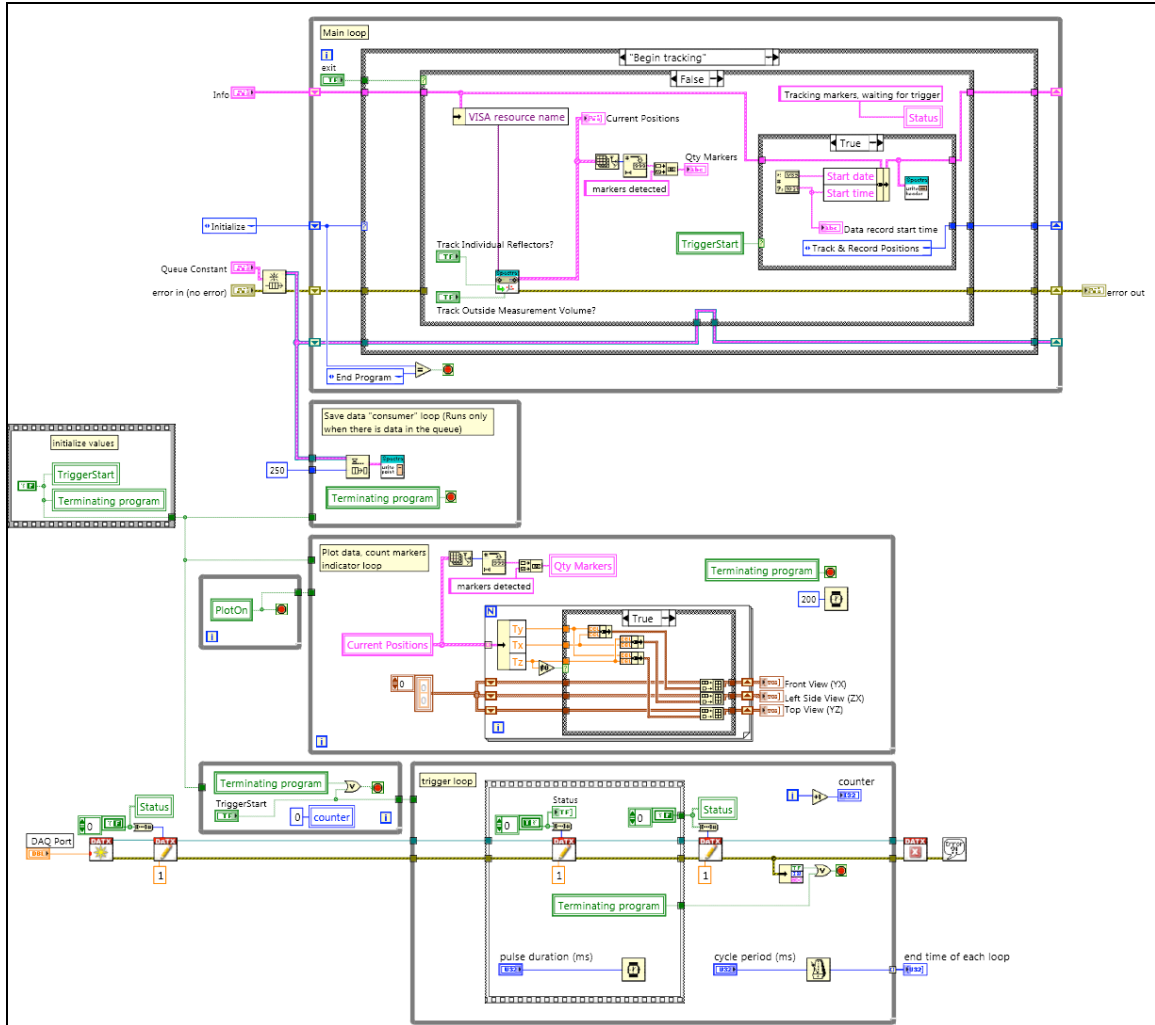
Spectra\_trackandrecord\_v7.vi  
 Based on Labview Standard State Machine

### C.1.1 Front Panel



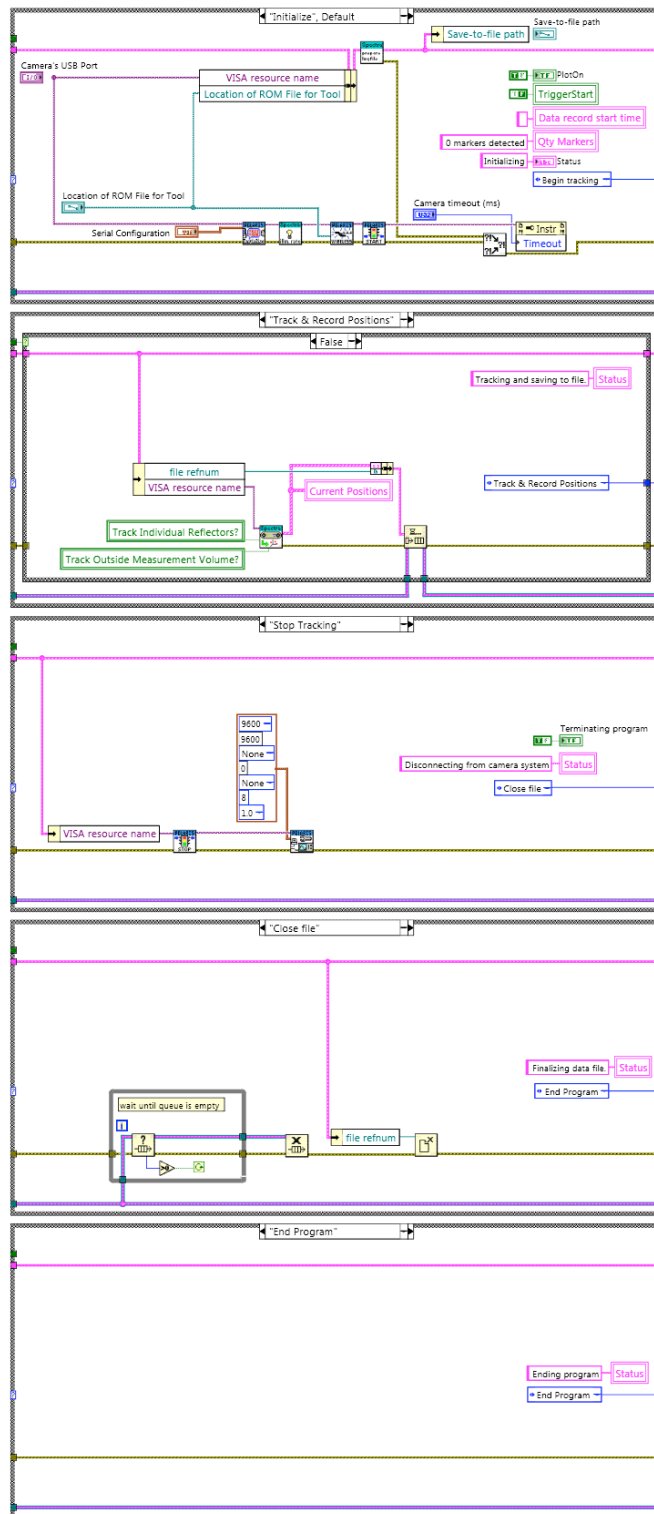
## C.1.2 Block Diagram

### C.1.2.1 Full Block Diagram





### C.1.2.3 States in Case Structure of Block Diagram Main Loop

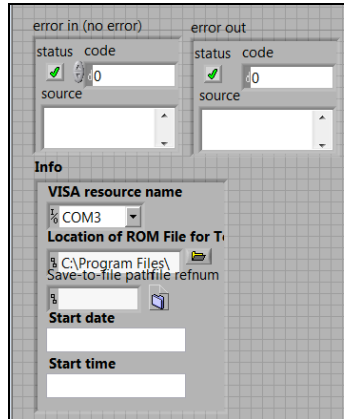


## C.2 Data Logging Code

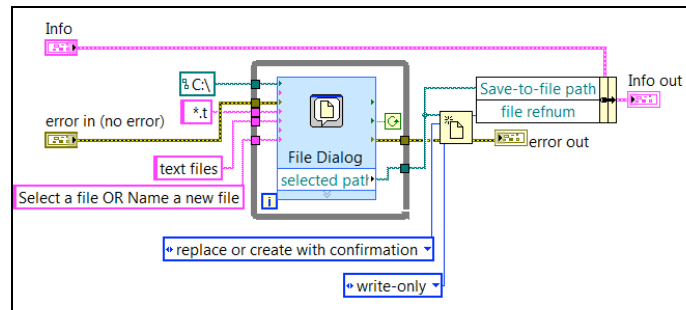
### C.2.1 Log File Creation

Spectra\_logdata\_init.vi

#### C.2.1.1 Front Panel



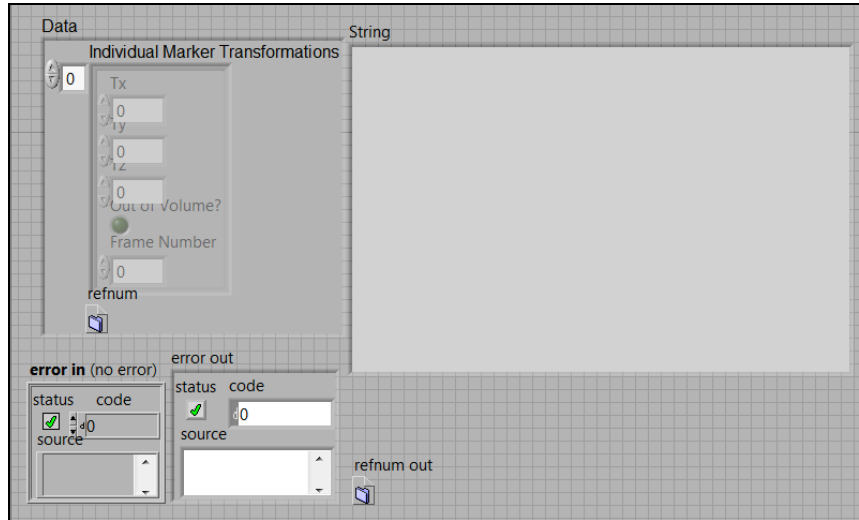
#### C.2.1.2 Block diagram



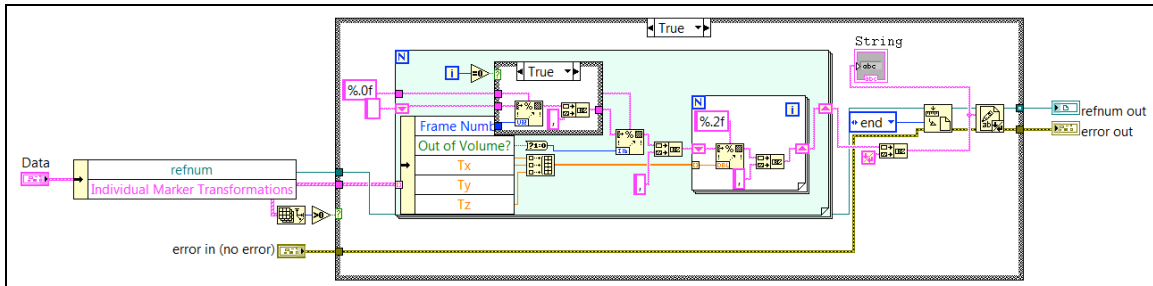
## C.2.2 Logging During Tracking

Spectra\_one\_datapoint.vi

### C.2.2.1 Front Panel



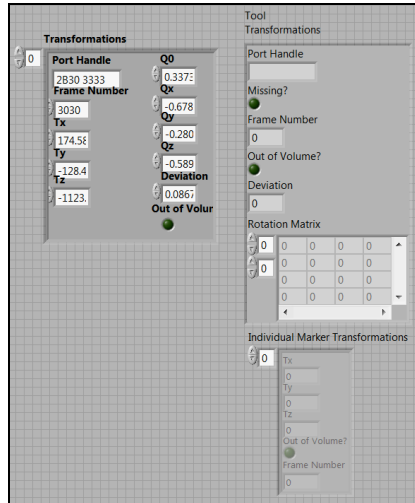
### C.2.1.2 Block Diagram



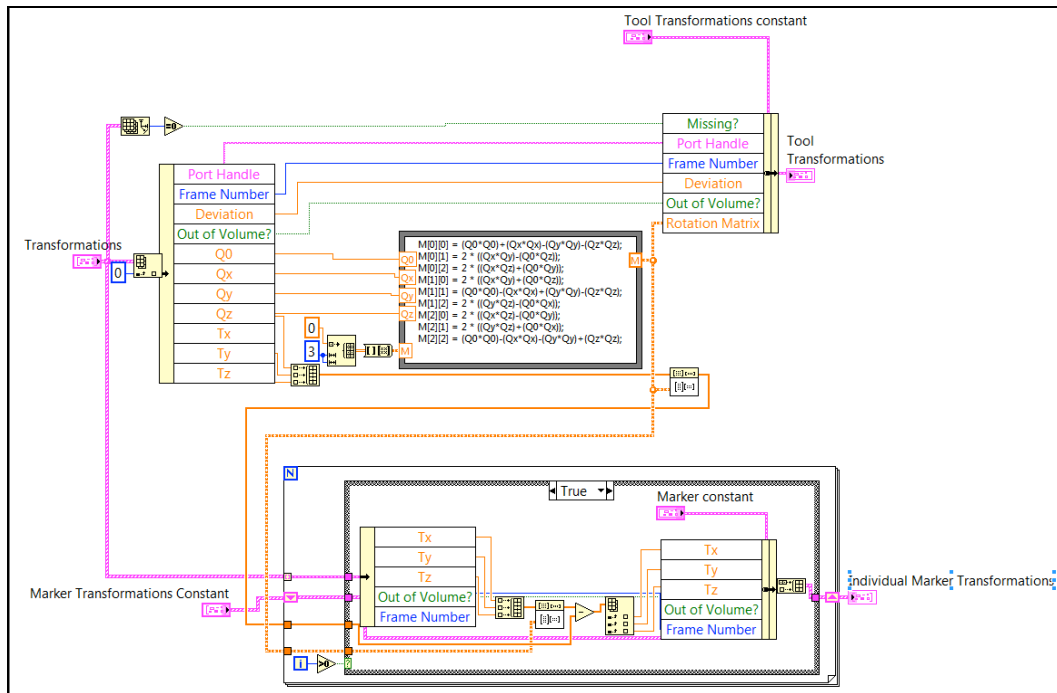
### C.3 Transformation from Quaternion to Cartesian Coordinates

Spectra\_logdata\_init.vi

#### C.2.1 Front Panel



#### C.2.2 Block Diagram



## REFERENCES

1. The American Society for Radiation Oncology. 2011. "Fast facts about radiation therapy." Retrieved March 16, 2012, from <https://www.astro.org/News-and-Media/Media-Resources/FAQs/Fast-Facts-About-Radiation-Therapy/Index.aspx>
2. Mah, D., Hanley, J., Rosenzweig, K.E., Yorke, E., Braban, L., Ling, C.C., Leibel, S.A., Mageras, G. 2000. Technical aspects of the deep inspiration breath-hold technique in the treatment of thoracic cancer. *International Journal of Radiation Oncology Biology and Physics* 48(4):1175-85.
3. Gierga, D.P., Brewer, J., Sharp, G.C., Betke, M., Willett, C.G., and Chen, G.T. 2005. The correlation between internal and external markers for abdominal tumors: implications for respiratory gating. *International Journal of Radiation Oncology Biology and Physics* 61(5):1551-1558.
4. Erridge, S.C., Seppenwoolde, Y., Muller, S.H., van Herk, M., De Jaeger, K., Belderbos, J.S., Boersma, L.J., and Lebesque, J.V. 2003. Portal imaging to assess set-up errors, tumor motion and tumor shrinkage during conformal radiotherapy of non-small cell lung cancer. *Radiotherapy and Oncology*. 66(1):75-85.
5. Keall, P.J., Mageras, G.S., Balter, J.M., Emery, R.S., Forster, K.M., Jiang, S.B., Kapatoes, J.M., Low, D.A., Murphy, M.J., Murray, B.R., Ramsey, C.R., van Herk, M.B., Vedam, S.S., Wong, J.W., and Yorke, E. 2006. The management of respiratory

- motion in radiation oncology report of AAPM Task Group 76. *Medical Physics*. 33(10):3874-3900.
6. Ozhasoglu, C., and Murphy, M. 2002 Issues in respiratory motion compensation during external-beam radiotherapy. *International Journal of Radiation Oncology Biology and Physics* 52;1389-1399.
  7. Bortfeld, T., Jiang, S.B., and Rietzel, E. 2004. Effects of motion on the total dose distribution. *Seminars in Radiation Oncology* 14:41-51.
  8. Mori, S., Chen, G.T.Y., and Endo, M. 2007. Effects of intrafractional motion on water equivalent pathlength in respiratory-gated heavy charged particle beam radiotherapy. *International Journal of Radiation Oncology Biology and Physics* 69(1):308-317.
  9. Wu, Q.J., Thongphiew, D., Wang, Z., Changkong, V., and Yin, F.F. 2008. The impact of respiratory motion and treatment technique on stereotactic body radiation therapy for liver cancer. *Medical Physics* 35(4):1440-1451.
  10. Chaudhari, S.R., Goddu, S.M., Rangaraj, D., Pechenaya, O.L., Lu, W., Kintzel, E., **Malinowski, K.**, Parikh, P.J., Bradley, J.D., and Low, D.A. 2009. Dosimetric variances anticipated from breathing- induced tumor motion during tomotherapy treatment delivery. *Physics in Medicine and Biology* 54:2541-2555.

11. Linthout N, Bral S, Van de Vondel I, Verellen D, Tournel K, Gevaert T, Duchateau M, Reynders T, Storme G. Treatment delivery time optimization of respiratory gated radiation therapy by application of audio-visual feedback. *Radiother Oncol*. 2009 Jun;91(3):330-5.
12. Cheung PC, Sixel KE, Tirona R, Ung YC. Reproducibility of lung tumor position and reduction of lung mass within the planning target volume using active breathing control (ABC). *Int J Radiat Oncol Biol Phys*. 2003 Dec 1;57(5):1437-42.
13. Eccles, C.L., Patel, R., Simeonov, A.K., Lockwood, G., Haider, M., and Dawson, L.A. 2011. Comparison of liver motion with and without abdominal compression using cine-magnetic resonance imaging. *International Journal of Radiation Oncology Biology and Physics* 79(2):602-608.
14. International Commission on Radiation Units and Measurements. 1999. ICRU Report 62: Prescribing, recording and reporting photon beam therapy (Supplement to ICRU Report 50). Bethesda, MD.
15. Chen, G.T.Y., Kung, J.H., and Beaudette, K.P. 2004. Artifacts of computed tomography scanning of moving objects. *Seminars in Radiation Oncology* 14:19-26.
16. Plathow, C., Ley, S., Fink, C., Puderbach, M., Hosch, W., Schmähl, A., Debus, J., and Kauczor, H.U. 2004. Analysis of intrathoracic tumor mobility during whole

- breathing cycle by dynamic MRI. *International Journal of Radiation Oncology Biology and Physics* 59(4):952-959.
17. American Cancer Society. 2010. "Cancer facts and figures." Retrieved September 30, 2011, from <http://www.cancer.org/acs/groups/content/@nho/documents/document/acspc-024113.pdf>
18. Seppenwoolde, Y., Berbeco, R.I., Nishioka, S., Shirato, H., and Heijmen, B. 2007. Accuracy of tumor motion compensation algorithm from a robotic respiratory tracking system: a simulation study. *Medical Physics* 34:2774-2784.
19. D'Souza, W.D., and McAvoy, T.J. 2006. An analysis of the treatment couch and control system dynamics for respiration-induced motion compensation. *Medical Physics* 33(12):4701-4709.
20. Sawant, A., Venkat, R., Srivastava, V., Carlson, D., Poyzner, S., Cattell, H., and Keall, P. 2008. Management of three-dimensional intrafraction motion through real-time DMLC tracking. *Medical Physics* 35(5):2050-61.
21. Berbeco, R.I., Nishioka, S., Shirato, H., Chen, G.T., and Jiang, S.B. 2005. Residual motion of lung tumours in gated radiotherapy with external respiratory surrogates. *Physics in Medicine and Biology* 50(16):3655-3667.



22. Smith, R.L., Lechleiter, K., **Malinowski, K.**, Shepard, D.M., Housley, D.L., Afghan, M., Newell, J., Peterson, J., Sargent, B., and Parikh, P. 2009. Evaluation of linear accelerator gating with real-time electromagnetic tracking. *International Journal of Radiation Oncology Biology and Physics* 74(3):920-927.
23. Shirato, H., Suzuki, K., Sharp, G.C., Fujita, K., Onimaru, R., Fujino, M., Kato, N., Osaka, Y., Kinoshita, R., Taguchi, H., Onodera, S., and Miyasaka, K. 2006. Speed and amplitude of lung tumor motion precisely detected in four-dimensional setup and in real-time tumor-tracking radiotherapy. *International Journal of Radiation Oncology Biology and Physics* 64(4):1229-1236.
24. Santanam L, **Malinowski K**, Hubensmidt J, Dimmer, S., Mayse, M.L., Bradley, J., Chaudhari, A., Lechleiter, K., Goddu, S.K., Esthappan, J., Mutic, S., Low, D.A., and Parikh, P. 2008. Fiducial-based translational localization accuracy of electromagnetic tracking system and on-board kilovoltage imaging system. *International Journal of Radiation Oncology Biology and Physics* 70:892-899.
25. Mayse, M.L., Parikh, P.J., Lechleiter, K.M., Dimmer, S., Park, M., Chaudhari, A., Talcott, M., Low, D.A., and Bradley, J.D. 2008. *International Journal of Radiation Oncology Biology and Physics* 72(1):93-98.
26. Shchory, T., Schifter, D., Lichtman, R., Neustadter, D., and Corn, B. 2010. Tracking accuracy of a real-time fiducial tracking system for patient positioning and

- monitoring in radiation therapy. *International Journal of Radiation Oncology Biology and Physics* 78(4):1227-1234.
27. Neustadter, D., Barnea, G., Stokar, S., and Corn, B. 2010. Analysis of dose to patient, spouse/caretaker, and staff, from an implanted trackable radioactive fiducial for use in the radiation treatment of prostate cancer. *Medical Physics* 37(3):1220-1224.
28. Tsunashima, Y., Sakae, T., Shioyama, Y., Kagei, K., Terunuma, T., Nohtomi, A., and Akine, Y. 2004. Correlation between the respiratory waveform measured using a respiratory sensor and 3D tumor motion in gated radiotherapy. *International Journal of Radiation Oncology Biology and Physics* 60(3):951-958.
29. Vedam, S.S., Kini, V.R., Keall, P.J., Ramakrishnan, V., Mostafavi, H., and Mohan, R. 2003. Quantifying the predictability of diaphragm motion during respiration with a noninvasive external marker. *Medical Physics* 30:505-513.
30. Hoisak, J.D.P., Sixel, K.E., Tirona, R., Cheung, P.C., and Pignol, J.P. 2004. Correlation of lung tumor motion with external surrogate indicators of respiration. *International Journal of Radiation Oncology Biology and Physics* 60(4):1298-1306.
31. Zhao T, Lu W, Yang D, Mutic S, Noel CE, Parikh PJ, Bradley JD, Low DA. Characterization of free breathing patterns with 5D lung motion model. *Med Phys*. 2009 Nov;36(11):5183-9.

32. Spoelstra, F.O., van Sörnsen de Koste, J.R., Vincent, A., Cuijpers, J.P., Slotman, B.J., and Senan, S. 2009. An evaluation of two internal surrogates for determining the three-dimensional position of peripheral lung tumors. *International Journal of Radiation Oncology Biology and Physics* 74(2):623-9.
33. Yan, H., Yin, F., Zhu, G., Ajlouni, M., and Kim, J.H. 2007. The correlation evaluation of a tumor tracking system using multiple external markers. *Medical Physics* 33:4073-4084.
34. Ionascu, D., Jiang, S.B., Nishioka, S., Shirato, H., and Berbeco, R.I. 2007. Internal-external correlation investigations of respiratory induced motion of lung tumors. *Medical Physics* 34(10):3893-3903.
35. Killoran JH, Allen AM, Kann BH, and Lyatskaya, Y. 2008. Interfractional variability of breathing phase definition as determined by fiducial location. *Medical Physics* 35(2):753-763.
36. Yan, H., Zhu, G., Yang, J., Lu, M., Ajlouni, M., Kim, J.H., and Yin, F.F. 2008. Investigation of the location effect of external markers in respiratory-gated radiotherapy. *Journal of Applied Clinical Medical Physics* 9(2):57-68.
37. Qiu, P., D'Souza, W.D., McAvoy, T.J., and Ray Liu, K.J. 2007. Inferential modeling and predictive feedback control in real-time motion compensation using the treatment couch during radiotherapy. *Physics in Medicine and Biology* 52(19):5831-5854.

38. Schweikard, A., Shiomi, H., and Adler, J. 2004. Respiration tracking in radiosurgery. *Medical Physics* 31(10):2738-2741.
39. Chen, Q.S., Weinhaus, M.S., Deibel, F.C., Cieszki, J.P., and Macklis, R.M. 2001. Fluoroscopic study of tumor motion due to breathing: facilitating precise radiation therapy for lung cancer patients. *Medical Physics* 28(9):1850-18536.
40. Allen, MP. 1997. *Understanding Regression Analysis*. New York: Plenum Press 3-4.
41. de Jong, S. 1993. SIMPLS: An alternative approach to partial least squares regression. *Chemometrics and Intelligent Laboratory Systems* 18(3):251-263.
42. Wu, C.F.J. 1986. Jackknife, bootstrap and other resampling methods in regression analysis. *The Annals of Statistics* 14(4):1261-1295.
43. Nehmeh SA, Erdi YE, Pan T, Yorke E, Mageras GS, Rosenzweig KE, Schoder H, Mostafavi H, Squire O, Pevsner A, Larson SM, Humm JL. 2004. Quantitation of respiratory motion during 4D-PET/CT acquisition. *Medical Physics* 31(6):1333-8.
44. Juhler-Nøttrup T, Korreman SS, Pedersen AN, Aarup LR, Nyström H, Olsen M, Specht L. 2007. Intra- and interfraction breathing variations during curative radiotherapy for lung cancer. *Radiotherapy and Oncology* 84(1):40-8.

45. Hugo, G., Vargas, C., Liang, J., Kestin, L., Wong, J.W., and Yan, D. 2006. Changes in the respiratory pattern during radiotherapy for cancer in the lung. *Radiotherapy and Oncology* 78;326-331.
46. Hugo GD, Yan D, Liang J. Population and patient-specific target margins for 4D adaptive radiotherapy to account for intra- and inter-fraction variation in lung tumour position. *Phys Med Biol.* 2007 Jan 7;52(1):257-74. Epub 2006 Dec 20.
47. Seppenwoolde, Y., Shirato, H., Kitamura, K., Shimizu, S., van Herk, M., Lebesque, J.V., and Miyasaka, K. 2002. Precise and real-time measurement of 3D tumor motion in lung due to breathing and heartbeat, measured during radiotherapy. *International Journal of Radiation Oncology Biology and Physics* 53;822-834.
48. Shewhart, W. (1980). *Economic control of quality of manufactured product*. Milwaukee, Wis: American Society for Quality Control.
49. Ergon R. 2004. Informative PLS score-loading plots for process understanding and monitoring. *Journal of Process Control.* 14:889-897.
50. MacGregor, J.F., and Kourti, T. 1995. Statistical process control of multivariate processes. *Control Engineering Practice* 3;403-414.
51. Jackson, J.E. and Mudholkar, G.S. 1979. Control procedures for residuals associated with principal components analysis. *Technometrics* 21;341-349.

52. Sayeh, S., Wang, J., Main, W.T., Kilby, W., and Maurer, C.R. Jr. 2007. Respiratory Motion Tracking for Robotic Radiosurgery. In: Urschel HC, Editor-in-Chief. Treating Tumors that Move with Respiration. New York:Springer 15-29.
53. George, R., Suh, Y., Murphy, M., Williamson, J., Weiss, E., and Keall, P. 2008. On the accuracy of a moving average algorithm for target tracking during radiation therapy treatment delivery. *Medical Physics* 35:2356-1265.
54. Yang, D., Lu, W., Low, D.A., Deasy, J.O., Hope, A.J., and El Naqua, I. 2008. 4D-CT motion estimation using deformable image registration and 5D respiratory motion modeling. *Med Phys* 35:4577-4590.
55. Wise, B.M. and Gallagher, N.B. 1996. The process chemometrics approach to process monitoring and fault detection. *Journal of Process Control* 6:329-348.
56. Beddar, A.S., Kainz, K., Briere, T.M., Tsunashima, Y., Pan, T., Prado, K., Mohan, R., Gillin, M., and Krishnan, S. 2007. Correlation between internal fiducial tumor motion and external marker motion for liver tumors imaged with 4D CT. *International Journal of Radiation Oncology Biology and Physics* 67:630-638.
57. Cerviño, L.I., Chao, A.K.Y., Sandhu, A., and Jiang, S.B. 2009. The diaphragm as an anatomic surrogate for lung tumor motion. *Physics in Medicine and Biology*. 54:3529-3541.

58. Meeks, S.L., Bova, F.J., Wagner, T.H., Buatti, J.M., Friedman, W.A., and Foote, K.D. 2000. Image localization for frameless stereotactic radiotherapy. *International Journal of Radiation Oncology Biology and Physics* 46:1291–1299.
59. Phillips, M.H., Singer, K., Miller, E., Stelzer, K. 2000. Commissioning an image-guided localization system for radiotherapy. *International Journal of Radiation Oncology Biology and Physics* 48:267–276.
60. Willoughby, T.R., Forbes, A.R., Buchholz, D., Langen, K.M., Wagner, T.H., Zeidan, O.A., Kupelian, P.A., and Meeks, S.L. 2006. Evaluation of an infrared camera and X-ray system using implanted fiducials in patients with lung tumors for gated radiation therapy. *International Journal of Radiation Oncology Biology and Physics* 66:568-575.
61. Abdi, H. 2003. Partial least squares regression (PLS-regression). In: Lewis-Beck M, Bryman A, Futing T (Eds.). *Encyclopedia for research methods for the social sciences*. Thousand Oaks, CA: Sage 792-795.
62. Werner, R., White, B., Handels, H., Lu, W., and Low, D.A. 2010. Technical note: development of a tidal volume surrogate that replaces spirometry for physiological breathing monitoring in 4D CT. *Medical Physics* 37:615-619.
63. Chalmer, B.J. 1987. Drawing inferences about group differences. In: *Understanding Statistics*. Marcel Dekker: Montpelier. pp 155-157.

64. Sonke, J., Rossi, M., Wolthaus, J., van Herk, M., Damen, E., and Belderbos, J. 2009. Frameless stereotactic body radiotherapy for lung cancer using four-dimensional CBCT guidance. *International Journal of Radiation Oncology Biology and Physics* 74(2):567-574.
65. Engelsman, M., Remeijer, P., van Herk, M., Lebesque, J.V., Mijnheer, B.J., and Damen, E.M. 2001. Field size reduction enables iso-NTCP escalation of tumor control probability for irradiation of lung tumors. *International Journal of Radiation Oncology Biology and Physics*. 51(5):1290-1298.
66. Hoogeman, M.S., Nuyttens, J.J., Levendag, P.C., and Heijmen, B.J. 2008. Time dependence of intrafraction patient motion assessed by repeat stereoscopic imaging. *International Journal of Radiation Oncology Biology and Physics* 70(2):609-618.
67. Mageras GS, Pevsner A, Yorke ED, Rosenzweig, K.E., Ford, E.C., Hertanto, A., Larson, S.M., Lovelock, D.M., Erdi, Y.E., Nehmeh, S.A., Humm, J.L., and Ling, C.C. 2004. Measurement of lung tumor motion using respiration-correlated CT. *International Journal of Radiation Oncology Biology and Physics* 60(3):933-941.
68. Ford, C., Mageras, G.S., York, E., and Ling, C.C. 2003. Respiration correlated spiral CT: A method of measuring respiratory-induced anatomic motion for radiation treatment planning. *Medical Physics* 30(1):88-97.



69. Rietzel, E., Chen, G.T., Choi, N.C., and Willett, C.G. 2005. Four-dimensional image-based treatment planning: Target volume segmentation and dose calculation in the presence of respiratory motion. *International Journal of Radiation Oncology Biology and Physics* 61(5):1535-1550.
70. Sher, D.J., Wolfgang, J.A., Niemierko, A., Choi, N.C. 2007. Quantification of mediastinal and hilar lymph node movement using four-dimensional computed tomography scan: implications for radiation treatment planning. *International Journal of Radiation Oncology Biology and Physics* 69(5):1402-1408.
71. Pantarotto, J.R., Piet, A.H., Vincent, A., van Sörnsen de Koste, J.R., and Senan, S. 2009. Motion analysis of 100 mediastinal lymph nodes: Potential pitfalls in treatment planning and adaptive strategies. *International Journal of Radiation Oncology Biology and Physics* Jul 15;74(4):1092-1099.
72. Donnelly, E.D., Parikh, P.J., Lu, W., Zhao, T., Lechleiter, K., Nystrom, M., Hubenschmidt, J.P., Low, D.A., and Bradley, J.D. 2007. Assessment of intrafraction mediastinal and hilar lymph node movement and comparison to lung tumor motion using four-dimensional CT. *International Journal of Radiation Oncology Biology and Physics* 69(2):580-588.
73. Bosmans, G., van Baardwijk, A., Dekker, A., Ollers, M., Wanders, S., Boersma, L., Lambin, P., and de Ruyscher, D. 2008. Time trends in nodal volumes and motion

- during radiotherapy for patients with Stage III non-small-cell lung cancer. *International Journal of Radiation Oncology Biology and Physics* 71(1):139-144.
74. Maxim, P.G., Loo, B.W., Jr., Shirazi, H., Thorndyke, B., Luxton, G., and Le, Q.T. 2007. Quantification of motion of different thoracic locations using four-dimensional computed tomography: implications for radiotherapy planning. *International Journal of Radiation Oncology Biology and Physics* 69(5):1395-1401.
75. Mountain CF, and Dresler CM. 1997. Regional lymph node classification for lung cancer staging. *Chest* 111:1718–1723.
76. Koch, N., Liu, H.H., Starkschall, G., Jacobson, M., Forster, K., Liao, Z., Komaki, R., and Stevens, C.W. 2004. Evaluation of internal lung motion for respiratory-gated radiotherapy using MRI: Part I-correlating internal lung motion with skin fiducial motion. *International Journal of Radiation Oncology Biology and Physics* 60(5):1459-1472.
77. Higgins, J., Bezjak, A., Franks, K., Le, L.W., Cho, B.C., Payne, D., and Bissonnette, J.P. 2009. Comparison of spine, carina, and tumor as registration landmarks for volumetric image-guided lung radiotherapy. *International Journal of Radiation Oncology Biology and Physics* 73(5):1404-1413.
78. van der Weide, L., van Sörnsen de Koste, J.R., Lagerwaard, F.J., Vincent, A., van Triest, B., Slotman, B.J., and Senan, S. 2008. Analysis of carina position as surrogate

- marker for delivering phase-gated radiotherapy. *International Journal of Radiation Oncology Biology and Physics* 71(4):1111:1117.
79. Piet, A.H.M., Lagerwaard, F.J., Kunst, P.W.A., van Sörnsen de Koste, J.R., Slotman, B.J., and Senan, S. 2007. Can mediastinal nodal mobility explain the low yield rates for transbronchial needle aspiration without real-time imaging? *Chest* 131:1783-1787.
80. Liu, H.H., Balter, P., Tutt, T., Choi, B., Zhang, J., Wang, C., Chi, M., Luo, D., Pan, T., Hunjan, S., Starkschall, G., Rosen, I., Prado, K., Liao, Z., Chang, J., Komaki, R., Cox, J.D., Mohan, R., Dong, L. 2007. Assessing respiration-induced tumor motion and internal target volume using four-dimensional computed tomography for radiotherapy of lung cancer. *International Journal of Radiation Oncology Biology and Physics* 68(2):531-540.
81. Wu, J., Lei, P., Shekhar, R., Li, H., Sunthralingam, M., and D'Souza, W.D. 2009. Do tumors in the lung deform during normal respiration? An image registration investigation. *International Journal of Radiation Oncology Biology and Physics* 75(1):268-275.
82. Lee, J., Yoo, C., In-Beum, L. 2004. Statistical monitoring of dynamic processes based on dynamic independent component analysis. 59:2995-3006.

83. Cai J, McLawhorn R, Read PW, Larnar JM, Yin FF, Benedict SH, Sheng K. Effects of breathing variation on gating window internal target volume in respiratory gated radiation therapy. *Med Phys*. 2010 Aug;37(8):3927-3934.
84. MacQueen, J. 1967. Some methods for classification and analysis of multivariate observations. In: *Proceedings of the Fifth Berkeley Symposium on Mathematical Statistics and Probability, Volume 1*. University of California Press: 1967;281-297.
85. Geraghty, P.R., Kee, S.T., McFarlane, G., Razavi, M.K., Sze, D.Y., Dake, M.D. 2003. CT-guided transthoracic needle aspiration biopsy of pulmonary nodules: needle size and pneumothorax rate. *Radiology* 229(2):475-481.
86. Tachibana, H., Kitamura, N., Ito, Y., Kawai, D., Nakajima, M., Tsuda, A., Shiizuka, H. 2011. Management of the baseline shift using a new and simple method for respiratory-gated radiation therapy: Detectability and effectiveness of a flexible monitoring system. *Medical Physics* 38(7):3971-3980.
87. Upasani, M., Chopra, S., Engineer, R., Medhi, S., Master, Z., Mahantshetty, U., Shrivastava, S.K. 2011. Inter and intraobserver variation in gross tumor delineation on megavoltage CT images in patients undergoing tomotherapy-based image-guided radiotherapy for postoperative vault recurrences. *Journal of Cancer Research and Therapeutics*. 7(3):292-297.

88. D'Souza, W.D., **Malinowski, K.T.**, Van Liew, S., D'Souza, G., Asbury, K., McAvoy, T.J., Suntharalingam, M., Regine, W.F. 2009. Investigation of motion sickness and inertial stability on a moving couch for intra-fraction motion compensation. *Acta Oncologica* 48(8):1198-1203.



# CURRICULUM VITAE

Kathleen T. Malinowski  
1303 Rogers Rd. Apt 3, Annapolis, MD 21409  
kate.malinowski@gmail.com  
503-896-6381

## CURRENT POSITIONS

Research Assistant  
Department of Bioengineering, University of Maryland, College Park, MD  
Department of Radiation Oncology, University of Maryland School of Medicine,  
Baltimore, MD

## EDUCATION

Ph.D. in Bioengineering, University of Maryland, College Park, MD  
Expected graduation date: May 2012, GPA: 4.0  
M.S. in Biomedical Engineering, Washington University in St. Louis, St. Louis, MO  
B.S. in Biomedical Engineering, Washington University in St. Louis, St. Louis, MO  
Minor in Electrical Engineering, December 2007, GPA: 3.9 (magna cum laude)

## HONORS AND AWARDS

ARCS Foundation Scholarship	2010-2012
2nd Place, Young Investigators Symposium, MAC-AAPM Annual Meeting	2010
Finalist, Fischell Fellowship Business Plan Contest	2009
Walter A. Sperry Scholarship for Engineering Education, Foundation of the Fox River Valley	2007
Gustav Kurt Mesmer Scholarship, Washington University in St. Louis	2003-2007
Dean's Scholarship, Washington University in St. Louis	2003-2007
National Merit Scholarship, AON Warranty Group	2003-2007
Indian Prairie School District Classified Association Scholarship	2007
Antoinette Frances Dames Award for Outstanding Performance in Engineering, Washington University in St. Louis	2005

## SELECTED RESEARCH AND WORK EXPERIENCE

Research Assistant, Department of Radiation Oncology  
University of Maryland

2008-present

*Developed Machine Learning techniques for rapidly and accurately localizing a tumor during radiation therapy treatments.*

- Created novel, patent-pending techniques that will be incorporated into a patient positioning device.
- Analyzed and drew conclusions from large datasets using multivariate statistics.

*Developed a prototype robotic patient positioning system on an embedded platform.*

- Designed and programmed a prototype of the user interface and underlying software for initial testing.
- Minimized latency in a serial component by bypassing unnecessary I/O layers.

*Administered imaging studies to patient-volunteers and collaborated on clinical study documentation.*

- Drafted institutional review board (IRB) protocols and consent documents for studies involving patients.

*Additional relevant projects and responsibilities:*

- Edited NIH and corporate grant applications for my advisor and other faculty.
- Guided fifteen student groups through the research proposal development process.
- Interviewed and critiqued candidates for post-doctoral assistantship positions.

Biomedical Engineer, Automation group  
Innoventor, Inc.

2007-2008

*Participated in the completion of contracted projects. Programmed software components and developed user manuals as well as system validation documentation.*

- Mastered complex aerospace industry environmental testing regulations to become the in-house expert.
- Achieved certification as an associate developer of the Labview programming language.

Research Assistant, Dept. of Radiation Oncology  
Washington University in St. Louis

2006-2007

*Redesigned, manufactured, sold, and delivered a robotic research tool for radiotherapy quality assurance.*

- Managed time and budget associated with design and production.
- Coordinated with manufacturers and machinists to have custom parts built.
- Wrote a user manual and led usability testing on the system.

*Applied for funding to support lab activities.*

- Assumed control of a successful academic/industrial partnership NIH R01 application, including setting a timeline for completion and delegating tasks to myself, another student, and my advisor.
- Mastered new topics quickly in order to write and revise grant application chapters.

Research Technician, Dept. of Anatomy & Neurobiology  
Washington University in St. Louis

2004-2005

*Trained non-human primates to perform gaze-reach tasks during single-neuron recording and assisted in surgeries for implantation of a magnetic ocular tracking system.*



## TEACHING EXPERIENCE

- Tutor, Chemistry, Algebra, and Spanish 2011
- Teaching Assistant, BIOE411 Tissue Engineering, University of Maryland 2010
- Teaching Assistant, BIOE120 Intro to Biology for Engineers, University of Maryland 2009
- Mentor, BME401 Biomedical Engineering Design I, Washington University in St. Louis 2006
- Mentor, BME402 Biomedical Engineering Design II, Washington University in St. Louis 2006
- Instructor, SAT Math, RLK Educational Services 2008

## PROFESSIONAL ACTIVITIES

Reviewer, *Medical Physics* (2011)

Reviewer, *Physics in Medicine and Biology* (2012)

## PATENTS

1. WD D'Souza, KT Malinowski, TJ McAvoy. A method for monitoring the accuracy of tissue motion prediction from surrogates. US Provisional Patent Application 61/506,667, filed July 2011. Patent Pending.
2. WD D'Souza, HH Zhang, KT Malinowski. Techniques for compensating movement of a treatment target in a patient. US Patent Application 13/172,010, filed June 2011. Publication Number US 2012-0004518. Patent Pending.

## PROCEEDINGS & SHORT PAPERS

1. H Zhang, K Malinowski, WD D'Souza. Machine Learning for Intra-Fraction Tumor Motion Modeling with Respiratory Surrogates. Proceedings of IEEE International Conference on Machine Learning and Applications (ICMLA), December 2009.
2. P Parikh, K Lechleiter, K Malinowski, et al. Tumor correlated CT: A new paradigm for motion compensated CT for image-guided therapy. Proceedings of SPIE Medical Imaging, Vol. 7261, San Diego, CA, February 2009.
3. R Smith, K Lechleiter, K Malinowski, et al. Incorporating electromagnetic tracking into respiratory correlated imaging for high precision radiation therapy. Proceedings of SPIE Medical Imaging, Vol. 6918, San Diego, CA, February 18-20, 2008.
4. K Malinowski, C Noel, W Lu, et al. Development of the 4D phantom for patient-specific, end-to-end radiation therapy QA. Proceedings of SPIE Medical Imaging, Vol. 6510, San Diego, CA, February 19-22, 2007.

## BOOK CHAPTER

1. K Malinowski, WD D'Souza. Couch-based motion adaptation. Ed: M Murphy. In: Motion Adaptation in Radiation Therapy. CRC Press: Boca Raton. 2012;39-46.

## PEER-REVIEWED PUBLICATIONS

1. KT Malinowski, TJ McAvoy, R George, S Dieterich, W D'Souza. Online monitoring and error detection of real-time tumor displacement prediction accuracy using statistical process control techniques. *Med Phys.* 2012;39(4):2042-48.
2. KT Malinowski, TJ McAvoy, R George, S Dieterich, W D'Souza. Mitigating errors in external respiratory surrogate-based models of tumor position. *Int J Radiat Oncol Biol Phys.* 2012;82(5):e709-16.
3. KT Malinowski, TJ McAvoy, R George, S Dieterich, W D'Souza. Incidence of changes in respiration-induced tumor motion and its relationship with respiratory surrogates during individual treatment fractions. *Int J Radiat Oncol Biol Phys.* 2012;82(5):1665-73.
4. KT Malinowski, J Pantarotto, S Senan, W D'Souza. Inferring Positions of Tumor and Nodes in Stage III Lung Cancer from Multiple Anatomical Surrogates Using 4D CT. *Int J Radiat Oncol Biol Phys.* 2010;77(5):1553-60.
5. WD D'Souza, KT Malinowski, S Van Liew, G D'Souza, K Asbury, TJ McAvoy, M Suntharalingam, WF Regine. Investigation of motion sickness and inertial stability on a moving couch for intra-fraction motion compensation. *Acta Oncol.* 2009;48(8):1198-203.
6. RL Smith, K Lechleiter, K Malinowski, DM Shepard, DJ Housley, M Afghan, J Newell, J Petersen, B Sargent, P Parikh. Evaluation of linac gating with real-time electromagnetic tracking. *Int J Radiat Oncol Biol Phys.* 2009;74(3):920-7.
7. SR Chaudhari, SM Goddu, D Rangaraj, OL Pechenaya, W Lu, E Kintzel, K Malinowski, et al. Dosimetric variances from breathing-induced tumor motion during tomotherapy treatment delivery. *Phys Med Biol.* 2009;54(8):2541-55.
8. KT Malinowski, C Noel, M Roy, T Willoughby, T Djemi, S Jani, T Solberg, D Liu, L Levine, PJ Parikh. Efficient use of continuous, real-time prostate localization. *Phys Med Biol.* 2008;35(10):4735-43.
9. L Santanam, K Malinowski, J Hubenschmidt, S Dimmer, M Mayse, J Bradley, A Chaudhari, K Lechleiter, SM Goddu, J Esthappan, S Mutic, DA Low, P Parikh. Fiducial-based translational localization accuracy of an electromagnetic tracking system and an on-board kilovoltage imaging localization system. *Int J Radiat Oncol Biol Phys.* 2008;70(3):892-9.
10. EL Kiehl, S Stojadinovic, KT Malinowski, et al. Feasibility of small animal cranial irradiation with the microRT system. *Med Phys.* 2008;35(10):4735-43.
11. S Stojadinovic, DA Low, AJ Hope, M Vicic, JO Deasy, J Cui, D Khullar, PJ Parikh, K Malinowski, et al. MicroRT – small animal conformal irradiator. *Med Phys.* 2007;34(12):4706-4716.

## SELECTED PODIUM PRESENTATIONS

1. KT Malinowski, R George, S Dieterich, et al. Fluoroscopic imaging for validation and correction of patient-specific radiation therapy treatment target margins for mobile tumors. BMES Annual Meeting 2011.
2. KT Malinowski, TJ McAvoy, R George, et al. Selecting training data to optimize accuracy of respiratory surrogate-based tumor displacement models. AAPM Annual Meeting 2011.
3. KT Malinowski, TJ McAvoy, R George, et al. Maintaining tumor targeting accuracy in gating and tracking systems for respiration-induced tumor motion. AAPM Annual Meeting 2011.
4. KT Malinowski, TJ McAvoy, R George, et al. Online monitoring and error detection of real-time tumor displacement prediction accuracy using statistical process control. AAPM Annual Meeting 2010.
5. KT Malinowski, MA Yousuf, WD D'Souza. Couch motion compensation. Real-Time Motion Adaptive Radiation Therapy Workshop (Luebeck, Germany) 2009.
6. KT Malinowski, TJ McAvoy, R George, et al. Does respiration-induced tumor motion and its relationship with respiratory surrogates change during a treatment fraction? ASTRO Annual Meeting 2009.
7. KT Malinowski, JR Pantarotto, S Senan, et al. Inferring Nodal Volume and Primary Tumor Positions from Multiple Anatomical Surrogates Using 4D CT in Stage III Lung Cancer. AAPM Annual Meeting 2009.
8. KT Malinowski, T McAvoy, R George, et al. Ordinary Least Squares and Partial Least Squares for Intra-Fraction Lung Tumor Motion Modeling. AAPM Annual Meeting 2009.
9. K Malinowski, K Lechleiter, J Hubenschmidt, et al. Use of the 4D Phantom to test real-time targeted radiation therapy device accuracy. AAPM Annual Meeting 2007.
10. KT Malinowski, P Parikh, L Santanam, et al. Concurrent tracking and fluoroscopic imaging of implantable wireless electromagnetic transponders. AAPM Annual Meeting 2006.

## PROFESSIONAL MEMBERSHIP

American Association of Physicists in Medicine (AAPM)

Biomedical Engineering Society (BMES)